Multiplicity-dependent Charmonia Production with ALICE and Collective Phenomena in O-O Collisions at LHC Energies

A THESIS

Submitted in partial fulfilment of the requirements

for the award of the degree

of

DOCTOR OF PHILOSOPHY

by

Debadatta Behera

DEPARTMENT OF PHYSICS

INDIAN INSTITUTE OF TECHNOLOGY INDORE

August 2025

25 August 2025

INDIAN INSTITUTE OF TECHNOLOGY INDORE

I hereby certify that the work which is being presented in the thesis entitled **"Multiplicity-dependent Charmonia Production with ALICE and Collective Phenomena in O-O Collisions at LHC Energies"** in partial fulfillment of the requirements for the award of the degree of **Doctor of Philosophy** and submitted to the **Department of Physics, Indian Institute of Technology Indore**, is an authentic record of my own work carried out during the period from August 2020 to August 2025 under the supervision of Prof. Raghunath Sahoo, Department of Physics, Indian Institute of Technology Indore.

The matter presented in this thesis has not been submitted by me for the award of any other degree of this or any other institute.

Debadatta Behera
25.11.2025

(Debadatta Behera)

Signature of the Student with Date

This is to certify that the above statement made by the candidate is correct to the best of my knowledge.

Rahoo 25-Nov-2025

(Prof. Raghunath Sahoo)

Signature of Thesis Supervisor with Date

Mr. Debadatta Behera has successfully given his Ph.D. Oral Examination held on 25 Nov. 2025

Rahoo 25-Nov-2025

(Prof. Raghunath Sahoo)

Signature of Thesis Supervisor with Date

Dedicated

to

my family, for their endless love and sacrifices,

and
my teachers, for their wisdom and encouragement.

ACKNOWLEDGEMENTS

Unless numerous well-wishers had pointed the way, my thesis would not have seen the daylight. To all of them, I am grateful. I have learned many things from my teachers, collaborators, and friends. I have acknowledged everyone who helped me throughout this journey. I sincerely apologize if I have missed someone who deserved to be on the list.

First and foremost, I thank my supervisor, Prof. Raghunath Sahoo, for his guidance, support, and encouragement on this research career. His expertise, patience, and valuable feedback shaped this thesis.

I am privileged to participate in one of the experiments, i.e., ALICE, at the LHC, the world's largest and most powerful accelerator. I thank Prof. Marco van Leeuwen (Spokesperson, ALICE), Prof. Bedangadas Mohanty (Deputy Spokesperson, ALICE), Prof. Kai Schwed (Deputy Spokesperson, ALICE), and Prof. Zubayer Ahammed (ALICE-India spokesperson) for their support in various matters despite their busy schedule. I want to extend my gratitude to the members of the Physics Working Group on Dileptons and Quarkonia (PWG-DQ) for their valuable support throughout my analysis. Specially, I am grateful to the conveners of PWG-DQ group, Dr. Luca Micheletti, Dr. Ionut Cristian Arsen, Dr. Cristiane Jahnke, Dr. Maxime Rene Josep Guilbaud, Dr. Maurice Coquet, and Dr. Batoul Diab, for their continuous guidance, constructive feedback, and invaluable contributions to the analysis presented in this thesis. I also extend my thanks to my collaborators, Alexander Marco Tiekoetter, Dr. Dukhishyam Mallick, Dr. Lorenzo Mattei, Dr. Xiaozhi Bai, and Senjie Zhu for their insightful discussions and assistance on various aspects of the analysis.

I am thankful to my PSPC committee members, Dr. Manavendra Mahato and Srivathsan Vasudevan, for their encouragement, support, and helpful suggestions

during my research. I also want to express my gratitude to the academics and staff for their assistance and cooperation. I am especially thankful to the IIT Indore Department of Physics for providing me with the infrastructure and resources I needed to conduct my research.

I want to thank my colleagues at the Experimental High Energy Physics Laboratory at IIT Indore. Over the past five years, their constant support, companionship, and scientific discussion have made it productive and enjoyable. I am privileged to work with Dr. Dhananjaya Thakur, Dr. Sushanta Tripathy, Dr. Captain R. Singh, Dr. Suman Deb, Dr. Jayanta Dey, Dr. Aditya Nath Mishra, Dr. Arvind Khuntia, Dr. Rutuparna Rath, Dr. Neelkamal Mallick, Dr. Dushmanta Sahu, Dr. Girija Shankar Pradhan, Dr. Ronald Scaria, Suraj, Kshitish, Bhagyarathi, Kamaljeet, Kangkan, Aswathy, and Purnima. I appreciate the friendship, support, and cooperation they have given me along the way. I would especially want to thank Dr. Dhananjaya Thakur for his assistance throughout the data analysis course.

I am also greatly appreciative of all my teachers from school, college, and university. Their guidance and support built the basis for my academic path and helped me to reach here. I extend my thanks to my friends from my village for their encouragement, support, and affection over the years.

Lastly, I sincerely thank my entire family for their unconditional love, sacrifices, and steadfast support. They have always motivated me and helped me move forward.

(Debadatta Behera)

ABSTRACT

The study of ultra-relativistic heavy-ion collisions has emerged as a powerful approach to explore the fundamental properties of nuclear matter under extreme conditions of temperature and energy density. One of the primary goals of such studies is to create and understand the characteristics of a deconfined state of matter known as the quark-gluon plasma (QGP), where quarks and gluons are no longer confined within hadrons. This state is believed to have existed in the early Universe, microseconds after the Big Bang. The ALICE experiment at the CERN Large Hadron Collider (LHC) provides a unique opportunity to investigate this QCD matter through collisions of protons and heavy ions at unprecedented energies.

This thesis is focused on probing the QGP through two major studies: (i) experimental analysis on a multiplicity dependent charmonia production with ALICE and (ii) a phenomenological investigation of collective dynamics in oxygen-oxygen (O–O) collisions at LHC energies using a multi-phase transport model (AMPT). The first part addresses the emergence of heavy-ion-like signatures in small collision systems, while the second part systematically characterizes light-flavor particle production, flow coefficients, and nuclear modification effects in O–O collisions.

Traditionally, pp collisions have been regarded as a reference or baseline for heavy-ion studies due to their expected lack of QGP formation. However, recent results at the LHC have challenged this view, showing that high-multiplicity pp events exhibit phenomena similar to those seen in heavy-ion collisions, such as strangeness enhancement and long-range correlations. This raises the intriguing possibility of medium effects even in small systems. Among the most sensitive probes of QGP are heavy quarkonia bound states of heavy quark-antiquark pairs, particularly charmonium states such as J/ψ and its excited state $\Psi(2S)$.

In this thesis, we investigate the multiplicity dependence study of J/ψ and

$\psi(2S)$-over-J/ψ ratio in pp collisions at $\sqrt{s} = 13.6$ TeV using the ALICE detector. The analysis involves careful event and track selection, muon identification, background suppression, and signal extraction from invariant mass distributions. Monte Carlo simulations are used to correct for detector efficiencies and acceptance effects. Multiplicity is estimated using tracks from the central barrel detectors.

To complement the experimental analysis, we conduct a detailed phenomenological study of collective behavior in O–O collisions at $\sqrt{s_{\rm NN}} = 7$ TeV, focusing on light-flavor observables. Small collision systems like O–O serve as an intermediate bridge between pp and Pb–Pb collisions and are ideal for disentangling initial-state geometry from final-state interactions. For this purpose, we employ the AMPT model, which incorporates fluctuating initial conditions, partonic scattering, hadronization via quark coalescence, and subsequent hadronic rescattering.

Three distinct nuclear density profiles are considered for the initial geometry: Woods-Saxon, harmonic oscillator, and α-clustered configurations. These profiles influence key observables such as eccentricity, triangularity, and impact parameter distributions. The analysis covers global observables like charged-particle multiplicity, transverse energy, Bjorken energy density, pseudorapidity distributions, and speed of sound. The kinetic freeze-out temperature and radial flow velocity are extracted using Boltzmann-Gibbs blast-wave fits to the p_T spectra of π, K, and p.

The anisotropic flow is investigated using the two-particle correlation method, focusing on flow harmonics v_2 (elliptic) and v_3 (triangular). The effects of initial geometry on final-state momentum anisotropies are quantified via normalized symmetric cumulants and the number-of-constituent-quark (NCQ) scaling of v_2 for identified particles. Our findings show that α-clustered geometries produce stronger elliptic flow, consistent with the idea that initial-state fluctuations significantly impact collective dynamics.

In addition, the nuclear modification factor R_{AA} is computed by comparing O–O spectra with a pp reference, adjusted for the number of binary nucleon-nucleon collisions. We find notable suppression of high-p_T hadrons in central O–O collisions, suggesting that medium-induced energy loss effects, typically associated with QGP, are present even in these lighter systems. In Run 3 of the LHC, ALICE has collected O-O collisions data. Our studies involving various density profiles of Oxygen nuclei, when confronted with the experimental data, will pave the way forward to understand the nuclear density profiles and their impact on the final state observables in TeV collisions.

PUBLICATIONS

List of publications:

Publications included in this thesis:

1. $\Psi(2S)/J/\Psi$ production ratio as a function of charged-particle multiplicity in pp collisions at $\sqrt{s} = 13.6$ TeV with ALICE, Debadatta Behera, Dhananjaya Thakur, and Raghunath Sahoo. https://alice-notes.web.cern.ch/node/1662 [ALICE Collaboration Internal Link], ID number: ANA-1662.

2. Predictions on global properties in O+O collisions at the Large Hadron Collider using a multi-phase transport model, **D Behera**, N. Mallick, S. Tripathy, S.Prasad, A. N. Mishra, and R. Sahoo, Eur. Phys. J. A 58, 175 (2022).

3. Effects of clustered nuclear geometry on the anisotropic flow in O–O collisions at the LHC within a multiphase transport model framework, **D. Behera**, S. Prasad, N. Mallick, and R. Sahoo, Phys. Rev. D 108, 054022 (2023).

4. Characterizing nuclear modification effects in high-energy O-O collisions at energies available at the CERN Large Hadron Collider: A transport model perspective, **D. Behera**, S. Deb, C. R. Singh and R. Sahoo, Phys. Rev. C 109, 014902 (2024).

Other Publication:

1. Event topology and global observables in heavy-ion collisions at the Large Hadron Collider, S. Prasad, N. Mallick, **D. Behera**, R. Sahoo, and S. Tripathy, Sci.Rep. 12, 3917 (2022).

Conference Proceedings:

1. Global properties in O+O collisions at $s_{NN} = 7$ TeV using a multi-phase transport model, D. Behera, N. Mallick, S. Tripathy, S. Prasad, A. N. Mishra, and R. Sahoo, 65th DAE BRNS Symposium on nuclear physics, 718-719 (2022).

2. Transverse spherocity dependence of the global observables in heavy-ion collisions at the LHC, S. Prasad, N. Mallick, D. Behera, R. Sahoo, and S. Tripathy, DAE Symp.Nucl.Phys. 66, 1016-1017(2023).

3. Global properties in O+O collisions at $s_{NN} = 7$ TeV using AMPT model, D. Behera, N. Mallick, S. Tripathy, S.Prasad, A. N. Mishra, and R. Sahoo, PoS LHCP2022, 305 (2023).

4. Transverse spherocity dependence of global observables in heavy-ion collisions at the LHC using AMPT model," S. Prasad, N. Mallick, D. Behera, R. Sahoo, and S. Tripathy, LHCP2022, 331 (2023).

5. Effects of α-cluster geometry on the azimuthal anisotropy in O-O collisions at the LHC, D. Behera, S. Prasad, N. Mallick, and R. Sahoo, DAE Symp. Nucl. Phys. 67, 1043-1044 (2024).

6. Sensitivity of Nuclear Density Profiles on Global Observables in O–O Collisions at the Large Hadron Collider Using AMPT Model, D. Behera, N. Mallick, S. Tripathy, S. Prasad, A. N. Mishra, and R. Sahoo, Springer Proc.Phys. 304, 925-927, (2024).

7. Nuclear modification factor in O–O collisions at LHC: A transport model study, D. Behera, S. Deb, Captain R. Singh, and R. Sahoo, DAE Symp. Nucl. Phys. 68, 1011 (2025).

8. Event Topology in Heavy-Ion Collisions: The Initial Spatial Anisotropy and Final Azimuthal Anisotropy, S. Prasad, N. Mallick, S. Tripathy, D. Behera, and R. Sahoo, J.Subatomic Part.Cosmol. 4, 100110, (2025).

9. Study of global observables in O-O collisions at $\sqrt{s_{NN}} = 7$ TeV using a transport model, D. Behera, N. Mallick, S. Tripathy, S. Prasad, A. N. Mishra, and R. Sahoo, J.Subatomic Part.Cosmol. 4, 100260, (2025).

Contents

List of Figures

List of Tables

Chapter 1

Introduction

The aim of high-energy nuclear physics is to create and study the primordial matter composed of quarks and gluons in the laboratory. This is achieved through ultra-relativistic collisions of heavy ions using facilities like the Large Hadron Collider (LHC) at CERN and the Relativistic Heavy Ion Collider (RHIC) at Brookhaven National Laboratory. A plasma of quarks and gluons called QGP is believed to be formed in the collisions where a condition of very high temperature and energy density is achieved. In this Chapter, we briefly introduce the Standard Model of particle physics, where we explain the classification of elementary particles; after that, there are brief discussions on quantum chromodynamics (QCD). Quark Gluon Plasma (QGP) and ultra-relativistic heavy-ion collisions, along with their thermodynamics and QCD phase transition, will be discussed in the third section. Another section explores the "Little Bang" phenomenon at the LHC, while a separate section focuses on the experimental signatures of the quark-gluon plasma (QGP).

1.1 The Standard Model

The Standard Model (SM) of particle physics is one of the crowning achievements in modern physics. It was developed mainly by Glashow, Salam, and Weinberg in

the 1970s [1–3]. It provides a theoretical framework for describing fundamental particles and their interactions, excluding gravity. It includes three fundamental interactions, i.e., strong, weak, and electromagnetic. The Standard Model relies on quantum field theory and gauge symmetry $SU(3)_C \times SU(2)_L \times U(1)_Y$. The unified weak and electromagnetic force is governed by Electroweak (EW) theory, while the electromagnetic interaction is governed by quantum field theory (QFT), also referred to as quantum electrodynamics (QED). The SM model categorizes elementary particles into two groups based on their spin. Fermions are half-integer spin particles, whereas bosons are integer spin particles. Figure 1.1 depicts the twelve fundamental fermions, which are composed of three generations of six leptons and six quarks. Leptons interact via electromagnetic and weak interactions and carry negative integer electric charges. The negative charged leptons are electron (e^-), muon (μ^-) and tauon (τ^-) and their antiparticles are positively charged leptons e^+, μ^+, τ^+. The charge neutral leptons are neutrinos. These neutrinos are left-handed ($(\nu_e^L, \nu_\mu^L, \nu_\tau^L)$) and their anti-particle ($(\bar{\nu}_e^R, \bar{\nu}_\mu^R, \bar{\nu}_\tau^R)$) are right-handed.

Quarks are classified into six flavors: up (u), down (d), charm (c), strange (s), top (t), and bottom (b), each with its own anti-quark ($\bar{q}$). These have fractional electrical charges. The u, c, and t quarks have $+2e/3$ electrical charge, while the d, s, and b quarks have $-1e/3$ charge. Since quarks are fermions, they follow Pauli's exclusion principle. In the case of a baryon, all three quarks can not be placed in a single state, so they have an additional quantum number known as the color charge. They contain three types of color charge, i.e., red (r = +1), blue (b = +1), and green (g = +1), and an anti-quark carries a negative color charge (r = -1, g = -1, or b = -1). In nature, hadrons are all color-neutral. Since quarks carry both a color charge and an electrical charge, they interact through all three interactions: strong, electromagnetic, and weak.

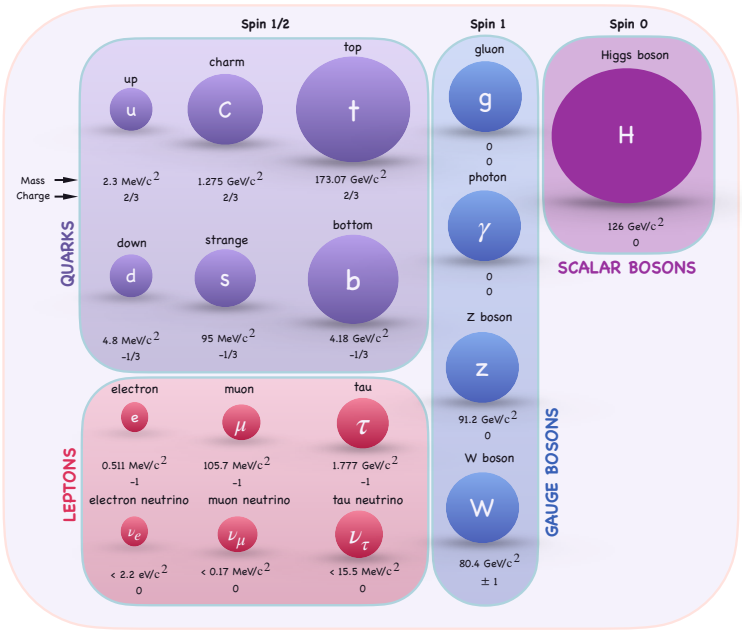

Figure 1.1: Schematic representation of the elementary particles in the Standard Model.

There are four fundamental forces present in nature: strong, weak, electromagnetic, and gravitational. There is a force carrier for each fundamental force: the gluons (g) carry the strong force, the $W^{\pm}$ and Z^0 bosons carry the weak force, and the photons (γ) carry the electromagnetic force. Photons are chargeless particles with no mass and do not interact with each other. Weak interactions are responsible for the β decays involving neutrinos and also flavour-changing decays of quarks. Quantum Electrodynamics (QED) is the theory of electromagnetic interactions, which is described using Abelian gauge theory with the symmetry group U(1). In the 1960s, Sheldon Glashow, Abdus Salam, and Steven Weinberg unified the electromagnetic and weak interactions with the symmetry group $SU(2) \times U(1)$, known as the electroweak unification. The strong interaction is the most fundamental interaction, and particles with color charges can only interact through strong interactions. Gluons, which are massless and electrically

chargeless particles but carry net color charges, mediate this. So, gluons are self-interacting, and the theory of strong interaction, known as Quantum Chromodynamics, is described by a non-Abelian SU(3) symmetry group, which will be briefly discussed in the next section.

1.2 Quantum Chromodynamics (QCD): the theory of strong interaction

The theory of strong interaction is known as Quantum Chromodynamics (QCD). It is responsible for the confinement of quarks inside hadrons inside nuclei. QCD belongs to a special class of field theories called gauge field theories, where the Lagrangian is invariant under local gauge transformations. This is known as gauge invariance [4]. Gluons carry both color and anti-color charge, so there should be $3^2 = 9$ gluons. However, one of these states corresponds to a color-neutral singlet, given by $r\bar{r} + g\bar{g} + b\bar{b}$. As a result, only eight gluons exist. The gluon-quark interaction in QCD is similar to the QED coupling of fermions and photons. Unlike photons, gluons can interact with one another, enabling more complex QCD processes. The two defining characteristics of QCD, i.e, confinement and asymptotic freedom, are covered in the following section.

1.2.1 Confinement

The QCD potential reveals that quarks experience color confinement, meaning they can not exist independently. This occurs due to the strong force, which is mediated by gluons. The following represents the QCD effective potential (V(r)) between partons: [5]

$$V(r) = -\frac{4}{3}\frac{\alpha_s}{r} + kr \tag{1.1}$$

Where α_s is the strong coupling constant, also known as running coupling constant as it depends on the scale of momentum transfer, r is the distance between the interacting partons, and k is the color string tension constant ($k \simeq 0.85$ GeV fm^{-1}) [5]. The first term arises due to single-gluon exchange at smaller r, similar to the Coulomb potential. The second term, which increases with distance r, is responsible for quark confinement. At large distances, this term becomes dominant, causing the QCD potential to increase, which strengthens the attractive force between quarks. Due to gluon self-interaction, the color field lines between two interacting partons become compressed, forming narrow color flux tubes. In other words, the effective color field intensifies as the separation distance (r) increases. Instead of allowing two free partons to emerge, the energy used in their separation is converted into the creation of a new quark-antiquark pair.

Now, in order to explain how the color field strength is developed at a large distance by gluon self-interaction, one must comprehend the phenomenon of "vacuum polarization." In QED, vacuum polarization describes the process where the background electromagnetic field generates virtual electron-positron (e^+e^-) pairs. These virtual particles create a screening effect, weakening interactions between other particles and modifying the effective charge distribution. This phenomenon is also referred to as the self-energy of gauge bosons (photons). Similarly, the QCD vacuum can generate virtual quark-antiquark and gluon pairs. The virtual $q\bar{q}$ pairs act to screen the color field over large distances, much like virtual e^+e^- pairs do in QED. However, due to gluon self-interaction, an anti-screening effect occurs, which overpowers the screening from virtual $q\bar{q}$ pairs at large distances [4, 5]. This explains why the interaction strength increases at greater separations, leading to quark confinement.

1.2.2 Asymptotic Freedom

Quark confinement indicates that the strong coupling parameter, α_s, is not a fixed constant. It means the effective strength between quarks depends upon the distance and momentum transfer. Deep inelastic scattering experiments showed that quarks inside hadrons behave almost like free particles when high-momentum electrons interact with quarks inside hadrons. Since high momentum transfer corresponds to short distances, this revealed that the strong interaction weakens at short distances but becomes extremely strong at larger distances. This property, known as asymptotic freedom, is a key feature of non-Abelian gauge theories like QCD [4]. The running coupling constant as a function of momentum transfer (Q^2) is given as:

$$\alpha_s(Q^2) = \frac{12\pi}{(11n_c - 2n_f)\ln\left(\frac{Q^2}{\Lambda^2}\right)} \tag{1.2}$$

where $n_c = 3$ colors, n_f is the number of quark flavors and the dimensional parameter λ_{QCD} is technically identical to the energy scale Q, where $\alpha_s(Q^2)$ diverges to infinity i.e. $\alpha_s(Q^2) \to \infty$ for $Q^2 \to \lambda^2_{QCD}$. In other words, λ_{QCD} (≈ 200 MeV) is the non-perturbative QCD scale parameter. For $\lambda_{QCD} < 200$ MeV, the non-perturbative QCD is in action, while above it, pQCD is applicable.

Figure 1.2 shows the coupling constant α_s decreases at short distances (high energy), allowing quarks to behave as quasi-free particles, and perturbative QCD is used to study strong interactions. This phenomenon is called asymptotic freedom. On the other hand, at long distances (low energy), the strength of the coupling increases, which leads quarks to be confined in color-neutral states. This property is called confinement. Fig. 1.2 illustrates the QCD running coupling constant variation with momentum transfer (Q) as observed in different experiments.

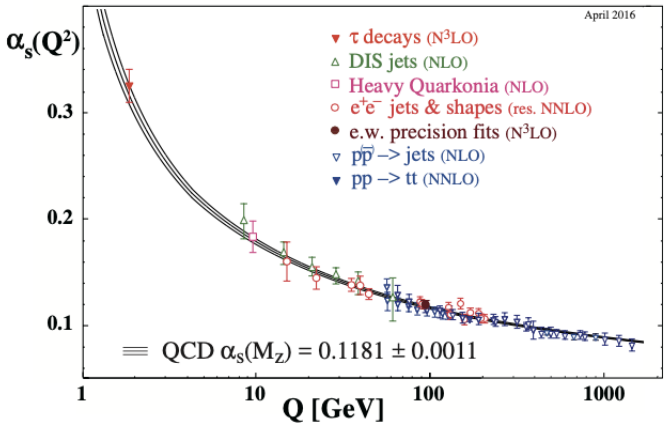

Figure 1.2: QCD coupling constant as a function of momentum transfer. The markers represent measurements based on perturbative calculations, and the solid line corresponds to an analytical prediction [6].

1.3 Quark-gluon Plasma (QGP)

QCD calculations and thermodynamic considerations indicate that strongly interacting matter can exist in various phases depending on the temperature and density of the system. QCD predicts that under extreme conditions of high temperature (T) and baryon chemical potential (μ_B), quarks and gluons transition into a deconfined state. This phase of QCD matter is thought to have existed in the early Universe, around 10^{-6} seconds after the Big Bang, when the temperature reached approximately 10^{12} K. The manifestation of their color degrees of freedom beyond hadronic dimensions occurs in this phase as hadrons melt down to create a hot and dense soup of quarks and gluons. The quark-gluon plasma (QGP) is this phase of locally thermalized and deconfined quark matter.

1.3.1 Thermodynamics of QCD

Lattice QCD calculations reveal how the energy density (ϵ) and pressure (P) of the QCD medium vary with temperature. Fig. 1.3 shows the Lattice QCD predictions of pressure (curves) and energy density (points) of the QCD medium as a function of temperature and normalized by the critical temperature (T_C). A rapid rise in ϵ/T^4 is observed in the temperature range of 150 to 200 MeV [7], followed by a gradual saturation at higher temperatures, approaching but remaining below the Stefan–Boltzmann limit. This temperature range suggests an abrupt change in thermodynamic characteristics. This can be explained by relating to a phase transition that occurs when the partonic number of degrees of freedom increases from hadronic. This change in the number of degrees of freedom implies that the QCD medium saw a phase transition from hadronic to partonic, resulting in a modification of all of its thermodynamic properties.

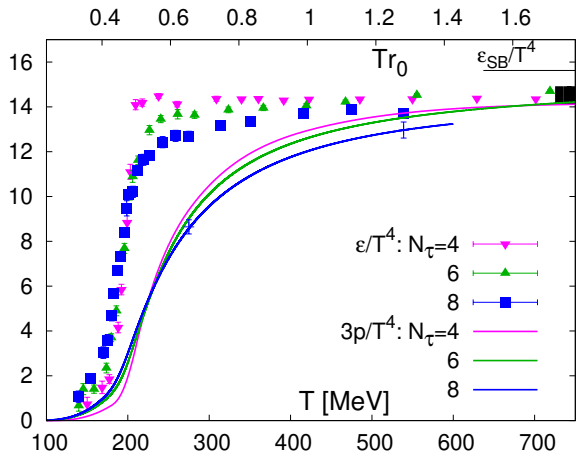

Figure 1.3: Lattice QCD predictions for the energy density (shown as points) and pressure (shown as curves) of the QCD medium as functions of temperature, normalized by the critical temperature (T_C). The ratio ϵ/T^4 represents the approach toward the Stefan–Boltzmann limit [7].

1.3.2 The QCD phase diagram

The QCD phase diagram illustrates the different states of QCD matter as a function of temperature (T) and net baryon chemical potential (μ_B). In general, temperature is associated with the energy density of the system, and the baryon chemical potential determines how much energy is required to add or remove a baryon at a given pressure and temperature. In a high-energy, relativistic system, mesons are continuously created and annihilated due to interactions, meaning their number is not a conserved quantity. Because of this, a well-defined meson chemical potential is generally not introduced in the QCD phase diagram. Hence μ_B was introduced. Fig. 1.4 shows this hypothetical QCD phase diagram. At low values of baryonic chemical potential (μ_B) and temperature (T), QCD matter primarily consists of confined hadrons. As μ_B increases while the temperature remains low, the wave functions of hadrons begin to overlap. At a certain combination of T and μ_B, this overlap becomes significant enough that quarks are no longer confined within individual nucleons but can interact freely with quarks from other nucleons in the system. This transformation leads to drastic changes in the system's thermodynamic properties, giving rise to a new state of matter known as the quark-gluon plasma (QGP). The transition from a hadronic phase to QGP at low temperatures and high μ_B is classified as a first-order phase transition. However, in the regime of low μ_B, this transition can be driven by increasing the temperature of the hadronic system. In this case, instead of a sudden shift, the thermodynamic variables evolve smoothly, resulting in a crossover transition rather than a first-order transition. This scenario is believed to have taken place in the early Universe. Due to the coexistence of these two types of phase transitions, the QCD phase diagram is expected to feature a critical point, marking the boundary between the first-order and crossover regions. This critical point corresponds to a second-order phase transition. As illustrated in Fig. 1.4, moving from high to low μ_B, the transition between hadronic matter and QGP

remains first-order until the system reaches this critical point. Beyond this, the transition becomes a smooth thermal crossover instead of a discontinuous phase change.

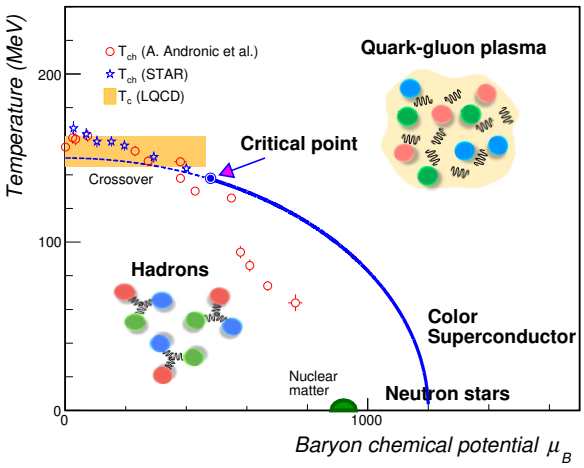

Figure 1.4: Sketch of QCD phase diagram [8].

1.4 The "Little Bang" at the LHC

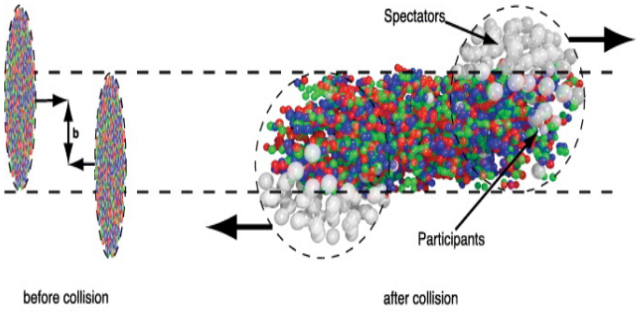

Figure 1.5: Depiction of heavy-ion collisions of two Lorentz contracted nuclei [9].

At the LHC, heavy nuclei are accelerated to extremely high energies, causing them to undergo Lorentz contraction along the beam direction. This makes them appear as flattened pancake-like shapes while moving along the beam axis

(Fig. 1.5). Their width in the transverse direction becomes much larger than their length along the beam. During a collision, the interaction can be understood as a collection of individual nucleon-nucleon collisions. The nucleons that take part in the interaction are called "participants" (N_{part}), while those that do not engage in the collision are referred to as "spectators." The number of spectators is given by $N_{\text{spect}} = 2A - N_{\text{part}}$, where A represents the mass number of the nucleus. A more detailed discussion of the collision geometry is provided in the next subsection.

1.4.1 Collision Geometry in Heavy-Ion Interactions at the LHC

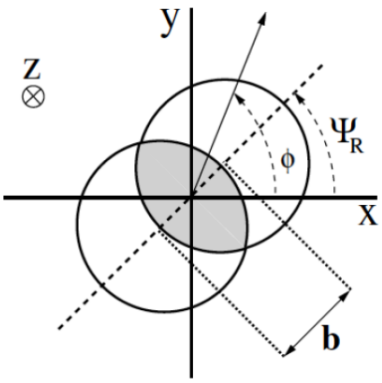

Figure 1.6: The transverse plane of collisions between heavy ions in ultra-relativistic collisions [9].

A schematic image of a transverse plane colliding with two symmetric heavy ions is displayed in Fig. 1.6. The beam axis is typically thought of as the z-axis. The overlap region of the colliding nuclei is quantified by the impact parameter (b), which is the distance measured perpendicularly between the centers of the two nuclei in the transverse plane. A small impact parameter, which indicates that the collision is nearly head-on and that the majority of the nucleons interact with one another, is a characteristic of central collisions. As a result, the final

state multiplicity of the central collisions would be maximum. Conversely, a few nucleons participate in a peripheral collision, which has a large impact parameter. The final state-charged particle multiplicity is correlated with the impact parameter and the number of participants, as shown in Fig. 1.7. The following methods can be used to select centrality: 1. from the relationship between centrality and the quantity of charged particles in the collision's final state, and 2. from the count of collision spectators. While the latter makes use of the measurement of the energy of the spectator nucleons in the forward calorimeters/detectors, the former depends on the selection of a geometrical model for the hadronic processes. The events in small collision systems, such as pp and p-Pb collisions, are divided using a similar technique based on final state multiplicity. The following chapters cover the specific techniques. As shown in Fig. 1.6, the event plane angle (ψ_R) and the impact parameter (b) vector define the event plane in heavy-ion collisions. Therefore, the impact parameter vector is needed to identify the collision's event plane.

1.4.2 Space-time evolution

The space-time evolution of relativistic nucleus-nucleus collisions with and without a deconfined state is schematically depicted in Fig. 1.8. There is a collision between two heavy ions when z = 0 and t = 0. In the central heavy-ion collision, an extremely hot and dense matter is expected to be produced.

Pre-equlibrium stage: Partons interact inelastically during this period to generate a large number of deconfined quarks and gluons. The majority of the particles created in this stage are produced by hard QCD processes and have high transverse momentum because it is the first stage of the evolution of collisions. The matter is currently in a state of non-equilibrium partons. The typical time scale of this phase is about $\tau \leq 1$ GeV$/fm^3$.

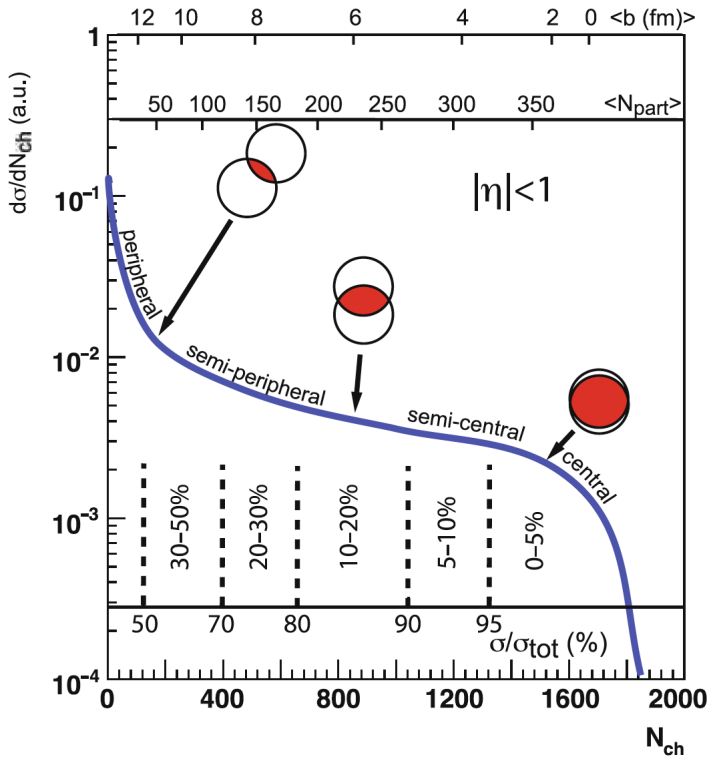

Figure 1.7: A cartoon illustrating how the impact parameter, number of participants, and the final state charged particle multiplicity are correlated [10].

QGP evolution: The produced partons from the initial interactions undergo further scattering, resulting in the local thermalization of the fireball. At this stage, it is believed that the Quark-Gluon Plasma (QGP) has been formed. Consequently, its evolution can be characterized by relativistic viscous hydrodynamics incorporating dissipative effects. During this phase, partons experience both inelastic and elastic collisions. Due to the inelastic interactions, the flavor composition of the partons of the system changes. The system starts to expand quickly due to the high internal temperature and pressure. As the system cools, quark-gluon plasma transitions into a hadron gas. This is known as the mixed phase. The QGP phase remains in existence until a few fm/c, beyond which the hydrodynamic evolution of the fireball is subjected to higher scrutiny.

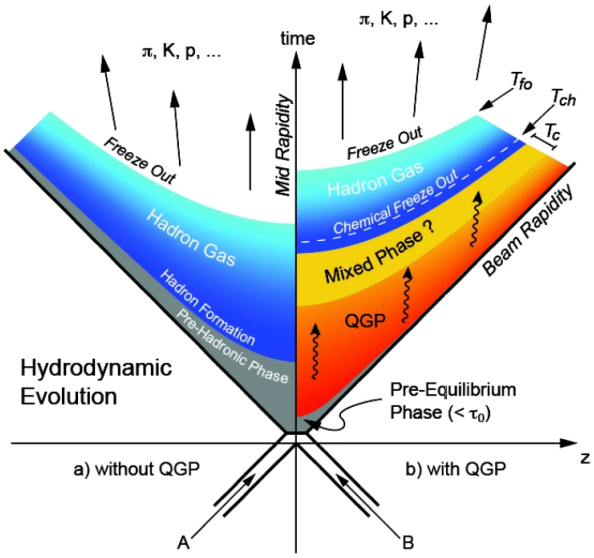

Figure 1.8: A schematic diagram of the space-time evolution of relativistic nucleus-nucleus collision [11].

Hadron gas phase and Freeze-out: There are two possible types of mechanisms for hadronization from the quark-gluon plasma (QGP), namely fragmentation and coalescence. At high energy levels, hadronization is primarily governed by fragmentation, which occurs when a high-transverse momentum (high-p_T) parton breaks into lower-transverse momentum (lower-p_T) hadrons. Coalescence, on the other hand, involves the combining of lower-momentum partons to create higher-p_T hadrons. Following hadronization, hadrons continue to interact through both elastic and inelastic processes until they achieve freeze-out. When inelastic collisions end, the system experiences chemical freeze-out, which is referred to as the chemical freeze-out temperature (T_{ch}). This phase signifies that the ratios of stable particles become fixed. However, elastic collisions still occur during this period. When the mean free path increases sufficiently, elastic collisions among hadrons will stop, marking the transition to kinetic or thermal freeze-out, with the corresponding temperature termed the kinetic freeze-out temperature (T_{fo}).

In this stage, the transverse momentum distribution of a particle becomes frozen. Once freeze-out occurs, all particles move towards the detector. Only a few stable hadron species are detected and measured in the detector. The invariant mass reconstruction technique can be used to reconstruct all other particles from their decay daughters. Relativistic transport model descriptions based on the Boltzmann equation are typically used to model the evolution of particles in the hadron gas phase.

The spacetime evolution of a system without QGP is depicted on the left side of Fig. 1.8. This scenario is appropriate for hadronic or low-energy heavy-ion collisions in which the energy density requirements for the deconfinement phase transition from the hadronic to the partonic phase are not satisfied. The partons may be deconfined in such collisions, but the small system size prevents the medium from being thermalized. Hydrodynamic descriptions, therefore, don't apply. A pre-hadronic phase with dominant hadronic productions precedes a hadron gas phase with hadron-hadron interactions, and, in the end, a freeze-out state is reached.

1.4.3 Kinematic variables in heavy-ion collisions

Kinematic variables are useful and invariant under the Lorentz transformation from one frame to another point of reference. The following list of kinematic variables, which are commonly employed in heavy-ion collisions, is briefly discussed.

Natural units: All physical quantities in high-energy physics are typically expressed in natural units, such as $\hbar = c = k_B = 1$. $\hbar c = 197.5$ MeV fm is the conversion used to convert all SI units into natural units. Thus, GeV^{-1} expresses the length and time. The primary idea of using natural units in this length scale

is supported by the proton mass being of order 1 GeV and the strong interaction lifetime of 10^{-23} sec, which is of the order of 1 fermi.

Center-of-mass energy: In a two-body collision, the center-of-mass energy is equal to the square of the sum of the four-momentum of the two incoming particles. It is a Lorentz invariant quantity and is expressed as follows:

$$s = (p_1 + p_2)^2 = (E_1 + E_2)^2 - (\overrightarrow{p}_1 + \overrightarrow{p}_2)^2 = (E_1 + E_2)^2, \tag{1.3}$$

The Mandelstam variable is denoted by s. In this case, p_1 and p_2 represent the colliding particles' four-momenta, and E_1, E_2, $\overrightarrow{p}_1$, and $\overrightarrow{p}_2$ represent the particles' energy and momentum. In the center of the mass frame, if the masses of the two colliding particles are equal, $E_1 = E_2$ and $\overrightarrow{p}_1 = -\overrightarrow{p}_2$. Consequently, the center-of-mass energy is $\sqrt{s} = E_1 + E_2 = 2E$.

Rapidity: Rapidity is a kinematic variable with an advantage over velocity due to its additive property under a Lorentz boost. The definition is as follows:

$$y = \frac{1}{2} \ln \left(\frac{E + p_z}{E - p_z} \right) = \frac{1}{2} \ln \left(\frac{1 + \beta}{1 - \beta} \right). \tag{1.4}$$

Here p_z is the longitudinal momentum, and β is the longitudinal velocity along the z-axis. Rapidity is the same as velocity in the non-relativistic limit.

Pseudo-rapidity: Energy (E) and momentum (p) can not be measured simultaneously at experiments such as RHIC and LHC because the mass of the particles can not be directly measured. Therefore, pseudo-rapidity is preferred over rapidity, which is determined by the following:

$$\eta = \frac{1}{2} \ln \left(\frac{p + p_z}{p - p_z} \right) = -ln(tan(\theta/2)) \tag{1.5}$$

Where, $\theta = \tan^{-1}(p/p_z)$ is the angle between emitted particle and beam axis. The pseudo-rapidity distribution has a shape invariance under the Lorentz transformation. Rapidity and pseudo-rapidity are equivalent under relativistic limits.

Azimuthal angle: The coordinate system in relativistic heavy-ion collisions is represented by (p_T, η, ϕ). The azimuthal angle (ϕ) is given as:

$$\phi = \tan^{-1}\left(\frac{p_y}{p_x}\right) \tag{1.6}$$

This is the angle between the total momentum vector and one of the axes (x-axis) in the transverse plane (x-y plane).

Invariant yield: The invariant yield is a Lorentz invariant quantity. This could be stated as follows in terms of experimentally measurable quantities:

$$\frac{Ed^3\sigma}{dp^3} = \frac{1}{m_T}\frac{d^3N}{dm_T d\phi dy} = \frac{1}{2\pi\, m_T}\frac{d^2N}{dm_T dy} = \frac{1}{2\pi\, p_T}\frac{d^2N}{dp_T dy}. \tag{1.7}$$

Where E and p are the energy and momentum of the particle, respectively.

1.5 Signatures of QGP and experimental probes

1.5.1 Strangeness Enhancement

One of the most remarkable indicators of QGP formation is the enhanced production of strange particles. Typically, this is investigated using the yield ratio of strange and multi-strange hadrons (e.g. $K^{\pm}, K^0_S, \Lambda + \bar{\Lambda}, \Xi^- + \bar{\Xi}^+, \Omega^- + \bar{\Omega}^+$) to non-strange hadrons ($\pi^+ + \pi^-$). The mechanism and rate of production of strange particles in the QGP medium are different from those in a hadron gas. Strange quarks are created in the QGP medium by processes such as flavor creation ($gg \to s\bar{s},\ q\bar{q} \to s\bar{s}$), flavor excitation ($gs \to gs, qs \to qs$) a gluon splitting ($g \to s\bar{s}$). In the QGP, the high gluon density leads to the dominance of $s\bar{s}$ pair

production through the $gg \rightarrow s\bar{s}$ process, compared to the $q\bar{q} \rightarrow s\bar{s}$ channel. On the other hand, the annihilation of light quarks into strange quarks is the main mechanism for creating strange quarks in pp collisions, where QGP formation is typically not expected. The enhancement factor (E) is defined as,

$$E = \frac{2}{\langle N_{part} \rangle} \left[\frac{\frac{dN_{AA}}{dy}\Big|_{y=0}}{\frac{dN_{pp}}{dy}\Big|_{y=0}} \right] \tag{1.8}$$

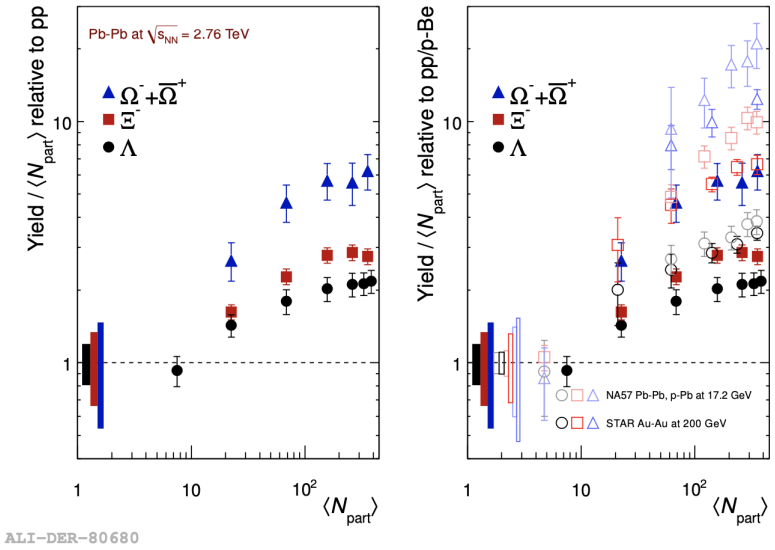

Figure 1.9: The yield of multi-strange hadrons in Pb-Pb collisions relative to pp collisions in ALICE (left) and NA57, STAR (right) as a function of $\langle N_{part} \rangle$ [12].

Where $\frac{dN_{AA}}{dy}\Big|_{y=0}$ and $\frac{dN_{pp}}{dy}\Big|_{y=0}$ are the integrated yields in heavy-ion and pp collisions, respectively, and $\langle N_{part} \rangle$ is the number of participants. The increased production of strange particles in Pb-Pb collisions (Fig. 1.9) suggests the formation of a deconfined state of matter at LHC energies, compared to small collision systems. Additionally, it is noted that particles with a higher number of strange quarks have a higher enhancement factor, meaning that $E(\Lambda) < E(\Xi) < E(\Omega)$. ALICE has also observed the enhanced production of strange particles in high multiplicity pp collisions, which is shown in Fig. 1.10.

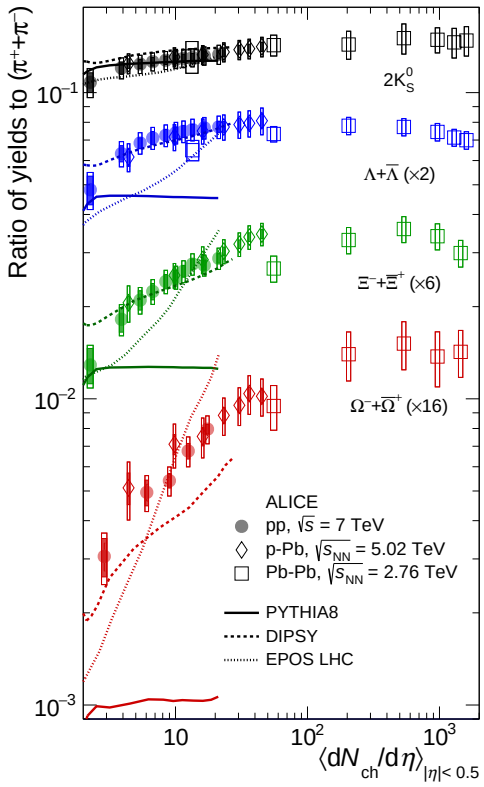

Figure 1.10: Integrated strange hadron-to-pion ratios as a function of charged particle multiplicities in pp, p–Pb, and Pb–Pb collisions at LHC energies [13].

1.5.2 Anisotropic flow

Elliptic flow is an important observable that helps us understand the initial condition and the overall behavior of the system. The initial spatial anisotropy created in non-central heavy-ion collisions is reflected in the momentum anisotropy of the final state particles, which is described as the elliptic flow (v_2).

The collective expansion of matter created in peripheral ultra-relativistic collisions results in spatial anisotropy of the initial density profile, resulting in final state momentum anisotropy due to the presence of pressure gradients. This phenomenon is called anisotropic flow. This can be measured with the azimuthal momentum anisotropy, which is the Fourier expansion in the azimuthal angle ϕ as follows:

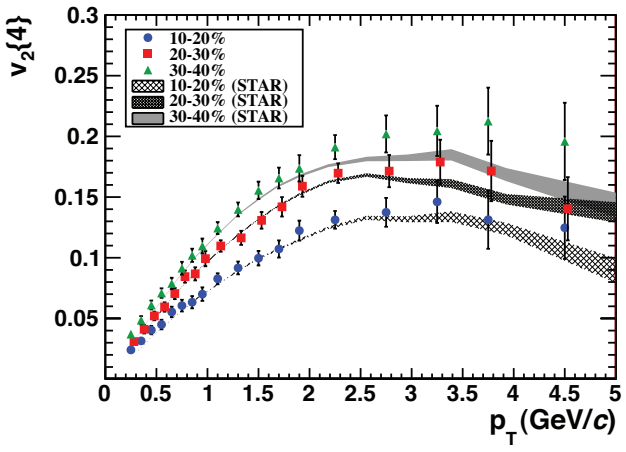

Figure 1.11: Elliptic flow of charged particles in Pb-Pb collisions at $\sqrt{s_{NN}} = 2.76$ TeV compared with Au-Au collisions at $\sqrt{s_{NN}} = 200$ GeV [10].

$$E\frac{d^3N}{dp^3} = \frac{d^2N}{2\pi p_{\mathrm{T}} dp_{\mathrm{T}} dy}\left(1 + 2\sum_{n=1}^{\infty} v_n \cos[n(\phi - \psi_R)]\right). \tag{1.9}$$

Where ψ_R is the event plane angle, v_n is the various order of flow harmonics, and v_1, v_2, and v_3 represent the directed, elliptic, and triangular flows, respectively. Fig. 1.11 displays the elliptic flow of charged particles, demonstrating the similarity between the dense media generated at RHIC and LHC. The availability of larger phase space and larger rescattering among partons at LHC accounts for the 30% higher value of v_2. In addition, this suggests that high-p_T partons thermalized earlier than RHIC.

1.5.3 Jet quenching

In relativistic heavy-ion collisions, jets are collimated sprays of high-p_T partons. These are created back-to-back to conserve four momenta. The production of jets in heavy-ion (A-A) collisions is different from pp collisions. If there is no medium present, i.e., any dijet produced in pp collisions will show two back-to-

back sharp peaks in the calorimeter; however, when a dijet is generated within QGP, the jet that travels farther through the medium loses more energy, leading to an imbalance in the two jets' four momenta. Therefore, the energy-losing jet seems to be suppressed when a medium is present. This phenomenon is called jet quenching. The hard partons interact with the thermalized partons in the medium, resulting in energy losses through collisions. It is a final state effect.

The final-state hadron yield at high-p_T is suppressed due to the quenching of high-p_T partons. This is usually expressed in terms of the nuclear modification factor (R_{AA}), which is the ratio between the yield in heavy-ion (A-A) collisions to pp collisions:

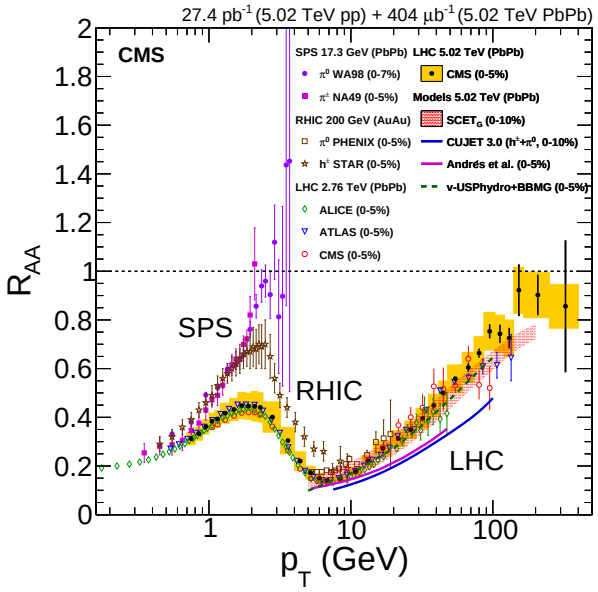

Figure 1.12: Nuclear modification factor R_{AA} for charged hadrons ($h^{\pm}$) and neutral pions (π^0) in the central heavy ion collisions at LHC, RHIC, and SPS [10].

$$\mathrm{R_{AA}} = \frac{\mathrm{d^2N^{AA}/dp_T d\eta}}{\langle \mathrm{N_{coll}} \rangle \mathrm{d^2N^{pp}/dp_T d\eta}} \tag{1.10}$$

where N^{pp} and N^{AA} are the charged-particle yields in pp and A-A collisions respectively. The mean number of binary collisions is $\langle N_{coll} \rangle = \sigma_{inel}^{NN} \langle T_{AA} \rangle$, where σ_{inel}^{NN} is the total inelastic nucleon-nucleon cross section and $\langle T_{AA} \rangle$ is the mean

nuclear thickness function. $R_{AA} = 1$, indicating the absence of QGP medium formation. However, any deviation of R_{AA} at high$-p_T$ from unity indicates quenching/enhancement in a high-density medium. Fig. 1.12 depicts the results of R_{AA} for charged hadrons ($h^{\pm}$) and neutral pions (π^0) in Pb+Pb and Au+Au collisions. RHIC and LHC energies showed the high-p_T suppression of hadrons in a dense QGP medium.

1.5.4 Quarkonia suppressions

Quarkonia is the bound state of a heavy quark and an anti-quark pair, basically charmonia ($c\bar{c}$) and bottomonia ($b\bar{b}$). These are expected to be formed at the early stages of the nuclear or hadronic collisions. Thus, quarkonia is an excellent probe for studying the early scenario of heavy-ion collisions. Because of the presence of deconfined partons in the QGP, the color charges screen the effective potential between heavy quarks to form quarkonia. So, it becomes more difficult to form a bound state of heavy quarks as the strength of the interaction between Q and $\bar{Q}$ decreases. This is known as Debye screening or color screening in QCD. Furthermore, the high temperature of the medium favors the dissociation of quarkonia. So, both these effects collectively suppress the quarkonia yield in A-A collisions.

Fig.1.13 (top) shows the R_{AA} of J/Ψ and $\Psi(2S)$ as a function of $\langle N_{part} \rangle$ in Pb-Pb collisions at $\sqrt{s_{\rm NN}} = 5.02$ TeV [14]. It is observed that J/Ψ and $\Psi(2S)$ are clearly suppressed due to the formation of QGP at the LHC energies. The availability of higher energy, however, also leads to a higher production of heavy quarks at the LHC. Thus a slightly enhancement of R_{AA} towards most central (higher $\langle N_{part} \rangle$) for both J/Ψ and $\Psi(2S)$. This is due to the regeneration of charmonia caused by the increased density of charm quarks in phase space. These regeneration effects are less at RHIC energies, which is shown in the bottom plot of Fig. 1.13. This plot clearly shows a larger suppression of J/Ψ at RHIC.

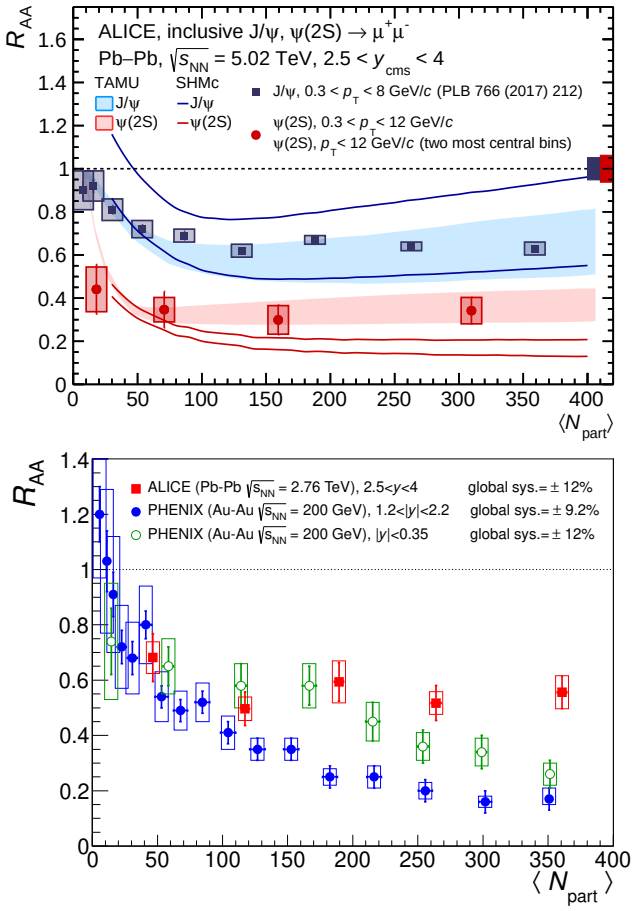

Figure 1.13: Nuclear modification factor (R_{AA}) showing the suppression of J/Ψ and $\Psi(2S)$ at the LHC(top) [14], and the bottom plot shows the R_{AA} of inclusive J/Ψ at the LHC compared to RHIC [15].

Additionally, it is noticed that $\Psi(2S)$ is more suppressed than J/Ψ as because $\Psi(2S)$ is the excited state of $c\bar{c}$, so it is weakly bound as compared to J/Ψ. So, less binding energy leads to greater suppression, as shown in FIg. 1.13 (top).

1.5.5 Electromagnetic Probes

Electromagnetic probes such as photons and dileptons provide additional insight into the characteristics of the QGP [16–18]. They interact only electromagnetically and thus escape the strongly interacting medium without further interac-

tions [19]. The photons and di-leptons are in the heavy ion collisions can be produced in the initial hard scattering process like annihilation ($q\bar{q} \rightarrow \gamma\bar{q}, q\bar{q} \rightarrow \gamma\gamma$), fragmentation ($qg \rightarrow gq^* \rightarrow q\gamma X$), Bremsstrahlung ($qg \rightarrow gq^* \rightarrow q\gamma g$), Compton ($qg \rightarrow \gamma q$) and pair production ($g\bar{q} \rightarrow l\bar{l}$). Additionally, they can be emitted by partons and hadrons during thermal equilibrium or through hadron decay. Direct photons (not from hadronic decays) provide a direct measurement of the initial QGP temperature through their thermal spectrum.

1.6 Thesis Structure and Organization

The major objective of this thesis is to understand the particle production mechanism in small system collisions through both heavy flavor and light flavor. In the data analysis, we studied particle production dynamics through the heavy flavor [Multiplicity-dependent of Charmonia production in pp collisions with ALICE], and in phenomenology, we studied particle production dynamics through the light flavor sector [global properties, anisotropic flow, nuclear modification factor in O-O Collisions at LHC energies]. The organization of the chapters in the thesis is presented below.

- **Chapter 1** introduces the Standard Model of particle physics and provides an overview of quantum chromodynamics (QCD), the framework describing strong interactions. It emphasizes two key properties of QCD: confinement and asymptotic freedom. Additionally, the Chapter explores the quark-gluon plasma (QGP), a state of primordial matter, along with its evolution over time and experimental indicators.

- **Chapter 2** covers the experimental setup, beginning with an introduction to the Large Hadron Collider (LHC) and a detailed description of A Large Ion Collider Experiment (ALICE). It highlights the key detector systems

essential for quarkonium production of $\Psi(2S)$ and J/Ψ. Additionally, the Chapter provides insights into the ALICE data acquisition system.

- **Chapter 3** presents the main experimental analysis on multiplicity dependence of charmonium production with ALICE. This includes the detailed analysis methodology of charged particle multiplicity in the mid-rapidity region and estimation of J/Ψ yield using the forward detectors. Finally, the invariant mass distribution, signal extraction, and evaluation of systematic uncertainty of J/ψ in different event classes have been reported.

- **Chapter 4** presents the phenomenological study of global properties, anisotropic flow, and nuclear modification factor in O-O collisions. This covers a brief introduction to a multiphase transport model (AMPT) for the Monte Carlo simulation in O-O collisions. The detailed analysis methodology of global properties estimation and the two-particle correlation technique for flow estimation is discussed.

- Finally, the conclusions drawn from the current studies are presented in **chapter 5**

Bibliography

[1] S. L. Glashow, Nucl. Phys. **22**, 579 (1961).

[2] A. Salam and J. C. Ward, Phys. Lett. **13**, 168 (1964).

[3] S. Weinberg, Phys. Rev. Lett. **19**, 1264 (1967).

[4] Wong, Cheuk-Yin. Introduction to High-energy Heavy-ion Collisions. Singapore, World Scientific (1994).

[5] H. Perkins, Introduction to High Energy Physics, Cambridge University Press (2012).

[6] G. L. Kane, Modern Elementary Particle Physics, Cambridge University Press (2017).

[7] A. Bazavov, T. Bhattacharya, M. Cheng, N. H. Christ, C. DeTar, S. Ejiri, S. Gottlieb, R. Gupta, U. M. Heller and K. Huebner, *et al.* Phys. Rev. D **80**, 014504 (2009).

[8] T. Niida and Y. Miake, AAPPS Bull. **31**, 12 (2021).

[9] F. Bellini, CERN-THESIS-2013-393.

[10] R. Pasechnik and M. Šumbera, Universe **3**, 7 (2017).

[11] https://particlesandfriends.wordpress.com/2016/10/14/evolution-of-collisions- and-qg

[12] B. B. Abelev *et al.* [ALICE], Phys. Lett. B **728**, 216 (2014) [erratum: Phys. Lett. B **734**, 409 (2014)]

[13] J. Adam *et al.* [ALICE], Nature Phys. **13**, 535 (2017).

[14] S. Acharya *et al.* [ALICE], Phys. Rev. Lett. **132**, 042301 (2024)

[15] B. Abelev *et al.* [ALICE], Phys. Rev. Lett. **109**, 072301 (2012).

[16] E. V. Shuryak, Phys. Lett. B **78**, 150 (1978).

[17] E. L. Feinberg, Nuovo Cim. A **34**, 391 (1976), CERN-TH-2156.

[18] G. Domokos and J. I. Goldman, Phys. Rev. D **23**, 203 (1981).

[19] P. Stankus, Ann. Rev. Nucl. Part. Sci. **55**, 517 (2005).

Chapter 2

Experimental Setup

2.1 Introduction

In the very beginning, right after the Big Bang, the universe was extremely hot and full of tiny particles. There were no atoms, stars, or planets just a thick soup of energy and particles. As time passed, the universe started to cool down. These tiny particles began to come together to form atoms, and over billions of years, stars, galaxies, and eventually life on Earth.

Humans have always been curious about how the universe began and what it is made of. Over many years, scientists have made great discoveries in learning about atoms and particles. But many questions still remain. What are the smallest building blocks of everything? How did the universe really begin?

To find these answers, scientists built the Large Hadron Collider (LHC) at CERN in Geneva. The LHC is the world's largest and most powerful machine. It accelerates tiny particles and causes them to collide, just like what happened right after the Big Bang. By studying these tiny collisions, scientists hope to learn more about how the universe works at its most basic level. The LHC is a huge step forward in our journey to understand where we come from and what

everything is made of. A Large Ion Collider Experiment (ALICE) is one of the main experiments at the LHC. It has been collecting data on hadronic and nuclear collisions for pp, p-Pb, Xe-Xe, and Pb-Pb. The purpose of ALICE is to study the physics of the quark-gluon plasma at extreme temperatures and energy densities in nucleus-nucleus and high-multiplicity hadronic collisions.

This chapter provides a detailed discussion of the ALICE detector at the LHC. It's divided into three sections. The first section 2.2 discusses the LHC in detail, including its various experiments. The second section 2.3 describes the ALICE detector system, with a particular emphasis on the detectors used for data analysis. The final section 2.4 focuses on the online-offline computing and reconstruction system built on the O2 framework.

2.2 The Large Hadron Collider (LHC)

The Large Hadron Collider is the world's most powerful and the largest particle accelerator. It is installed in an underground tunnel at a depth of 45-170 m across and 26.7 km in circumference along the France and Switzerland border [1]. It has several accelerating structures to boost the energy of the particles along the way. Two particle beams travel in opposite directions through two separate rings. They are guided by superconducting dipole magnets, powered by currents of up to 12 kA, and cooled to 1.9 K with liquid helium. They generate a magnetic field of 8.3 Tesla. Furthermore, quadrupoles allow for the focusing of particle beams, maximizing the probability of collision at the interaction point. Highly energetic hadron beams are pre-accelerated by a sequence of systems (Fig. 2.1) that increase the beam energy in a progressive way using older accelerators as injectors. These hadrons may be heavy nuclei or protons. The LHC is designed to accelerate proton beams up to a maximum energy for a beam of protons (lead ions) to be 7 TeV (2.76 TeV). This gives collision energies for pp collisions up to

$\sqrt{s} = 14$ TeV and for Pb-Pb collisions up to $\sqrt{s_{\mathrm{NN}}} = 5.5$ TeV.

Figure 2.1 depicts a schematic representation of the CERN accelerator complex. The four main experiments (ATLAS, CMS, LHCb, and ALICE) are also displayed. The accelerators at the CERN complex work sequentially to increase beam energy by increasing the size of the accelerator rings. To create a beam of protons, hydrogen gas is first ionized with an electric field, accelerating the protons to 750 keV. After that, the protons are fed into LINAC 2, accelerating them even more to 50 MeV. The proton beams then pass through the Proton Synchrotron Booster (PSB), Proton Synchrotron (PS), and Super Proton Synchrotron (SPS) in order to reach 450 GeV. Finally, it is injected into the LHC, where the beam energy increases from 450 GeV to 6.5 TeV. Under ideal circumstances, this process in the LHC only takes 20 minutes. Similarly, LINAC 3 provides Pb ions, which are then accelerated up to 72 MeV by the Low Energy Ion Ring (LEIR). The ion beams are then injected into the LHC, where they accelerate even more to reach the beam energy of 2.76 TeV per nucleon, after completing the same sequential acceleration chain through PS and SPS.

After entering the accelerator, two beams of particles with high energy, achieved by the chain of accelerators, travel nearly at the speed of light before colliding. In two separate tubes, known as beam pipes, which are maintained at an extremely high vacuum, the beams move in opposite directions. The beams are guided around the accelerator ring by a powerful magnetic field produced and managed by superconducting electromagnets. The bunches are now kept focused and accelerated to their final collision energy by the combination of electric and magnetic fields. Besides collision energy, instantaneous luminosity $\mathcal{L}$) is a key factor in achieving a high rate of particle collisions at the interaction points. The LHC has four primary detectors with varying objectives and dimensions based on the four Interaction Points (IPs) [Fig. 2.1] where collisions are produced. These

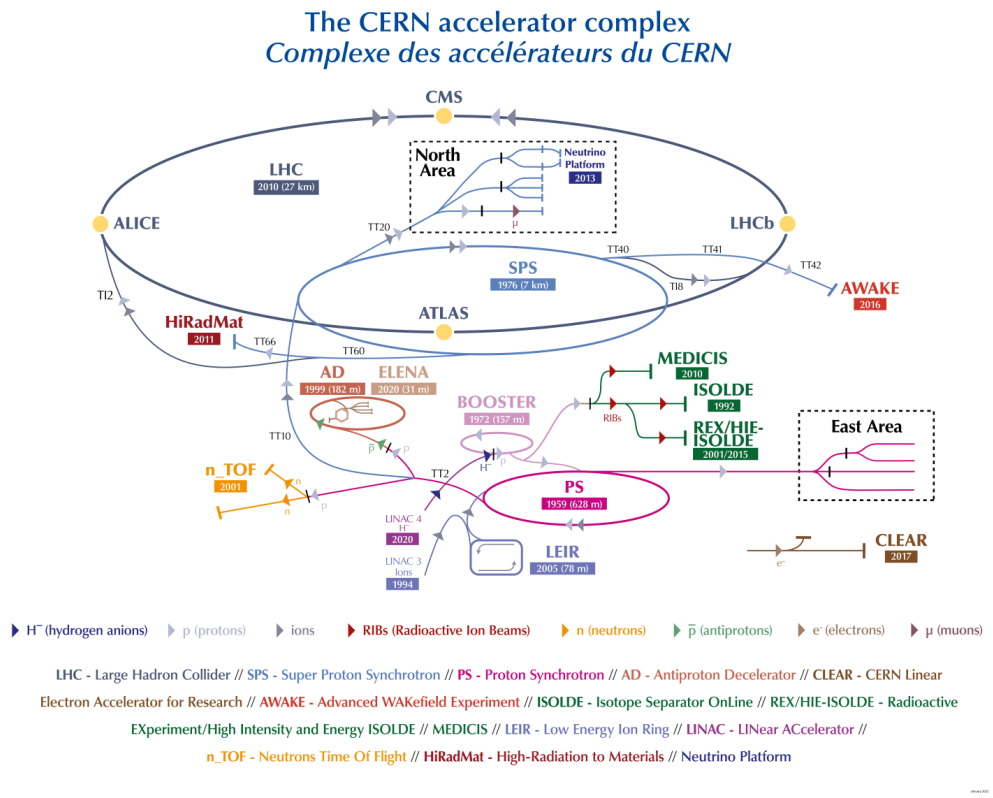

Figure 2.1: The CERN accelerator complex [2]

.

are:

- A Large Ion Collider Experiment (ALICE): It focuses on QGP studies and heavy-ion collisions. This experiment will be further detailed in the next section.

- A Toroidal LHC ApparatuS (ATLAS) [3]: The LHC's largest detector. It is a multifunctional detector that uses high luminosity pp collisions to investigate beyond SM physics and study the Higgs boson. It supports QGP research as well. ATLAS is shaped like a cylinder and has a toroidal magnetic system that produces a field of 2 T. This detector's acceptance in pseudorapidity is $|\eta| < 2.5$.

- Compact Muon Solenoid (CMS) [4]: CMS is a multi-purpose detector, just like ATLAS, which enables a complementary cross-check between the two collaborations operating separately. The detector is built around a big solenoid magnet that produces a 4 T field. $|\eta| < 2.5$ is the pseudorapidity region of this detector, and the minimum transverse momentum for muon measurements is between 1.2 and 3.5 GeV/c.

- LHC beauty (LHCb) [5]: The primary objective of the LHCb collaboration is to investigate matter-anti-matter asymmetry and the b-quark physics. The detector is a forward spectrometer made specifically to measure b-hadron decays. It covers an acceptance of $2 < |\eta| < 5$ and is made up of a dipole magnet with a bending power of 4 T m. In addition to the pp and heavy-ion runs, LHCb can operate in fixed-target mode by injecting noble gases (He, Ne, and Ar) into the LHC beam pipe near the interaction point.

The crossing of the colliding objects in the LHC experiments involves probabilistic processes. A given interaction's cross section σ quantifies its probability of occurring. This quantity is a universal property of the studied physical process. Similar to the interaction between two hard spheres, it can be classically viewed as the transverse section of the overlap region between the two objects at low energies. Its units are inverse-squared lengths.

Furthermore, LHC experiments focus on rare events with a small production cross-section σ. Therefore, a significant number of events are required in order to use statistical methods to study these processes. The collision rate is the number of inelastic collisions per unit of time that occur at a specific interaction point at the LHC, denoted by the symbol dR/dt. This rate increased from Run 2 to Run 3 in order to collect more events that will aid in the study of rare candidates. For Pb–Pb collisions, it will reach up to 50 kHz. The collision rate is calculated by multiplying the instantaneous luminosity $\mathcal{L}$ by the interaction cross section of

the colliding objects:

$$\frac{dR}{dt} = \mathcal{L} \cdot \sigma$$

Where σ represents the inelastic collision cross section. Thus, $\mathcal{L}$ has units of $cm^2 s^{-1}$. This luminosity is one of the key features of accelerators like the LHC. It measures the particle accelerator's ability to generate a large number of interactions, or collisions. The integrated luminosity L_{int}, which measures the quantity of events recorded over a specific time period, can also be defined as follows:

$$L_{\text{int}} = \int \mathcal{L}\, dt = \int \frac{1}{\sigma} \times \frac{dR}{dt}\, dt \tag{2.1}$$

During Run 3, the LHC instantaneous luminosity is expected to reach (2×10^{34} $\text{cm}^{-2}\text{s}^{-1}$). The High Luminosity LHC upgrade (HL-LHC) aims to increase the instantaneous luminosity at the LHC up to 5×10^{34} $\text{cm}^{-2}\text{s}^{-1}$ for the ATLAS and CMS experiments, while the collimation and focusing magnets are not adapted in ALICE and LHCb due to the specific needs of these experiments [6].

2.3 A Large Ion Collider Experiment (ALICE)

ALICE (A Large Ion Collider Experiment) is a detector at the LHC that studies Quark-Gluon Plasma (QGP) via collisions of protons, nuclei, and heavy ions accelerated in the LHC [7]. It measures 26 meters in length, 16 meters in width, and 16 meters in height, weighing approximately 10,000 tons. This experiment was designed to investigate low-momentum particles such as heavy-flavor hadrons, low-mass dileptons, and quarkonia in collisions. It is thought that this hot, dense state of matter persisted for a few millionths of a second after the Big Bang. The purpose of the ALICE detector's design is to recreate and investigate this state of matter. Its primary characteristics include its exceptional ability to identify particles using specific energy loss, time of flight, electromagnetic calorimetry, muon

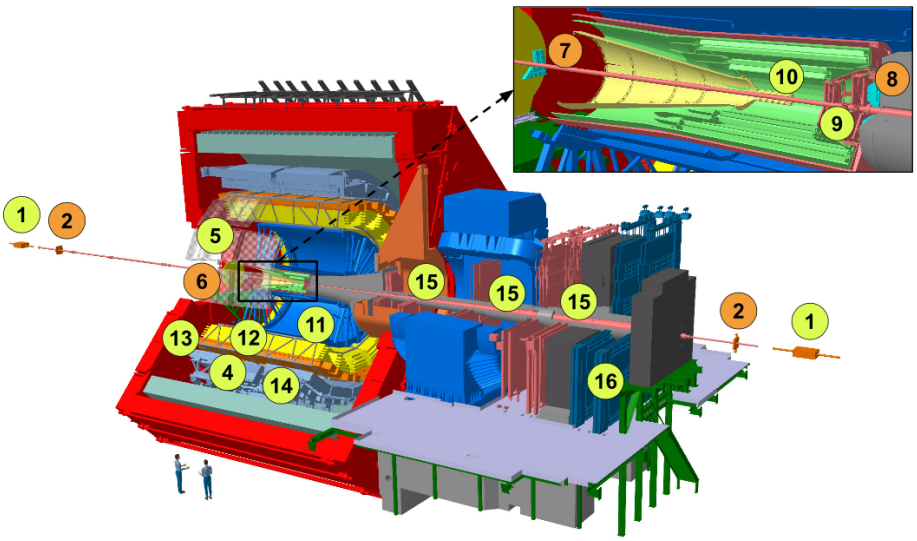

1. **ZDC** – Zero Degree Calorimeter
2. **FDD** – Forward Diffractive Detector
3. **EMCal** – Electromagnetic Calorimeter
4. **DCal** – Di-jet Calorimeter
5. **HMPID** – High Momentum Particle Identification Detector
6. **FV0** – FVzero
7. **FT0-A** – FTzero A-side
8. **FT0-C** – FTzero C-side
9. **MFT** – Muon Forward Tracker
10. **ITS** – Inner Tracking System
11. **TPC** – Time Projection Chamber
12. **TRD** – Transition Radiation Detector
13. **TOF** – Time-of-Flight Detector
14. **PHOS** – Photon Spectrometer
15. **MCH** – Muon Tracking Chambers
16. **MID** – Muon Identifier

Figure 2.2: Schematic Layout of ALICE detector at LHC in the RUN3 setup [8].

spectrometry, etc. These capabilities, in turn, enable detailed studies of hadrons, electrons, muons, and photons produced in the collisions, extending down to very low transverse momenta.

ALICE is made up of various sub-detectors (Fig. 2.2) that serve different purposes, which we will explain below. Particle multiplicity and collision time are measured by global detectors, which are positioned around the interaction point. Charged particles at midrapidity can be tracked and identified using the central barrel detectors.

The z-axis and the beam pipe direction coincide in the Cartesian ALICE coor-

dinate system. The A-side, or positive z, is pointed in the direction of the ATLAS experiment. The CMS experiment is indicated by the C-side, which is oriented in the opposite direction. The x-axis points toward the LHC's center and is the horizontal plane. The y-axis is pointing up.

2.3.1 Inner Tracking System 2 (ITS2)

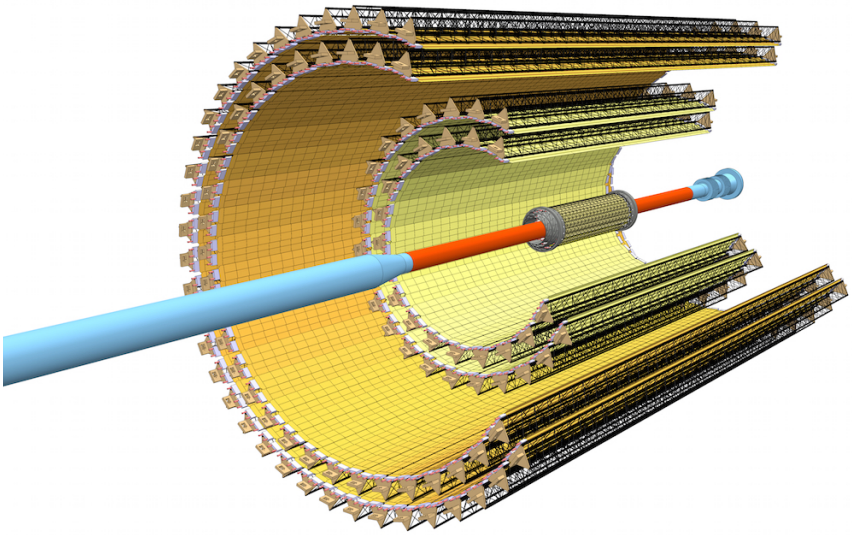

Figure 2.3: Structural Overview of the ITS2 System [9].

The Inner Tracking System 2 (ITS2) plays a central role in precisely determining the primary vertex of the collisions and the secondary vertices of heavy hadron decays at mid-rapidity, as it is closest to the beam pipe [11]. It also allows for tracking down to low p_T and improves TPC momentum and angular resolution. It consists of seven silicon layers surrounding the interaction point (Fig. 2.3), with the pseudorapidity region $|\eta| \leq 1.3$ and full azimuthal coverage. It is based on the ALice PIxel DEtector (ALPIDE) chips. Its sensors provide higher pointing resolution due to their reduced proximity to the interaction point, as well as better spatial resolution than the original ITS utilised during LHC Runs 1 and 2.

The ITS2 is designed to withstand the high hit densities associated with nominal operating circumstances, resulting in robust performance in pp and Pb-Pb collisions. A total of 10 m^2 is the surface area of active silicon. The impact parameter resolution it offers is ~ 25 μm in both $r\varphi$ and z dimensions [11]. The location of ITS2 is 21 mm away from the interaction region.

2.3.2 The Time Projection Chamber (TPC)

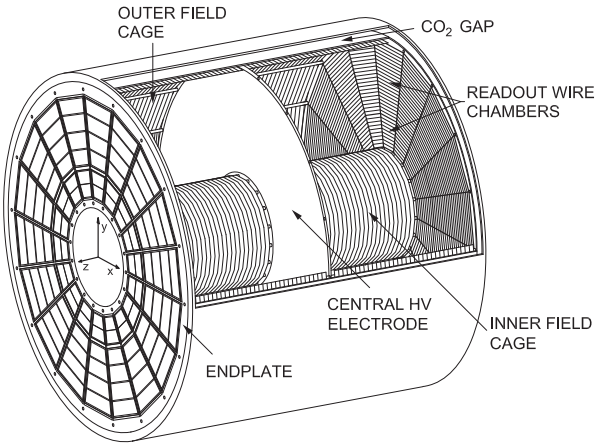

Figure 2.4: Schematic drawing of the ALICE TPC [10].

This is a 90 m^3 cylinder (Fig. 2.4) filled with $Ne - CO_2 - N_2$ gas, with the acceptance $|\eta| \leq 0.9$ and full azimuthal coverage [12]. The gas will become ionized when a charged particle enters the detector. According to Gas Electron Multipliers (GEM), an electric field will cause the secondary electrons that are created to drift in the direction of the TPC end plates. Particle identification, tracking, and momentum measurements of the charged particle are made possible by the information these end-plates provide.

2.3.3 The Time Of Flight detector (TOF)

It is made up of a cylindrical array that is 3.7 meters away from the interaction point. It is divided into 18 sectors using Multigap Resistive Plate Chambers. Its

acceptance range is $|\eta| \leq 0.9$, with full azimuthal coverage [13]. TOF measures the time at which the particle passes through the detector, with a resolution of more than 50 ps. This measurement determines particle velocity and identifies protons ($p_T < 4$ GeV/c), pions, and kaons ($p_T < 2.5$ GeV/c).

2.3.4 The Transition Radiation Detector (TRD)

It consists of a cylinder around the TPC with a diameter of 7 m, covering the pseudorapidity region of $|\eta| \leq 0.84$ and with full azimuthal coverage. It consists of six MWPC chambers with a drift region and an amplification. It provides tracking information to supplement the other central barrel detectors and differentiates between electron-pion particles with $p_T \geq 1$ GeV/c [14].

2.3.5 The ElectroMagnetic Calorimeter (EMCal)

It includes the azimuthal region ($\Delta\varphi = 110°$) and the pseudorapidity region ($|\eta| \leq 0.7$). It's a Pb-scintillator sampling calorimeter with multiple layers [15]. It identifies particles as photons and neutral mesons via the photonic decay channel.

2.3.6 The PHOton Spectrometer (PHOS)

It covers the azimuthal range of $\Delta\varphi = 70°$ and the pseudorapidity region $|\eta| \leq 0.12$ [16]. It is made up of an electromagnetic calorimeter that measures photons and neutral mesons through their photonic decay channels.

2.3.7 The High Momentum Particle Identification Detector (HMPID)

It lies inside the pseudorapidity region $|\eta| \leq 0.6$, including the azimuthal range $\Delta\varphi = 58°$. It is based on the technology known as Ring Imaging CHerenkov

(RICH). For pion, kaon, and proton separation, it offers extra identifying information [17].

2.3.8 The Fast Interaction Trigger detector (FIT)

It is made up of three detectors (Fig. 2.7), which are positioned between −19.5 and 17 meters from the interaction point (IP) along the beam pipe [18].

2.3.8.1 The FT-zero (FT0) detector:

It is made up of two detectors, FT0A and FT0C, each of which has twelve Cherenkov counters and is situated on either side of the interaction point. The FT0 covers $3.5 < \eta < 4.9$ (FT0A) and $-3.3 < \eta < -2.1$ (FT0C). This detector establishes a start time for the TOF detector by determining the vertex position of the collisions and providing an accurate collision time with a resolution of 25 ps.

2.3.8.2 The FV-zero (FV0) detector:

This large scintillator disk is segmented into five concentric rings with equal coverage of pseudorapidity. The ring with the smallest inner diameter is 8 cm, while the largest has an outer diameter of 144 cm. The information from this segmentation and the other forward detectors is enough to produce the necessary event plane resolution and centrality. FV0 and FT0 work together to provide the input required to produce multiplicity and minimum bias triggers.

2.3.8.3 The Forward Diffractive Detector (FDD):

It consists of two subdetectors positioned on opposite sides of the interaction point (IP). It covers the pseudorapidity ranges $4.7 < \eta < 6.3$ and $-6.9 < \eta < -4.9$. Each array contains eight rectangular scintillator pads. The FDD helps in

selecting ultra-peripheral collisions and measuring the diffractive cross section. It also provides a centrality measurement based on the charged-particle multiplicity.

2.3.9 The Zero Degree Calorimeter (ZDC)

It is a detector composed of two hadronic calorimeters for proton (ZP) detection, two for neutron (ZN) detection, and two electromagnetic (ZEM) calorimeters. Photomultipliers read the data from each of these calorimeters, which are Cherenkov detectors made of quartz fibers. When charged particles travel faster than the speed of light in quartz, they produce Cherenkov light, which is then captured and intensified. The two hadronic calorimeters detect spectator nucleons that emerge at 0° from the collisions and are located at $z = \pm$ 112.5 m from the nominal interaction point [19]. Both electromagnetic calorimeters are positioned seven meters from the interaction point in the experiment's forward region. They measure the energy that photons deposit at forward rapidity. By measuring the energy deposited by the spectator nucleons, the ZDC is primarily used to eliminate parasitic beam-gas background events and to ascertain the centrality in pPb and Pb–Pb collisions.

2.3.10 The Muon spectrometer

The Forward Muon Spectrometer of ALICE [20] is primarily used to measure the production of low mass mesons (ρ, ω, ϕ) and heavy quarkonia ($J/\psi, \psi(2S), \Upsilon(1S), \Upsilon(2S)$ via their dimuon ($\mu^+\mu^-$) decay channel. The production of single muons from the decays of $W^{\pm}$, Z^0 bosons, and heavy-flavor hadrons (D and B mesons) is also measured by the detector. A pseudorapidity range of $-4 < \eta < -2.5$ corresponds to the spectrometer's angular acceptance between $171° < \theta < 178°$. It is made up of an inner beam shielding, front and rear absorbers, a dipole magnet, and muon tracking and muon identifier stations that are separated by an iron wall (Fig. 2.5). The front absorber's position between the spectrometer and the interaction point

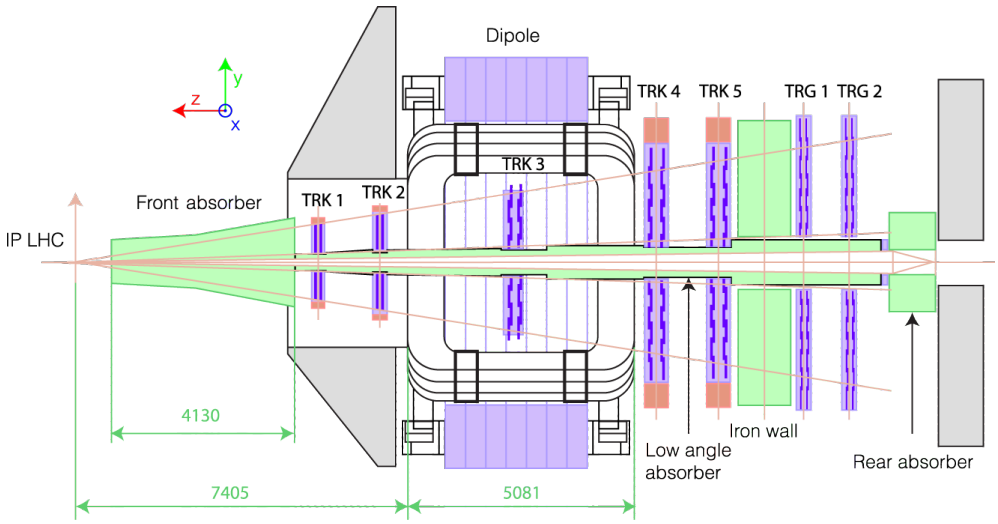

Figure 2.5: Schematic of the ALICE Muon Spectrometer [21].

causes multiple scattering in tracks extrapolated to the IP, which significantly reduces resolution. As a result, the exploitable physics program is subject to restrictions, specifically the inability to distinguish between open charm and beauty contributions.. In order to get around these restrictions for Run 3, the Muon Forward Tracker (MFT) was placed between the front absorber and the interaction point in front of the muon spectrometer. The upcoming chapter will focus on this new detector.

2.3.10.1 System absorber and shielding

The Muon Spectrometer must include absorbers and shielding due to the large background environment in central Pb-Pb collisions. The Muon Spectrometer consists of four distinct components: the front absorber, the beam shield, the iron wall, and the rear absorber.

- **Front absorber:** The ALICE solenoid magnet L3 contains the front absorber (Fig. 2.6), which is 4.13 meters long overall. A good shielding of hadrons from the IP and background from $\pi, K \rightarrow \mu$ is provided by the optimized absorber design. Additionally, it reduces muon multiple scatter-

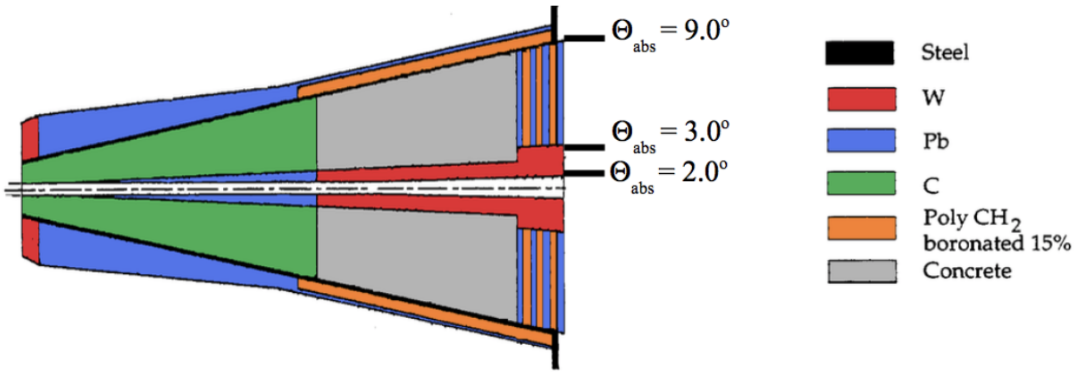

Figure 2.6: Schematic view of front absorber of the ALICE Forward Muon Spectrometer [22].

ing, which shouldn't affect the spectrometer's mass resolution. A layout of the front absorber is shown in Fig 2.6. Carbon, a low-Z material, is used near the IP to reduce the effects of multiple scattering. In order to absorb low-energy protons and neutrons as well as secondary particles created in the absorber, the back portion is composed of concrete and multiple layers of lead and boronated polyethylene. The absorber's exterior is coated with lead and boronated polyethylene to prevent the recoil particles from reaching the TPC. To absorb background particles from beam-gas interactions, the beam is covered by an inner shield composed of tungsten.

- **Beam shield:** The tracking chambers are protected by the small-angle beam shield, which lowers background particles created in the beam pipe. It is composed of stainless steel, lead, and tungsten. Its conical geometry extends up to a maximum radius of 30 cm along the spectrometer's length, following the 178° acceptance line.

- **Iron Wall:** The tracking chambers can be adequately protected by the beam shield and front absorber, but the trigger chambers need extra defense. This is why the muon filter, an iron wall that is 1.2 meters thick ($\approx 7.2\ \lambda_{int}$), is positioned in front of the first trigger chamber after the last

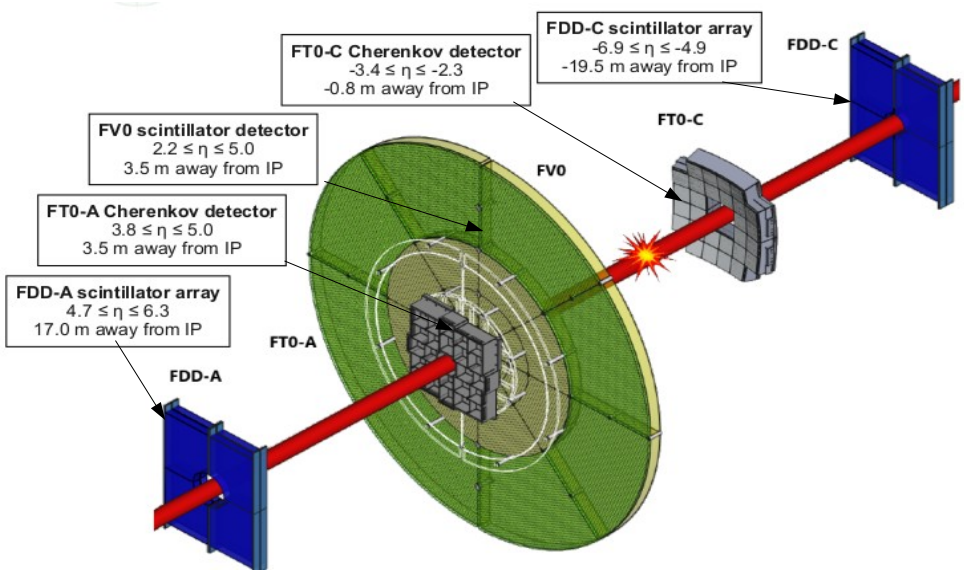

Figure 2.7: Illustration of the FIT layout [23].

tracking chamber. The front absorber and muon filter prevent muons with momenta smaller than 4 GeV/c.

- **Rear absorber**: This is the extra shielding at the rear of the trigger chambers that protects against beam gas interactions created in the LHC tunnel's beam pipe.

2.3.10.2 The dipole magnet:

It is located 7 meters from the interaction point (IP) and has dimensions of 5 meters in length, 6.6 meters in width, and 8.6 meters in height. It generates a magnetic field with a bending power of 3 T·m. In the ALICE coordinate system, the magnetic field is oriented perpendicular to the bending plane, defined as the (yz) plane. As charged particles traverse the field, they are deflected, allowing for the measurement of their curvature and thus, their momentum and electric charge.

2.3.10.3 The Muon CHamber (MCH):

It has five stations, each with two cathode pad chambers, and is situated between 5.2 and 14.4 meters from the IP. It comprises low-Z materials like carbon fibers; their design was optimized to reduce the scatterings that can occur during the muons' passage. Composed of a central anode wire positioned between two cathode planes, they comprise cathode pad chambers with a high granularity (~ 2)% occupancy in central Pb-Pb collisions at $\sqrt{s_{NN}} = 2.76$ TeV [24]. The gas mixture that fills the chambers consists of CO_2 (20%) and argon (80%). A particle moving through will therefore ionize the volume, releasing electrons that will move to a nearby cathode and produce a signal.

2.3.10.4 The Muon Identification (MID):

It is situated behind the iron wall filter, 16 meters from the IP. Each of its two stations is constructed from two resistive plate planes. These plates are made up of gas-filled electrodes spaced two millimeters apart. An avalanche of secondary electrons is created when charged particles cross paths. When a muon travels through these chambers, the response time is approximately 2 ns. However, this detector's readout frame is longer, roughly 25 ns, as will be discussed later.

2.4 ALICE online and offline system

2.4.1 Continuous readout and Online-Offline processing: ALICE

During the Long Shutdown 2 (from 2018 to late 2021), prior to the start of Run 3, the detector electronics were improved to enable an operational mode known as "continuous readout" [25]. This means that the detectors are continuously read for the entire duration of the physical fill. This is in contrast to the pre-

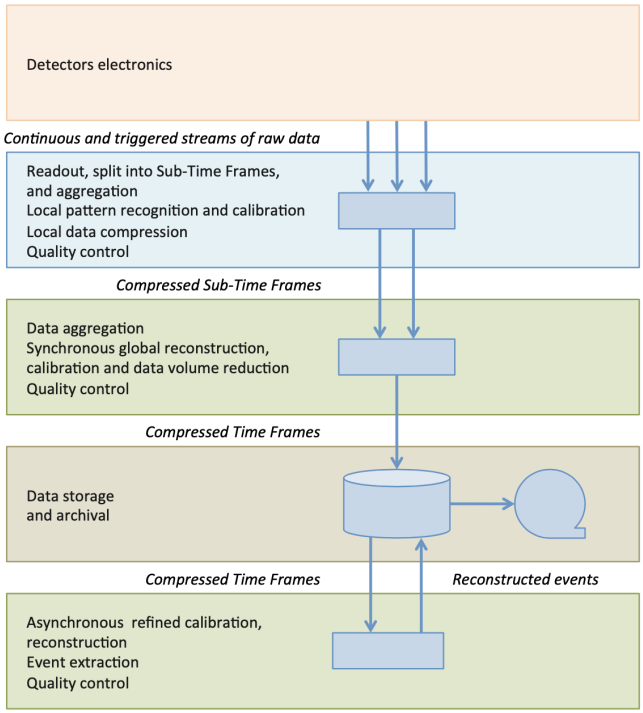

Figure 2.8: A full scheme of the online-offline computing system [26].

vious mode of operation used in Runs 1 and 2, which relied on start-of-readout signals delivered by dedicated hardware, known as triggers, when various types of signals indicating valuable events were detected. A clock signal propagated from the LHC radio-frequency cavities (the "beam" clock) is sent to all detectors operating in the continuous mode to ensure synchronization. This enables each piece of readout data to be timestamped with the accuracy of an LHC bunch crossing of ≈ 25 ns.

The data stream from the detector's front-end electronics is routed to the data acquisition system, which consists of Local Trigger Units connected to Common Readout Units (CRUs). The raw detector data from the CRUs is then sent to the processing farms, which are outfitted with the new Online-Offline (O2) software environment. There, the First Level Processors (FLPs) receive it and send it to the Event Processing Nodes (EPNs)[3] following some local processing. The

continuous data stream is handled by this processing chain by breaking it up into time frames (TFs).

The data stream from the detector front-end electronics is distributed to the data acquisition system, which is comprised of Local Trigger Units connected to Common Readout Units (CRUs). It is then directed to the processing farms, equipped with the new Online-Offline (O2) software environment, where the First Level Processors (FLPs) receive the raw detector data from the CRUs and send them after some local treatment to the Event Processing Nodes (EPNs)[3]. This processing chain handles the continuous data stream by dividing it into chunks named time frames (TFs). In order to expedite the data treatment process, this architecture is built to run the reconstruction over one of these time chunks and process independent ones in parallel (one TF per EPN). It also runs algorithms to compress and skim the data. The raw data generated by the detector's front-end electronics is approximately ≈ 3.4 TB^{-1}. By using FLPs, the data is compressed to 900 GBs^{-1}. At the end of the reconstruction's intermediate step (i.e., the synchronous or online part), the EPN farm's output is 130 GBs^{-1} [25]. One of the goals of Run 3 is to study rare events, like heavy flavors, and this continuous readout and data reduction enable an effective use of the enhanced luminosity to be delivered 2 Upgrade TDR by the OLHC in Run 3, resulting in a considerable improvement in statistics and performance.

A Time Frame (TF) is a unit of time and is defined as a fixed number of LHC orbits. One LHC orbit is completed in $\sim$89 μs or 3564 bunch crossings (BC). In the 2021 commissioning and regular data collection period, 1 TF = 128 LHC orbits, or 11.3825 ms. On average, there are 569 Pb-Pb collisions at a 50 kHz interaction rate [25]. In 2023, it was reduced to 1 TF = 32 LHC orbits because of the fluidity of the synchronous processing.

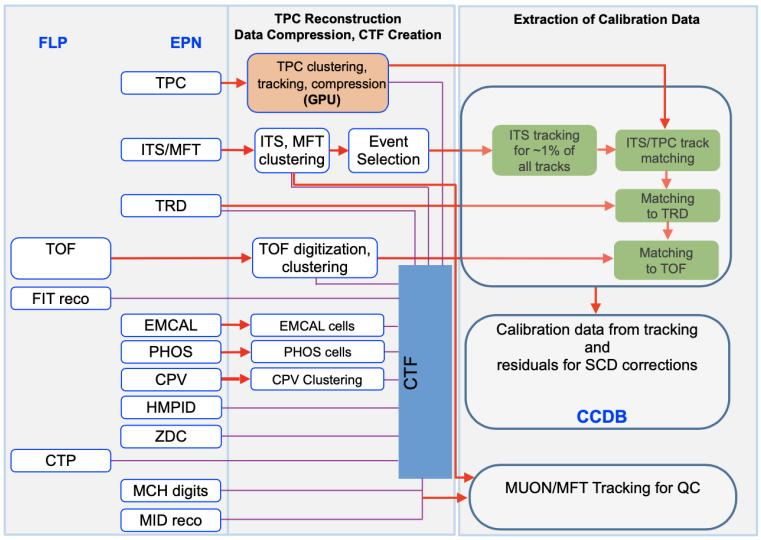

Figure 2.9: Illustration of the different processes of synchronous reconstruction workflow [25].

Detailed descriptions of the synchronous and asynchronous processing are shown in Fig. 2.8 and Fig. 2.9.

- Each TF is further subdivided into sub-time frames (STFs). The data from a sub-part of the ALICE detector during an LHC orbit is represented by an STF. Parallelized synchronous (online) processing on the FLPs is followed by the STFs. It should be noted that, depending on the detector, FLPs can also carry out calibration tasks. Additionally, a specific FLP is utilized to gather and process data from the Detector Control System (DCS). It processes and saves conditions related to the detector, such as temperature or voltage, in calibration objects that are kept in the Condition and Calibration Database (CCDB). Later on, such as in asynchronous phases or physics analysis, they can be accessed.

- The FLPs send all of the compressed STFs that are part of the same TF to a specific EPN for aggregation (TF building).

- The synchronous reconstruction will be completed on the EPN farm [4]. The

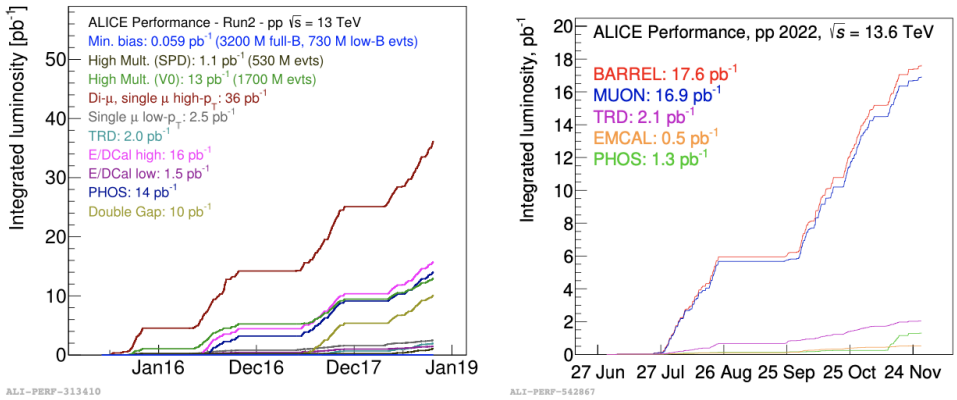

Figure 2.10: Integrated luminosity for various triggers in pp collisions at $\sqrt{s} =$ 13 TeV during Run 2 (Left), Integrated luminosity for pp collisions at $\sqrt{s} = 13$ TeV taken in 2022 (right) [27].

main goal of synchronous processing is to reduce the data rate, particularly from the TPC, which accounts for the majority of raw data volume. This is accomplished by clustering, full track reconstruction, and removing background hits from the data. The compressed data is organized into compressed time frames (CTFs) and saved to a semi-permanent disk buffer.

- Following the synchronous stage, the asynchronous stage occurs, in which data reconstruction and final calibrations using CCDB-stored objects are performed on EPNs and in the GRID environment. The final output is the Analysis Object Data (AOD), which is saved on permanent disk storage. These objects store information about the reconstructed tracks left by particles in the detectors. All of the physics analyses that follow make use of the produced objects.

2.4.2 Data taking performances in early Run 3

The continuous readout architecture of Run 3 is designed to achieve precise measurements in the open heavy-flavor or low-mass dilepton sector. Because these

processes do not have signatures that can be easily distinguished by hardware triggers, they can only be collected satisfactorily with a zero-bias (minimum-bias) interaction trigger, which corresponds to an event with at least one inelastic collision. At the start of Run 3, in 2022, pp data was mostly recorded at a 500 kHz interaction rate. Fig. 2.10 (right) shows the integrated luminosity during this time period, which can be compared to the one accumulated over the entire duration of Run 2 (left). The lower collected luminosity in comparison to the Muon and Barrel detectors can be explained by the fact that the EMCAL detector is still using legacy triggered mode because the readout electronics were not upgraded. Because of the old data acquisition system's limited bandwidth, the muon integrated luminosity sampled by the continuous mode in 2022 is already nearly half of the dimuon triggered luminosity of Run 2 and more than six times the low-pT muon luminosity (recorded with a specific and down-scaled trigger in Run 2).

2.5 Summary

This chapter provides an in-depth overview of the ALICE (A Large Ion Collider Experiment) detector at the Large Hadron Collider (LHC), designed to study the Quark-Gluon Plasma (QGP) produced in high-energy nuclear collisions. It begins with a brief introduction to the LHC, the world's largest and most powerful particle accelerator, located at CERN. The LHC accelerates particles to near-light speeds and collides them at designated interaction points monitored by major detectors: ALICE, ATLAS, CMS, and LHCb. ALICE is uniquely optimized for studying heavy-ion collisions and rare processes at low transverse momentum.

The chapter elaborates on the major sub-detectors in ALICE, such as the Inner Tracking System (ITS2), Time Projection Chamber (TPC), Time of Flight (TOF), Transition Radiation Detector (TRD), Electromagnetic Calorimeters (EM-

Cal and PHOS), and Muon Spectrometer. Each subsystem is designed to track and identify particles like electrons, photons, muons, and hadrons with high precision across various rapidity ranges. The Muon Spectrometer, in particular, plays a crucial role in measuring heavy quarkonia via dimuon decays.

The chapter also discusses the upgraded continuous readout and online-offline (O^2) data processing system introduced in Run 3. This system enables real-time data acquisition, reconstruction, and compression to handle high collision rates efficiently. It supports detailed analysis of rare probes by dividing data into "time frames" and allowing parallel processing on dedicated computing farms. The chapter concludes by highlighting the performance improvements seen in early Run 3 operations, particularly for minimum-bias triggers and low-p_T particle measurements.

Bibliography

[1] L. Evans and P. Bryant, JINST **3**, S08001 (2008).

[2] The CERN accelerator complex https://cds.cern.ch/record/2800984/

[3] G. Aad *et al.* [ATLAS], JINST **19**, P05063 (2024).

[4] S. Chatrchyan *et al.* [CMS], JINST **3**, S08004 (2008).

[5] A. A. Alves, Jr. *et al.* [LHCb], JINST **3**, S08005 (2008).

[6] G. Apollinari, O. Brüning, T. Nakamoto and L. Rossi, CERN Yellow Rep., no.5, 1-19 (2015).

[7] K. Aamodt *et al.* [ALICE], JINST **3**, S08002 (2008).

[8] S. Upadhyaya, Int. J. Mod. Phys. A **40**, 2444006 (2025).

[9] F. Reidt [ALICE], Nucl. Instrum. Meth. A **1032**, 166632 (2022).

[10] A. Mathis [ALICE], EPJ Web Conf. **174**, 01002 (2018).

[11] B. Abelev *et al.* [ALICE], J. Phys. G **41**, 087002 (2014).

[12] C. Lippmann [ALICE], CERN-LHCC-2013-020.

[13] A. Akindinov, A. Alici, A. Agostinelli, P. Antonioli, S. Arcelli, M. Basile, F. Bellini, G. Cara Romeo, L. Cifarelli and F. Cindolo, *et al.* Eur. Phys. J. Plus **128**, 44 (2013).

[14] S. Acharya *et al.* [ALICE], Nucl. Instrum. Meth. A **881**, 88-127 (2018).

[15] P. Cortese *et al.* [ALICE], CERN-LHCC-2008-014.

[16] G. Dellacasa *et al.* [ALICE], CERN-LHCC-99-04.

[17] G. Volpe [ALICE], Nucl. Instrum. Meth. A **876**, 133-136 (2017).

[18] A. I. Maevskaya [ALICE], EPJ Web Conf. **204**, 11003 (2019).

[19] G. Dellacasa *et al.* [ALICE], CERN-LHCC-99-05.

[20] C. Finck [ALICE Muon Spectrometer], J. Phys. Conf. Ser. **50**, 397 (2006).

[21] Addendum of the Letter of Intent for the upgrade of the ALICE experiment : The Muon Forward Tracker. https://cds.cern.ch/record/1592659

[22] [ALICE], CERN-LHCC-99-22.

[23] A. Maevskaya [ALICE], Phys. Atom. Nucl. **84**, 579 (2021).

[24] B. B. Abelev *et al.* [ALICE], Int. J. Mod. Phys. A **29**, 1430044 (2014).

[25] S. Acharya *et al.* [ALICE], JINST **19**, P05062 (2024)

[26] P. Buncic, M. Krzewicki and P. Vande Vyvre, CERN-LHCC-2015-006.

[27] M. Coquet, Probing the quark-gluon plasma at the LHC: study of charmonia with the ALICE detector and thermal dileptons phenomenology, https://theses.hal.science/tel-04337446v1.

Chapter 3

Charmonia production as a function of charged particle multiplicity in pp collisions at $\sqrt{s} = 13.6$ TeV with ALICE

3.1 Introduction

Charmonia are bound states consisting of a charm and an anti-charm quark. The production of heavy quarks and the formation of a bound state are the two stages of their production. The first stage is described by perturbative QCD and occurs during initial hard parton-parton scatterings with large momentum transfer. The second phase is a non-perturbative process that involves soft momentum scales and long-distance interactions. At LHC energies, multiple parton interactions (MPI) can occur within a single pp collision, influencing both soft particle production and heavy-flavour yields. Therefore, it is essential to investigate the interaction between hard and soft processes, the function of MPI, and potential collective phenomena in small systems by examining J/ψ production as a function of charged-particle multiplicity.

The analysis presented here is based on the data collected in 2024 by the upgraded ALICE detector during LHC Run3, which provides higher statistics

than previous data-taking periods. This thesis reports the self-normalized J/Ψ yield as a function of the normalized charged-particle in pp collisions at $\sqrt{s}$ = 13.6 TeV in the dimuon channel using INEL > 0 events is studied.

3.2 Data and Monte Carlo samples

3.2.1 Data:

The present analysis is carried out for pp collisions at $\sqrt{s}$ = 13.6 TeV, and the data samples are collected in 2024 for the estimation of multiplicity distribution. The list of runs is presented in Appendix 3.8. For the estimation of the J/ψ and $\psi(2S)$ yields, we have used a skimmed dataset of LHC24-pass1-skimmed.

3.2.2 Monte Carlo:

The Monte Carlo sample (LHC24f4d) is used for general-purpose studies are anchored to apass1 pp collisions at $\sqrt{s}$ = 13.6 TeV, corresponding to the 2024 run conditions. The samples are detailed in Table 3.1.

MC Production period	
MC Data	**Anchored to**
LHC24f4d	2024 - pass1 (PYTHIA8)

Table 3.1: MC Production periods and their anchoring.

3.2.3 Event Selection

In this analysis, the event selection applied is *eventStandardSel8ppQuality*. This cut will remove the ambiguous track contribution at the event selection level. Minimum bias events are selected (sel8), events in time frames (TF) border are removed to avoid tracks coming from the same events splitting in different TF,

and a selection on the primary vertex position is applied to ensure good vertex reconstruction efficiency and compatibility with the Monte Carlo description. The included cuts are listed below:

- isSel8 = True: Ensures that the event passes the minimum-bias trigger (Sel8).
- VtxZ: -10 to 10: Selects events with the primary vertex within ±10 cm along the beam axis.
- isNoTFBorder = True: Rejects events with vertices at the edges of the Time Frame to avoid border effects.
- isNoITSROFBorder = True: Removes events close to the ITS readout-frame border to prevent timing mismatches.
- isNoSameBunch (No collisions with same T0 BC) = True: Excludes events from the same bunch crossing.
- isGoodZvtxFT0vsPV = True: No collisions with difference > 1 cm between Z_{PV}^{tracks} and Z_{PV}^{FT0A-C}
- isVertexITSTPC = True: Requires a reconstructed vertex using both ITS and TPC tracks.
- isVertexTOFmatched = True: Ensures the vertex has TOF-matched tracks.
- Zorro selection = True: Applies additional quality cuts from the Zorro framework.
- Zorro trigger = fDimuon: Selects events triggered by the dimuon trigger.
- Split Collisions = true: Rejects split (duplicate) collisions.

3.2.4 Muon track selection

Data selections are performed on single tracks and reconstructed dimuon pairs:

- Single muon track within the muon spectrometer acceptance: $-4.0 < \eta < -2.5$.
- The MCH-MID track match requirement: track type 3
- Radial position of (R_{abs}) of the muon track is $17.6 < R_{abs} < 89.5$.
- No p_T cut is applied in the single muon level.
- fwdtrack-to-collision associator: time
- Remove collision splitting candidates: true

3.3 Multiplicity measurement

For the current analysis, the number of tracks reconstructed in the pseudo-rapidity range $|\eta| < 0.8$ has been used as an event multiplicity estimator. The z-vertex position has to be constrained to $|z| < 10$ cm. The multiplicity distribution, i.e., the event average Primary Vertex contributors, is shown in Fig. 3.1. The multiplicity is divided into 10 multiplicity classes (to match the RUN2 analysis [1]). These are N_{ch} = 1-8, 9-14, 15-20, 21-25, 26-33, 34-41, 42-50, 51-60, 61-80, 81-115. To check the efficiency of the detector, i.e., the presence of inactive area in the detector, we have performed $< N_{tracks} >$ vs. z-vertex distribution (Fig. 3.2). It can be clearly seen that the $< N_{tracks} >(z_v)$ is flat around its maximum value, i.e., $< N_{tracks} >$ is independent of Z_{vtx}.

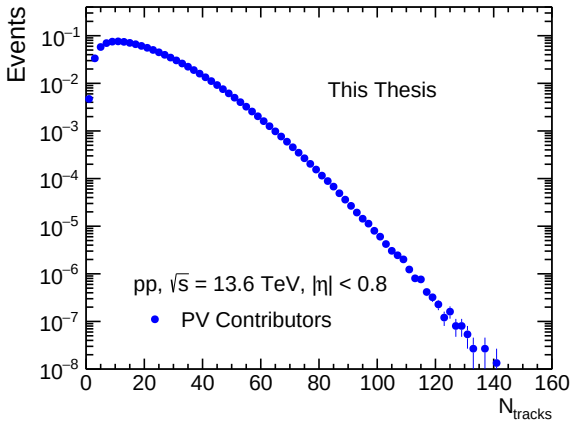

Figure 3.1: N_{tracks} distribution from data [5].

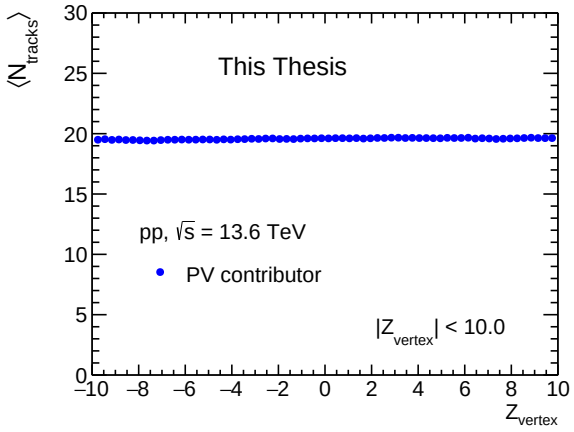

Figure 3.2: $< N_{tracks} >$ vs. Z_{vtx} profile from data [5].

3.4 Monte Carlo Analysis

In order to obtain the true N_{ch} value, we need to correct the efficiency loss. For this, we need to know the correlation of the event-averaged number of corrected tracks in a certain multiplicity range with the number of primary charged particles. The distribution of N_{tracks} from MC simulation (PYTHIA8 + GEANT4) is shown in Fig. 3.3 (left). This correction is obtained from an MC analysis, computing the correlation between N_{ch}^{reco} and the generated N_{ch}^{gen}, which is shown in

Fig. 3.3 (right). For this purpose, we have used general-purpose MC production, which uses PYTHIA8. The MC data periods are listed in Table 3.1:

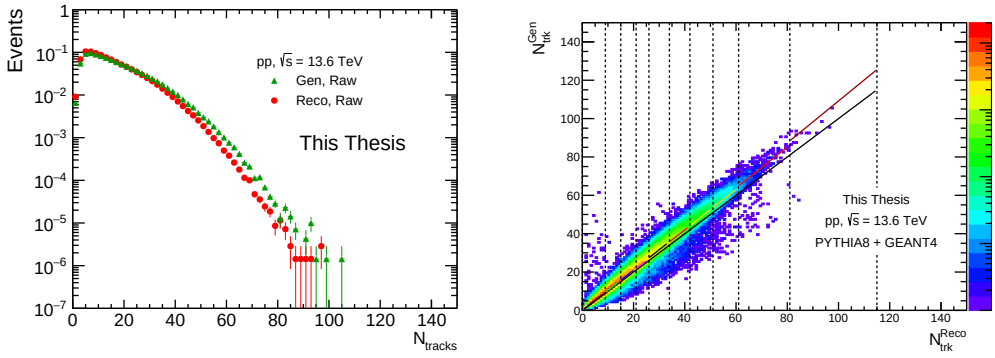

Figure 3.3: N_{tracks} in MC (reconstructed and generated) (left), combining all the periods mentioned in Table 3.1, and right plot is the correlation between N_{trk}^{Gen} and N_{trk}^{Reco} from PYTHIA8. Here, the vertical lines represent the multiplicity bins chosen for the analysis. The fits are used to get the global correction (black line) and the bin-by-bin ones [5].

3.5 Event level correction

When we apply selection cuts to events, we might unintentionally remove some real physical events. To correct for this, we use Monte Carlo (MC) simulations. We calculate how many events pass the selection cut and divide that by the total number of events that were correctly reconstructed. This gives us efficiency. To find how the efficiency depends on the number of tracks (N_{tracks}), we look at the distribution of tracks from reconstructed events before and after applying the cut. We only consider events where the original MC event (that created the reconstructed event) had at least one charged particle in the region $\eta < 0.8$. These are known as INEL > 0 events. To calculate trigger efficiency, we divide the number of events that passed the sel8 cut by the number of events that didn't have this cut applied. All other efficiencies are calculated using events

that already passed the INEL > 0 condition. This way, the efficiencies remain independent of each other, and there's no double-counting.

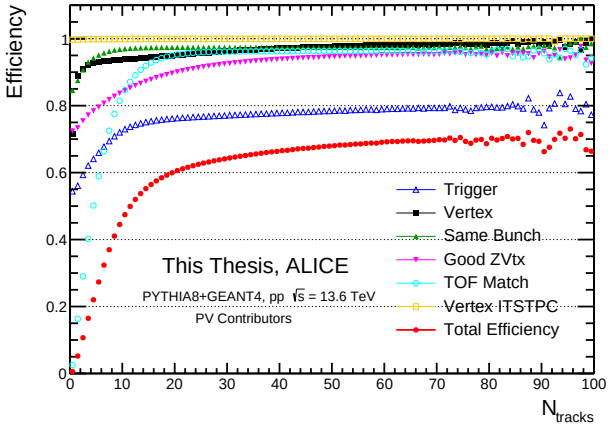

Figure 3.4: N_{tracks} efficiency of PV contributors for different event selection cuts and total efficiency for pp collisions at $\sqrt{s} = 13.6$ TeV. The efficiency was estimated using PYTHIA8.3 and a detector simulation in GEANT4 [5].

The efficiency for a cut "i" is given by:

$$\varepsilon_i(N_{\text{trk}}) = \frac{N_{\text{trk, Cut Applied}}}{N_{\text{trk, Without Cut Applied}}} \tag{3.1}$$

To get the total efficiency, we multiply all the individual efficiencies together:

$$\varepsilon = \prod \varepsilon_i \tag{3.2}$$

This total efficiency is shown in Fig. 3.4

Finally, the inverse of the total efficiency, $w = \frac{1}{\varepsilon}$, is used as a weight when analyzing selected events based on their multiplicity.

After taking care of the efficiency estimation, we have obtained the corrected multiplicity distribution. Fig. 3.5

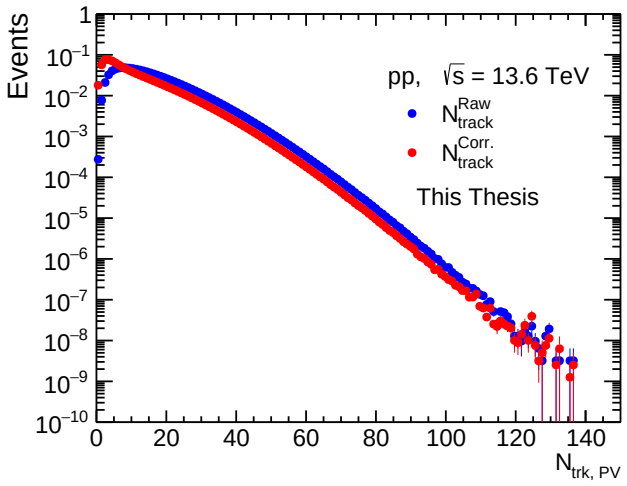

Figure 3.5: N_{tracks} distribution from data after efficiency correction [5].

3.5.1 N_{trk}^{Gen} and N_{trk}^{Reco} correlation factor calculation

The effect of efficiency variation and resolution variation along the z-vertex is already corrected by ALICE central framework; therefore, the $< N_{trk} >$ is flat along the z-vertex (Fig. 3.2). So, the exact N_{ch} value can be obtained by the correlation between reconstructed tracks (N_{trk}^{Reco}) and primary charged particles (N_{trk}^{Gen}). The correction factor for integrated multiplicity will be $\alpha = N_{trk}^{Gen}/N_{trk}^{Reco}$ and this can be obtained by a linear fit between N_{trk}^{Gen} and N_{trk}^{Reco}. The α factor takes care of efficiency loss at z_0 and tracks particle correlation. As each track corresponds to a charged particle, the correlation between N_{trk}^{Gen} and N_{trk}^{Reco} should be linear. From Fig. 3.3 (right), it can be seen that the correlation is not perfectly linear; there is a slight deviation from linearity towards high multiplicity. Therefore, for the current analysis, we have adopted two different methods as follows,

Method 1: By **linear fit** $f(x) = \alpha x$ to N_{trk}^{Gen} and N_{trk}^{Reco} correlation, and then to taking care of non-linearity, we use different polynomials such as, pol1, pol2 and pol3 to fit the N_{trk}^{Gen} and N_{trk}^{Reco} correlation in each multiplicity intervals separately.

Method 2: Using bayesian unfolding method for the correction to N_{trk} distribution.

3.5.2 Method 1:

As we are interested in the multiplicity dependence study of J/Ψ production, the starting point of this analysis is MB N_{trk}^{Reco}. We have divided the MB N_{trk}^{Reco} into different intervals. If the event-averaged corrected number of tracks in i^{th} multiplicity bin is $< N_{trk}^{Reco} >_i$, then the corresponding value of the event-averaged charged particle multiplicity density in that multiplicity bin can be computed as follows:

$$\left\langle \frac{dN_{ch}}{d\eta} \right\rangle_i = \frac{\left\langle N_{trk}^{Reco} \right\rangle_i \times \alpha_i}{\Delta\eta} \tag{3.3}$$

As the tracks are selected in the interval $-0.8 < \eta < 0.8$, therefore $\Delta\eta = 1.6$. The correction factor in each multiplicity interval (α_i) is obtained by fitting N_{trk}^{Gen} - N_{trk}^{Reco} correlation plot by linear function (αx) in each multiplicity bin. In Fig. 3.3 (right), different colors show fitting results in different multiplicity bins. The value of α_i corresponding to each multiplicity interval is tabulated in Table 3.2 and shown in Fig. 3.6. The values of α_i come above unity, which is expected.

To get the relative charged particle density $dN_{\rm ch}/d\eta/\langle dN_{\rm ch}/d\eta\rangle$, the bin $\langle dN_{\rm ch}/d\eta\rangle_i$ has to be divided by event-averaged charged-particle multiplicity. Therefore, the relative multiplicity in i^{th} bin will be:

$$\left(\frac{dN_{\rm ch}/d\eta}{\langle dN_{\rm ch}/d\eta\rangle}\right)_i = \frac{\langle N_{trk}^{Reco}\rangle_i}{\langle N_{trk}^{Reco}\rangle} \tag{3.4}$$

For the ideal case, the generated charged particle varies linearly with a reconstructed charged particle, which implies that the efficiency and track-to-particle effect are independent of multiplicity. But it is not the case. It can be seen from Fig. 3.3 (right) that the red line diverges from the black line towards the higher

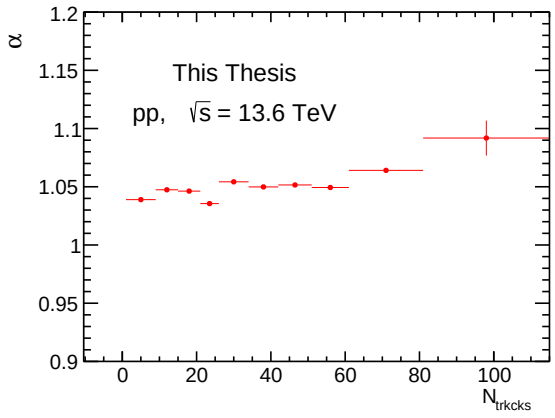

Figure 3.6: $\alpha-$values obtained from linear fit (Method-1) to N_{trk}^{Gen} and N_{trk}^{Reco} correlation [5].

multiplicity. To account for this, we have used higher-order polynomials such as pol1, pol2, and pol3 in addition to alpha-fit, which is shown in Fig. 3.7 to fit the N_{trk}^{Gen} - N_{trk}^{Reco} correlation.

The mean value and systematic uncertainty of the signal are calculated in each multiplicity bin as follows:

Mean: The mean $< N_{ch} >$ is computed by averaging the mean values obtained from fits of four different polynomials: $< N_{ch} >_{\alpha}$, $< N_{ch} >_{pol1}$, $< N_{ch} >_{pol2}$, and $< N_{ch} >_{pol3}$.

$$\mu = \frac{< N_{ch} >_{\alpha} + < N_{ch} >_{pol1} + < N_{ch} >_{pol2} + < N_{ch} >_{pol3}}{4} \tag{3.5}$$

Here, 4 is divided because we consider four different polynomial methods to estimate the systematic uncertainty.

Standard deviation:

$$\sigma = \sqrt{\frac{1}{n}\sum_{i=1}^{n}(X_i - \mu)^2} \tag{3.6}$$

Where:

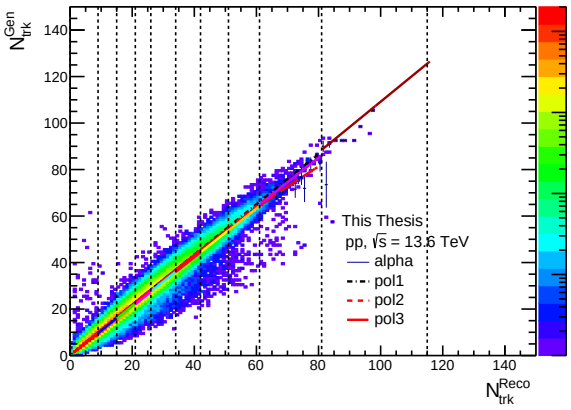

Figure 3.7: Fitting different polynomial (αx, pol1, pol2, pol3 to the N_{trk}^{Gen} and N_{trk}^{Reco} correlation [5].

- X_i represents the individual mean values from different polynomial methods.
- μ is the overall mean of these values.
- n is the total number of methods used (4 in this case).

The mean values and standard deviation are listed in Table 3.3.

3.5.3 Method 2: Evaluation of α using unfolded N_{ch}

From Fig. 3.8, a clear difference in N_{trk} between the Data and MC is observed. The differences are mainly caused by an incorrect description of the underlying N_{ch} distribution of the MC generator. Therefore, to correct for the N_{ch} distribution, the unfolding procedure [2] is applied. The input to the unfolding corrections are a) the original N_{trk} distribution from data and detector response matrix obtained from MC simulations (PYTHIA8).

The measured N_{trk}^{Gen} and N_{trk}^{Reco} distribution was unfolded with the detector response matrix to obtain the unfolded N_{trk}^{Gen} and unfolded N_{trk}^{Reco} distribution as presented in Fig. 3.9. The detector response matrix was rescaled with the ratio

N_{trk}^{Reco} to N_{trk}^{Gen} correction factor (α)			
Multiplicity Class	$\boldsymbol{\alpha}$ - factor	$\langle \boldsymbol{N_{track}^{data}} \rangle$	$\langle \boldsymbol{N_{ch}} \rangle = \boldsymbol{\alpha_i} \times \langle \boldsymbol{N_{track}^{data}} \rangle$
1.0 - 8.0	1.08 ± 0.00	5.96 ± 0.00	6.41 ± 0.00
9.0 - 14.0	1.07 ± 0.00	11.97 ± 0.00	12.78 ± 0.00
15.0 - 20.0	1.06 ± 0.00	17.88 ± 0.00	18.98 ± 0.00
21.0 - 25.0	1.05 ± 0.00	23.39 ± 0.00	24.58 ± 0.00
26.0 - 33.0	1.06 ± 0.00	29.64 ± 0.00	31.46 ± 0.00
34.0 - 41.0	1.06 ± 0.00	37.55 ± 0.00	39.67 ± 0.00
42.0 - 50.0	1.06 ± 0.00	45.85 ± 0.00	48.45 ± 0.00
51.0 - 60.0	1.05 ± 0.00	55.07 ± 0.00	58.06 ± 0.00
61.0 - 80.0	1.06 ± 0.00	67.09 ± 0.01	71.36 ± 0.01
81.0 - 115.0	1.09 ± 0.02	87.45 ± 0.06	95.48 ± 0.07

Table 3.2: N_{tr}^{corr} to N_{ch} correction factor (α) for different multiplicity classes.

of the unfolded N_{trk}^{Gen} and the original N_{trk}^{Gen} distribution. The N_{trk}^{Reco} distributions obtained from MC simulations after rescaling the N_{trk}^{Gen} distribution show better agreement with the data. The unfolding result of both N_{trk}^{Gen} and N_{trk}^{Reco} are shown in Fig. 3.9.

The rescaled detector response matrix is used to obtain the $\alpha-$factor. The average ratio between N_{trk}^{Gen} and N_{trk}^{Reco} termed as $\alpha-$factor. The values of $\alpha-$factor evaluated in multiplicity bins are tabulated in Table 3.4. Further we have estimated the corrected number of charged particles in different multiplicity intervals using this correction factor ($\alpha-$values). The corrected number of charged particles in different multiplicity intervals are given in the Tab. 3.5.

$\langle N_{ch} \rangle$ evaluated using polynomial functions with the systematic uncertainties	
Multiplicity Class	$\langle N_{ch} \rangle$
1.0 - 8.0	6.57 ± 0.09
9.0 - 14.0	13.05 ± 0.16
15.0 - 20.0	19.41 ± 0.25
21.0 - 25.0	25.27 ± 0.40
26.0 - 33.0	32.04 ± 0.33
34.0 - 41.0	40.44 ± 0.45
42.0 - 50.0	49.23 ± 0.48
51.0 - 60.0	58.87 ± 0.63
61.0 - 80.0	71.44 ± 0.97
81.0 - 115.0	92.50 ± 3.24

Table 3.3: $\langle N_{ch} \rangle$ values for different multiplicity classes.

3.6 Signal Extraction

In this work, we extract the inclusive J/ψ signal in the dimuon decay channel using the invariant mass approach. In the ALICE forward muon spectrometer ($-4 < \eta < -2.5$), muons are reconstructed by tracking their trajectories through a system of absorbers, tracking chambers, and a dipole magnet. The bending of tracks in the magnetic field allows determination of their momentum, and hence the transverse momentum (p_T) is obtained from the curvature of the reconstructed muon tracks. We calculate the invariant mass for each of the chosen opposite-sign dimuons, which is obtained by:

$$M_{\mu^+\mu^-} = \sqrt{(E_1 + E_2)^2 - |\vec{p}_1 + \vec{p}_2|^2} \tag{3.7}$$

Here, the energy and momenta of the decay muons are represented by E_1, E_2, and $\vec{p}_1$, $\vec{p}_2$. $M_{\mu^+\mu^-}$ represents the dimuon's invariant mass. This dimuon invariant mass should show a signal peak on the continuum surrounding the mass of J/ψ when plotted as a histogram, which is $m_{J/\psi} = 3096.900 \pm 0.006$ MeV. Around the $\psi(2S)$ mass pole, which is around J/ψ, another signal peak should

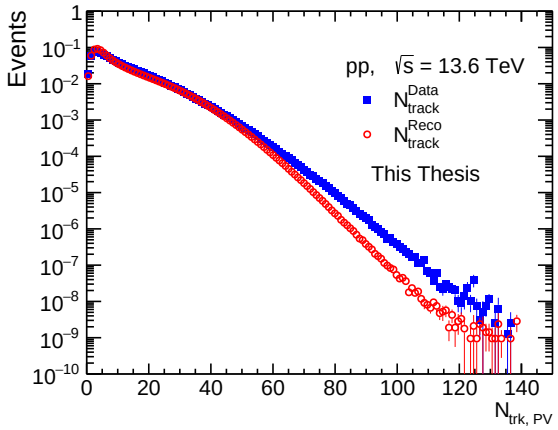

Figure 3.8: N_{tracks} distribution from data and MC (PYTHIA8) [5].

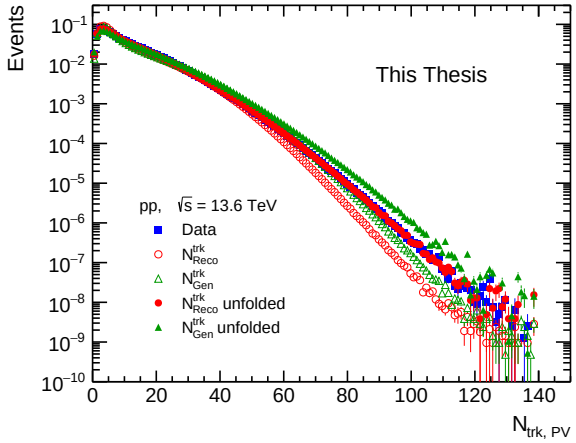

Figure 3.9: N_{tracks} distribution from data and MC and unfolding [5].

also emerge, i.e., $m_{\psi(2S)} = 3686.093 \pm 0.034$ MeV. Compared to $\psi(2S)$, the signal peak for J/ψ is substantially higher. This is because $\psi(2S)$ is the resonance of J/ψ and it has a larger chance than anything else of decaying into a J/ψ, i.e., $\psi(2S) \rightarrow J/\psi + \text{anything}$, B.R. $= (59.5 \pm 0.8)\%$, which subsequently decays to a pair of muons.

The raw yield of J/ψ can then be extracted from the invariant mass distribution. This is accomplished using a sum of the signal and background functions to

N_{trk}^{Reco} to N_{trk}^{Gen} correction factor (α) after unfolding			
Multiplicity Class	$\boldsymbol{\alpha}$ - factor	$\langle \boldsymbol{N_{track,\ corr}^{data}} \rangle$	$\langle \boldsymbol{N_{ch}} \rangle = \boldsymbol{\alpha_i} \times \langle \boldsymbol{N_{track,\ corr}^{data}} \rangle$
1.0 - 8.0	1.09	4.69 ± 0.00	5.10 ± 0.00
9.0 - 14.0	1.09	11.67 ± 0.00	12.75 ± 0.00
15.0 - 20.0	1.09	17.63 ± 0.00	19.23 ± 0.00
21.0 - 25.0	1.09	23.16 ± 0.00	25.17 ± 0.00
26.0 - 33.0	1.08	29.28 ± 0.00	31.71 ± 0.00
34.0 - 41.0	1.08	37.71 ± 0.00	40.09 ± 0.00
42.0 - 50.0	1.07	45.38 ± 0.00	48.77 ± 0.00
51.0 - 60.0	1.07	54.59 ± 0.00	58.34 ± 0.00
61.0 - 80.0	1.06	66.26 ± 0.01	70.27 ± 0.01
81.0 - 115.0	1.05	86.50 ± 0.04	90.10 ± 0.03
1.0 - 115.0 (Integrated)	1.04	11.86 ± 0.01	12.64 ± 0.01

Table 3.4: N_{tr}^{corr} to N_{ch} correction factor (α) for different multiplicity classes.

fit the invariant mass spectrum. These functions, which have several components for characterizing the signal and the long continuum on either side of the signal peak, which we refer to as the tail, were selected empirically. The double Crystal Ball function (CB2) is applied to the signal; it is composed of a Gaussian core with power-law tails appended on either side of the peak's mean. Two distinct CB2 functions, one for J/ψ and one for $\Psi(2S)$, are employed in the fitting since the $\Psi(2S)$ mass peak is near J/ψ. This also addresses the possibility that the low mass tail of $\psi(2S)$ could influence the high mass tail of J/ψ. The fact that both particles are suited to the same kind of signal function is crucial to this fitting. As it happens, there is a close relationship between the parameters of the signal functions for these two particles. The mass ($m_{\psi(2S)}^{\text{fit}}$) and width ($\sigma_{\psi(2S)}^{\text{fit}}$) of the $\psi(2S)$ signal relate to the mass ($m_{J/\psi}^{\text{fit}}$) and width ($\sigma_{J/\psi}^{\text{fit}}$) of the J/ψ signal derived from the fitting as follows.

Bin	N_{PV} Interval	$N^{I}_{\mathrm{ch}}/\langle N_{\mathrm{ch}}\rangle$
1	1–8	0.40 ± 0.00
2	9–14	1.01 ± 0.00
3	15–20	1.52 ± 0.00
4	21–25	1.99 ± 0.00
5	26–33	2.51 ± 0.00
6	34–41	3.18 ± 0.00
7	42–50	3.86 ± 0.00
8	51–60	4.62 ± 0.00
9	61–80	5.57 ± 0.00
10	81–115	7.13 ± 0.00
1-115 (Integrated)		12.64 ± 0.00

Table 3.5: Multiplicity bins and relative charged particle densities with uncertainties (rounded to two decimal places).

$$m_{\psi(2S)} = m^{\mathrm{fit}}_{J/\psi} + \Delta m^{\mathrm{PDG}}, \tag{3.8}$$

$$\Delta m^{\mathrm{PDG}} = m^{\mathrm{PDG}}_{\psi(2S)} - m^{\mathrm{PDG}}_{J/\psi} \tag{3.9}$$

$$\sigma_{\psi(2S)} = \sigma^{\mathrm{fit}}_{J/\psi} \times \frac{\sigma^{\mathrm{MC}}_{\psi(2S)}}{\sigma^{\mathrm{MC}}_{J/\psi}} \tag{3.10}$$

The PDG provides [3] the mass difference between the two particles, and a CB2 function fitting to the Monte Carlo (MC) data yields the ratio of their widths, which is $\sigma_{\psi(2S)}/\sigma_{J/\psi} \sim 1.03$, in accordance with a prior analysis based on the same data sample [1]. The background description is done using two different *ad hoc* functions. These are the Double Exponential (DoubleExp) and Variable Width Gaussian (VWG) functions. The objective is to use the fewest possible

Bin	Mult-Bin	$N_{J/\psi}$
1	1–8	458973 ± 1249
2	9–14	772690 ± 1707
3	15–20	822120 ± 1872
4	21–25	594210 ± 1665
5	26–33	684201 ± 2101
6	34–41	387644 ± 1449
7	42–50	203775 ± 1065
8	51–60	84464 ± 887
9	61–80	31456 ± 439
10	81–115	2056 ± 120
1-115 (Integrated)		4039867 ± 4271

Table 3.6: Number of J/ψ values in different multiplcvity intervals.

free parameters to fit the background. Appendix 3.8 contains explicit references to the signal and background functions.

First, the signal has been extracted for integrated multiplicity and integrated p_T. The J/ψ signal is reconstructed in the $\mu^+\mu^-$ decay channel. With suitable selection cuts, a resonance structure around the rest mass of the J/ψ appears, which lies on top of a background (Fig. 3.10). The intrinsic decay width of a J/ψ is $\Gamma \sim 92.9$ keV/c^2, while in the experiment one observes a much broader structure. Especially toward lower masses, the J/ψ peak exhibits a long tail. After that, we corrected the signal by taking care of the efficiency estimated from different event selection cuts using MC data. Then, the signal is divided into 11 multiplicity bins, and in each multiplicity bin, the signal is extracted using the same procedure. Here, we have fitted only the Double Crystal ball function (CB2) with signal and the Variable Width Gaussian function(VWG) with background.

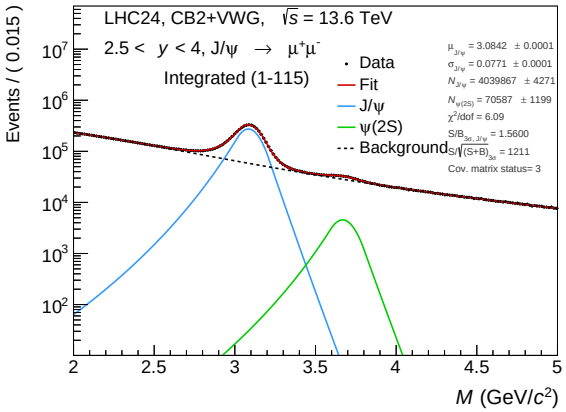

Figure 3.10: Fitting of a CB2+CB2+VWG function in the integrated multiplicity bin (1-115) range in pp collisions at $\sqrt{s} = 13.6$ TeV [5].

The tail parameters are kept free. The fitting ranges are kept for the fitting of the signal+background functions in the range $2.0 < M_{\mu^+\mu^-} < 5.0$ GeV/c^2. The fitting of all multiplicity bins is shown in Fig. 3.11. After that, we estimate the J/ψ number in each multiplicity interval and estimate the relative J/ψ with respect to the relative charged particle. Fig. 3.12 shows the self-normalised relative J/ψ yield as a function of self-normalized multiplicity in $|\eta| < 0.8$ in pp collisions at $\sqrt{s} = 13.6$ TeV. The multiplicity was estimated from Primary Vertex (PV) contributors. The result of the p_T-integrated analysis of the self-normalized J/ψ yield in the forward region ($2.5 < y < 4.0$) as a function of the self-normalized multiplicity is shown in Fig. 3.12. The obtained results are compared with the results from the previous analysis in RUN2. The values for the self-normalized yield versus multiplicity, estimated from SPD tracklets at $\sqrt{s} = 13$ TeV, are taken from this Ref. [4]. The comparison shows a good agreement with the Run 2 result [4]. However, there are still some deviations from the RUN2 result towards the high multiplicity region. There are several issues with not obtaining the corrected number of J/ψ in the RUN3 data for the current period. More advanced algorithms for event separation and pile-up rejection are being developed for cleaner selection of primary collisions, especially high multiplicity region.

3.6 Signal Extraction

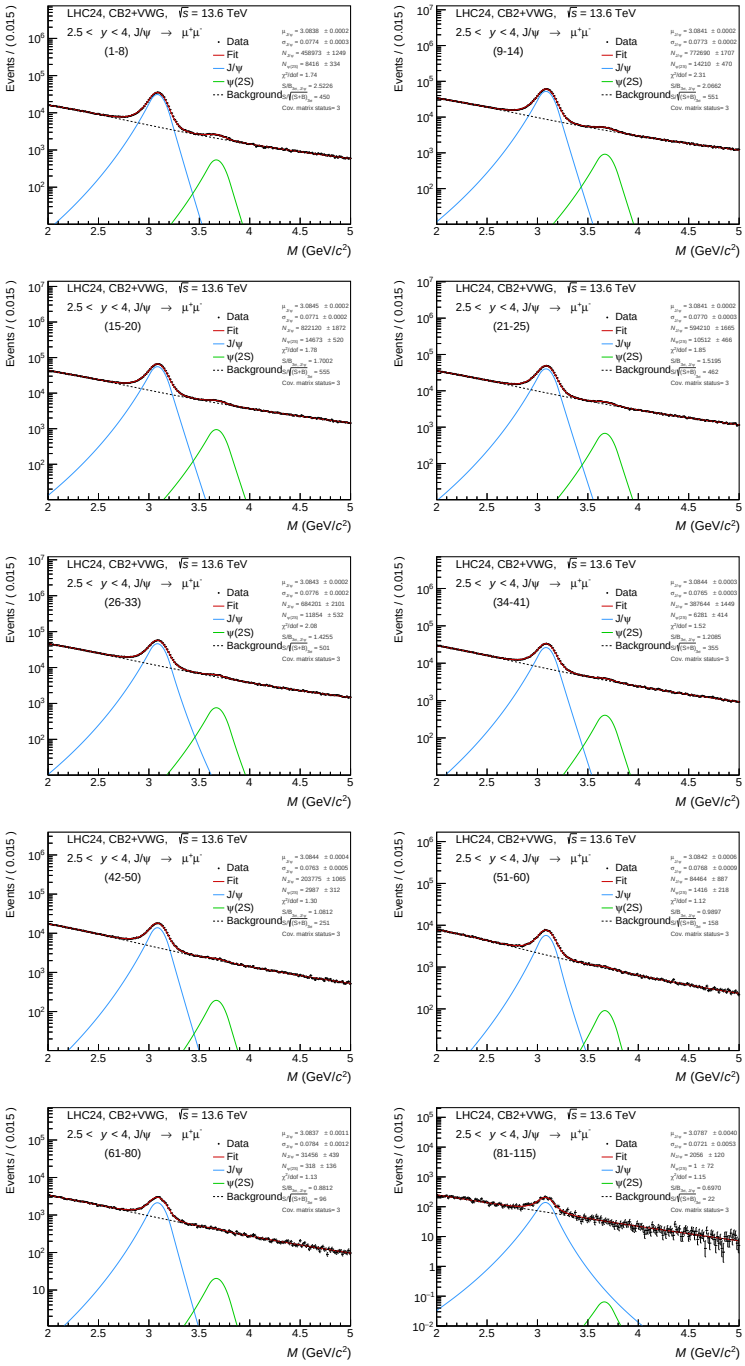

Figure 3.11: Example of signal extractions in different multiplicity bins using CB2+VWG function in the range $2.0 < M_{\mu^+/mu^-} < 5.0$ [5].

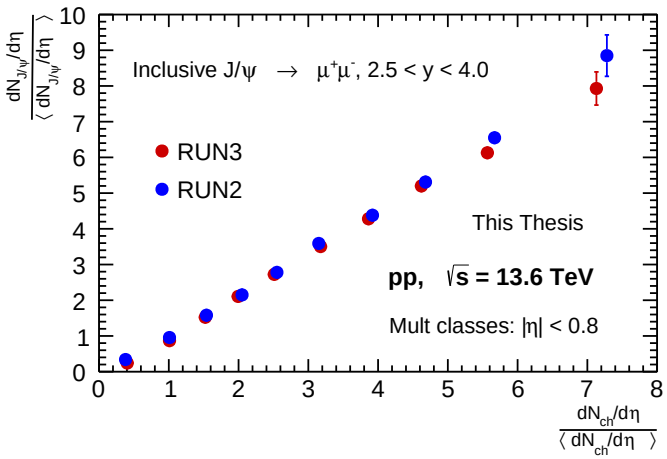

Figure 3.12: Self-normalize p_T-integrated J/ψ yield in forward rapidity region ($2.5 < y < 4.0$) as a function of self-normalized charged-particle yield in $|\eta| < 0.8$ in pp collisions at $\sqrt{s} = 13.6$ TeV. The multiplicity was estimated from PV contributors [5].

Ongoing efforts are being made to improve detector reconstruction, calibration, and alignment in order to decrease systematic biases in J/ψ yield extraction and multiplicity and to increase tracking efficiency.

Furthermore, we have estimated the self-normalized relative $\psi(2S)$ yield as a function of the self-normalized charged-particle multiplicity within $|\eta| < 0.8$. Subsequently, we evaluated the ratio of the normalized $\psi(2S)$-over-J/ψ yields as a function of the normalized charged-particle multiplicity, as shown in Fig. 3.13. The normalized $\psi(2S)$-over-J/ψ yield ratio shows no significant deviation from unity across the charged-particle multiplicity range, suggesting that the excited and ground state charmonium states follow a similar multiplicity trend. The obtained results are consistent with the Run 2 measurements [6].

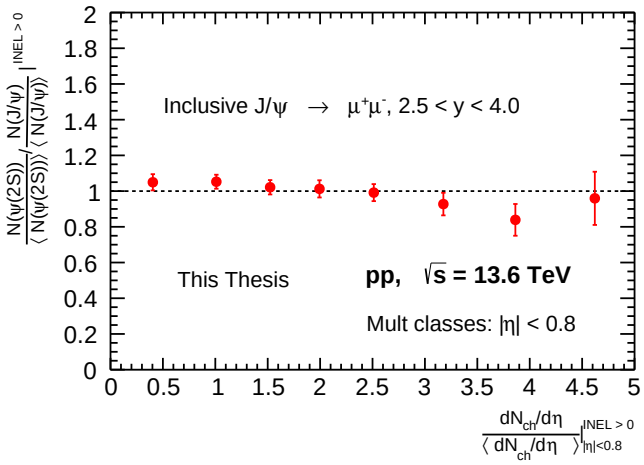

Figure 3.13: Ratio of normalized $\psi(2s)/J/\psi$ yield as a function of the normalized charged-particle in pp collisions at $\sqrt{s} = 13.6$ TeV [5].

3.7 Summary

We have presented a detailed analysis of the self-normalized inclusive J/ψ yield at forward rapidity ($2.5 < y < 4.0$) as a function of the self-normalized charged-particle multiplicity in $|\eta| < 0.8$ for the pp collisions at a center-of-mass energy $\sqrt{s} = 13.6$ TeV. Multiplicities were estimated using PV contributors. To convert from the raw number of tracks in a collision to the true charged-particle multiplicity, an iterative Bayesian unfolding algorithm was employed. The self-normalized inclusive J/ψ yield shows a linearly increasing trend as a function of charged particle multiplicity. Furthermore, we have evaluated the ratio of the normalized $\psi(2S)$-over-J/ψ yields as a function of the normalized charged-particle multiplicity. The normalized $\psi(2S)$-over-J/ψ ratio is compatible with unity independently of the charged-particle multiplicity within uncertainties.

3.8 Appendix

3.8.1 List of good run numbers

LHC24 pass1 skimmed

1. **LHC24af:** 550916, 550889, 550858, 550852, 550848, 550843, 550824, 550819, 550784, 550781, 550778, 550774, 550760, 550756, 550742, 550731, 550728, 550711, 550707, 550691, 550690, 550654, 550634, 550632, 550630, 550439, 550425, 550424, 550421, 550417, 550412, 550375, 550369, 550367

2. **LHC24ag:** 551504, 551498, 551468, 551463, 551427, 551418, 551398, 551394, 551392, 551391, 551389, 551387, 551365, 551296, 551290, 551272, 551260, 551257, 551255, 551232, 551230, 551229, 551221, 551219, 551149, 551127, 551122, 551107, 551105, 551083, 551066, 551027, 551023, 551013, 551008, 551007, 551005, 550997

3. **LHC24aj:** 552403, 552402, 552401, 552400, 552384, 552383, 552382, 552381, 552369, 552353, 552341, 552340, 552304, 552285, 552283, 552206, 552205, 552204, 552203, 552201, 552200, 552198, 552197, 552179, 552178, 552177, 552176, 552156, 552142, 552141, 552140, 552139, 552138, 552103, 552102, 552080, 552029, 552005, 551997, 551993, 551992, 551989, 551983, 551982, 551979, 551977, 551958, 551943, 551931, 551926, 551925, 551924, 551923, 551922, 551921, 551894, 551890, 551889, 551877, 551875, 551874, 551856, 551843, 551780, 551761, 551760, 551759

4. **LHC24am:** 555976, 555967, 555965, 555960, 555958, 555933, 555917, 555900, 555883, 555860, 555853, 555850, 555801, 555798, 555790, 555789, 555763, 555761, 555759, 555742, 555740, 555723, 555707, 555705, 555695, 555693, 555676, 555651, 555649, 555612, 555596, 555591, 555575, 555546,

555543, 555540, 555504, 555482, 555478, 555476, 555451, 555443, 555435, 555411, 555408, 555401, 555374, 555370, 555345, 555344

5. **LHC24al:** 555308, 555270, 555267, 555259, 555254, 555232, 555226, 555208, 555202, 555187, 555172, 555166, 555160, 555156, 555152, 555150, 555124, 555122, 555121, 555073, 555071, 555047, 555023, 555022, 555020, 554998, 554973, 554970, 554968, 554920, 554898, 554880, 554873, 554837, 554835, 554808, 554791, 554774, 554772, 554768, 554752, 554736, 554732, 554728, 554714, 554703, 554633, 554615, 554613, 554603, 554588, 554569, 554564, 554558, 554538, 554526, 554524, 554507, 554504, 554495, 554494, 554471, 554462, 554427, 554413, 554408, 554404, 554394, 554354, 554323, 554322, 554316, 554295, 554293, 554261, 554247, 554223, 554208, 554207, 554203, 554201, 554198, 554194, 554098, 554095, 554094, 554092, 553903, 553880, 553862, 553844, 553825, 553824, 553821, 553819, 553816, 553807, 553785, 553756, 553739, 553702, 553700, 553663, 553660, 553655, 553633, 553610, 553590, 553588, 553555, 553536, 553530, 553512, 553486, 553305, 553299, 553297, 553294, 553274, 553255, 553253, 553250, 553225, 553219, 553193, 553189, 553188, 553187, 553185

3.8.2 Lists of bad runs

550653, 555431, 555722, 555881, 554097, 554701

3.8.3 Signal and Background fitting functions

3.8.3.1 Signal Fittng:

Double Crystal Ball function (CB2)

$$f(x; N, \bar{x}, \sigma, t_1, t_2, p_1, p_2) = N \cdot \begin{cases} A \cdot (B - t)^{-p_1}, & t \leq t_1 \\ \exp\left(-\frac{1}{2}t^2\right), & t_1 < t < t_2 \\ C \cdot (D + t)^{-p_2}, & t \geq t_2 \end{cases} \tag{3.11}$$

where

$$t = \frac{x - \bar{x}}{\sigma}$$

$$A = \left(\frac{p_1}{|t_1|}\right)^{p_1} \cdot \exp\left(-\frac{|t_1|^2}{2}\right)$$

$$B = \frac{p_1}{|t_1|} - |t_1|$$

$$C = \left(\frac{p_2}{|t_2|}\right)^{p_2} \cdot \exp\left(-\frac{|t_2|^2}{2}\right)$$

$$D = \frac{p_2}{|t_2|} - |t_2|$$

3.8.3.2 Background fitting:

Variable Width Gaussian (VWG)

$$f(x; N, \bar{x}, A, B) = N \cdot \exp\left(-\frac{(x - \bar{x})^2}{2\sigma_{VWG}^2}\right) \tag{3.12}$$

where

$$\sigma_{VWG} = A + B \cdot \frac{x - \bar{x}}{\bar{x}}$$

and the combination of a fourth-degree polynomial and an exponential function (POL4EXP) is:

$$f(x; N, p_0, p_1, p_2, p_3, p_4, p_5) = N \cdot \exp(p_0 x) \cdot (p_1 + p_2 x + p_3 x^2 + p_4 x^3 + p_5 x^4) \tag{3.13}$$

Bibliography

[1] J/ψ production as function of charged-particle multiplicity in pp collisions at $\sqrt{s} = 13$ TeV at forward rapidity, D. Thakur and R. Sahoo, [https://alice-notes.web.cern.ch/node/734] [ALICE Internal].

[2] ROOT Unfolding Framework, https://gitlab.cern.ch/RooUnfold/RooUnfold

[3] R. L. Workman *et al.* (Particle Data Group), Prog. Theor. Exp. Phys. **2022**, 083C01 (2022).

[4] S. Acharya *et al.* [ALICE], JHEP **06**, 015 (2022).

[5] $\psi(2S)/J/\psi$ production ratio as a function of charged-particle multiplicity in pp collisions at $\sqrt{s} = 13.6$ TeV with ALICE, D. Behera, D. Thakur and R. Sahoo, [https://alice-notes.web.cern.ch/node/1662] [ALICE Internal].

[6] S. Acharya *et al.* [ALICE], JHEP **06**, 147 (2023).

Chapter 4

Collective Dynamics in Small Systems: O–O Collisions at LHC Energies

4.1 Motivation

Ultra-relativistic hadronic and nuclear collisions at the Large Hadron Collider (LHC) have advanced our understanding of high-energy physics significantly. Heavy-ion collisions at the LHC have made it easier to study quark-gluon plasma, a hot and dense QCD matter. To better understand the properties of Quark-Gluon Plasma (QGP), several collider experiments conduct measurements in different collision systems at different center-of-mass energies. Traditionally, quark-gluon plasma (QGP) studies at collider experiments such as the LHC and RHIC have focused on heavy-ion collisions like Pb–Pb and Au–Au, while smaller systems like proton–proton (pp) collisions have primarily served as reference baselines. However, recent LHC experiment results reveal QGP-like characteristics in high-multiplicity pp collisions [1–4], which makes heavy-ion physicists question whether pp collisions can serve as a baseline and whether QGP droplets are created in small system collisions at LHC energies. This ambiguity has serious implications for the results of heavy-ion collisions. Thus, a closer look at the small collision systems is a call for time. A brief run of Oxygen-oxygen (O-O)

collisions is presently ongoing in RUN3 at the LHC [5]. This short run might offer a useful chance to research the impacts observed in high-multiplicity p-Pb collisions, in which a system has the same number of final state multiplicity but a relatively bigger geometrical transverse overlap region [6] and a similarly small number of participating nucleons. A larger overlap area, combined with a comparable final-state multiplicity, is expected to enhance path-length-dependent phenomena such as jet quenching. A number of theoretical studies have recently examined different facets of particle production dynamics associated with O-O collisions, including those in references [7–15]. Furthermore, O-O collisions offer a great chance to investigate the fundamental processes that underlie the production of particles, light-nuclei, and transverse collective flow effects in a multiplicity range that spans Pb-Pb and Xe-Xe on the higher side and pp and p-Pb on the lower side [6].

Besides these, the ^{16}O has a rather compact structure and is resistant to decay because of its double magic property [16]. The $\alpha-$clustered structure [17–20] is also thought to have an effect on the oxygen nuclei. $\alpha-$clustering in a nucleus refers to the phenomenon where two protons and two neutrons group together to form a cluster. Recent simulation investigations for collisions involving oxygen nuclei reveal a signature of $\alpha-$ clustering [20]. However, the exotic tetrahedral $\alpha-$clustering structure of ^{16}O nucleus, first hypothesized by G. Gamow [21] and later by J.A. Wheeler [22], has not yet been substantiated by good experimental data. In particular, Broniowski *et al.* [23–25] is proposing and studying in great detail the probing of the $\alpha-$clustering structure in relativistic collisions of light nuclei. Thus, it is also crucial to look at whether the initial nuclear structure has an impact on the final-state observables, including the collective behavior of produced particles or the net particle production yield. Hence, a comprehensive understanding of these observables and QGP-like features is vital for the study of systems produced in O–O collisions.

4.1 Motivation

A fundamental nuclear shell model calculation [26] incorporates a spin-orbit interaction term after assuming the nuclear potential to be that of a simple harmonic oscillator. The nucleus that contains these nucleon magic numbers is expected to be highly stable and tightly bound. Oxygen's nucleus is doubly magic and should be extremely compact because its proton and neutron counts meet the magic number separately.

We have used a multi-phase transport model (AMPT) [27] to add a more realistic Woods-Saxon potential and a simple harmonic oscillator potential in the oxygen nucleus in order to gain a better understanding of the influence of nuclear structure inside the nucleus. We also compared the results with a α-clustered structure within the oxygen nucleus. Global observables such as charged-particle multiplicities, transverse energy, particle spectra, and pseudorapidity distributions provide information about the potential formation of QGP in a system. It is suggested that the correlation between mean transverse momentum and particle multiplicity [28] can be used to investigate the equation of state of hot hadronic matter. While the mean transverse mass and momentum provide information about the hard processes in the collision, charged-particle multiplicity provides information about the soft processes. Recent LHC data [1] indicate that the final state multiplicity drives the QGP-like features observed in high-multiplicity pp collisions. So, it is interesting to study the initial and final state effects in O–O collisions, since their multiplicity is similar to that in high-multiplicity pp collisions. The Bjorken hydrodynamic model [29] can be used to estimate the initial energy density, where one uses the transverse energy or charged-particle multiplicity density in rapidity and mean transverse mass for each collision centrality. To investigate the final state effects, particle spectra, kinetic freeze-out parameters, and particle ratios can be examined.

The structure of this chapter is as follows. Section 4.1 outlines the motivation

behind this study. In Section 4.2, we describe the event generation process using the AMPT model. Section 4.3 discusses various nuclear density profiles, while Section 4.4 presents the results related to global properties. The anisotropic flow results are presented in Section 4.5, and the nuclear modification factor results are discussed in Section 4.6. Finally, the chapter concludes with a summary in Section 4.7.

4.2 Event generation

4.2.1 A Multi-Phase Transport (AMPT) Model

The AMPT (A multi-phase transport) model is an event generator in heavy-ion physics that simulates heavy-ion collisions. It helps study QGP properties and final-state particle observables. It consists of four main stages: the initialization of the collisions, the parton cascade, the hadronization, and the hadronic interactions. These key components are discussed below:

1. **Initialization:** The initial collisions of AMPT are obtained from the HIJING (Heavy Ion Jet Interaction Generator) model, which describes the early stages dynamics of the collisions [30]. The early stage includes the distributions of momentum and space of generated hadrons and partons before evolution. An incorporated Glauber model is used to compute and convert the cross-section of the minijets created in pp collisions to heavy-ion collisions.

2. **Parton cascade:** After the initial conditions are set by HIJING, the AMPT model handles partonic interactions before hadronization. Here, the produced parton evolves through Zhang's Parton Cascade (ZPC) model, which includes partonic interactions via two-body elastic parton scatterings [31]. These scatterings are modeled using the leading-order pQCD

cross-section, given by:

$$\sigma = \frac{9\pi\alpha_s^2}{2\mu^2} \tag{4.1}$$

Where α_s is the strong coupling constant, and μ is the Debye screening mass that regulates the interaction range in the medium.

3. **Hadronization:** After the parton transport, the next process is the hadronization, where partons (quarks and gluons) combine to form hadrons. There are two different models for hadronization inside the AMPT model [32–34].

   (a) **Default AMPT (Lund string fragmentation):** In the default AMPT model, hadrons are directly generated by HIJING and do not undergo partonic interactions. These hadrons are then hadronized using the Lund String Fragmentation model.

   (b) **String melting AMPT (Quark coalescence):** In the String Melting version of AMPT, hadrons from HIJING are first converted into partons, which interact via Zhang's Parton Cascade (ZPC). After partonic interactions, hadronization occurs through quark coalescence (recombination) instead of string fragmentation. When partons (quarks and antiquarks) come close together in phase space, they recombine into hadrons. The probability of coalescence is determined by the overlap between parton and hadron wavefunctions.

4. **Hadronic Interactions:** After hadronization, the system enters the hadronic interaction phase, where hadrons interact before kinetic freeze-out. These interactions are handled using the ART (A Relativistic Transport) model in AMPT [35, 36]. This ART model includes meson-meson, meson-baryon, and baryon-baryon-level interactions.

The transverse momentum spectra and rapidity distribution of the identified particles in heavy-ion collisions at both SPS and RHIC are well described by

the default model. However, the elliptic flow at RHIC is greatly underestimated. Since only the mini-jet partons from HIJING are included in the parton cascade in the default model, the initial parton density is comparatively lower in order to generate the required medium effects. However, in the string melting model, before the parton cascade phase, all of the excited strings are also transformed into partons and mixed with the minijet partons. This increases the parton density required to sustain the medium effects, resulting in a good description of the elliptic flow and particle p_T spectra in the intermediate p_T. We note that in the HIJING model, minijet partons produced from hard scatterings can lose energy through gluon splitting and transfer this energy to nearby soft strings. In the AMPT model, this so-called jet quenching mechanism in HIJING is replaced by parton scatterings in the Zhang's Parton Cascade (ZPC). Since only two-body elastic scatterings are included in ZPC, higher-order processes contributing to jet energy loss, such as medium-induced gluon radiation, are not incorporated. Consequently, the jet quenching effect in AMPT is limited to collisional energy loss and does not include the full radiative contributions expected in perturbative QCD-based jet quenching models. In the current work, we have used the string melting mode of AMPT (AMPT version 2.26t9b), and the AMPT setting is reported in Ref. [17, 37].

4.3 Nuclear density profiles

The nuclear density profile plays a crucial role in governing the final-state observables in heavy-ion collisions. In this work, we have employed three density profiles (Woods-Saxon, Harmonic oscillator, and α-cluster) inside the oxygen nucleus to see the effect of density profile on particle production:

4.3.0.1 Woods-Saxon Profile

The Woods-Saxon profile is a commonly used nuclear density distribution that characterizes the nuclear shape using a three-parameter Fermi (3pF) distribution. It is defined as:

$$\rho(r) = \frac{\rho_0(1 + w(\frac{r}{r_0})^2)}{1 + \exp(\frac{r-r_0}{a})}. \tag{4.2}$$

Where r_0 is described as an equilibrium or saturation radius up to which nuclear matter is evenly distributed, and corresponding density distribution is defined by ρ_0 (a constant nuclear density at the core of a nucleus), r is the radial distance from the center of the nucleus, w is the deformation parameter, and a is the skin diffusivity/depth of the nucleus. For oxygen nucleus, a is 0.513 fm, r_0 is 2.608 fm and w is -0.051 [17].

4.3.0.2 Harmonic oscillator Profile

The harmonic oscillator model provides an alternative nuclear charge density description and is given by:

$$\rho(r) = \rho_0\left[1 + \alpha\left(\frac{r}{a}\right)^2\right]\exp\left(\frac{-r^2}{a^2}\right). \tag{4.3}$$

Here, α and a are parameters that are taken as 1.833 and 1.544 fm for oxygen, respectively [17]. ρ_0 is a constant nuclear density at the core of a nucleus.

4.3.0.3 α-clustered structure in O^{16}

Clustering plays an essential role in the study of nuclear structure. In order to reduce overall energy or boost system stability, protons and neutrons in many-body nuclear systems tend to form clusters. Two protons and two neutrons together form an α-particle. In several light nuclei ^{8}Be and ^{12}C [17] α-cluster structure had been observed. The experimental observation is predicated on the ^{16}O having

an α-like cluster at the corners of a tetrahedron (Fig. 4.1). The distribution of nucleons within an α-cluster follows the Woods-Saxon distribution for ^{4}He nuclei with a radius of 1.676 fm. Such randomized α-clusters are placed on the vertices of a regular tetrahedron with a side length of 3.42 fm. The rms radius of such an arrangement gives the rms radius for ^{16}O to be 2.699 fm. The arrangement of nucleons is randomized event-by-event by rotating the system in the x-y-z directions for both projectile and target nuclei, following the tetrahedral structure.

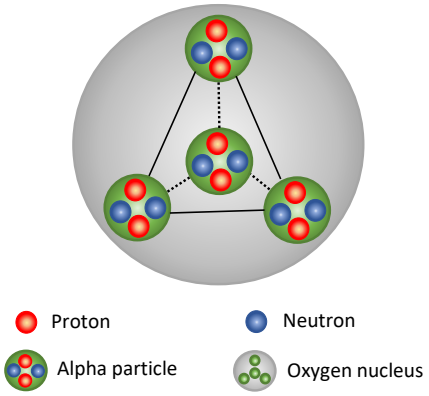

Figure 4.1: Model representation of the oxygen nucleus with an α-clustered configuration [17].

For Woods-Saxon, harmonic oscillator, and α-cluster density profiles, the probability of the radial positions of the nucleons distributed inside the oxygen nucleus is shown in Fig. 4.2. In contrast to the other two density profiles, the α-cluster structure appears to have a compact radial distribution of nucleons.

Galuber model helps to estimate quantities such as the number of participants ($N_{part}(b)$), number of binary nucleon-nucleon collisions ($N_{coll}(b)$), impact parameter (b), etc. in heavy-ion collisions which depends on the nuclear overlap function ($T_{AA}(b)$). This overlap function is determined based on a realistic model

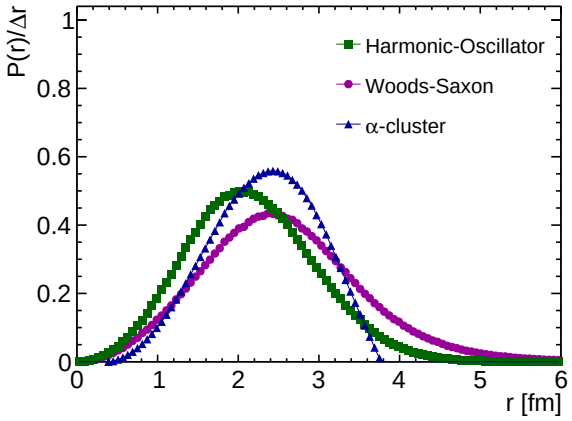

Figure 4.2: Radial probability distribution of nucleons within the oxygen nucleus. Circular (rectangular) markers correspond to the Woods-Saxon (harmonic oscillator) density profile, while triangular markers represent the α-clustered configuration [17].

of the collision geometry, which assumes the proton to be a point-like particle, leading to $N_{\rm coll}(b) = 1$. In this work, we have modified the Glauber model in AMPT to include a harmonic oscillator density profile and α-clustered structure in the oxygen nucleus. The values of the number of participants ($N_{part}(b)$), impact parameters (b), nucleon-nucleon collisions ($N_{coll}(b)$) for different centrality classes in O-O collisions for different density profiles are obtained using the publicly available MC Glauber code (TGlauberMC-3.2), and these values are shown in Table 4.1.

4.4 Global observables

4.4.1 Transverse energy and Bjorken Energy Density

One of the most important observable in the study of QGP properties in heavy-ion collisions is the initial energy density. It can be estimated via the Bjorken boost-invariant hydrodynamics model [17]. The Bjorken energy density ($\epsilon_{\rm Bj}$) with

Table 4.1: Centrality bins and corresponding impact parameters, participant number, and number of binary collisions for different models: Woods-Saxon, Harmonic Oscillator, and α-Cluster.

Woods-Saxon

Centrality(%)	b_{min} (fm)	b_{max} (fm)	$\langle N_{\text{part}} \rangle \pm$ rms	$\langle N_{\text{coll}} \rangle \pm$ rms
0–5	0.00	1.47	28.00 ± 2.06	48.33 ± 9.43
5–10	1.47	2.08	25.22 ± 2.27	39.96 ± 7.98
10–20	2.08	2.94	21.25 ± 2.81	30.17 ± 7.34
20–30	2.94	3.59	16.46 ± 3.01	20.24 ± 5.96
30–40	3.59	4.14	12.55 ± 3.20	13.63 ± 5.07
40–50	4.14	4.63	9.39 ± 3.15	9.13 ± 4.22
50–60	4.63	5.09	7.01 ± 2.86	6.17 ± 3.40
60–70	5.09	5.54	5.32 ± 2.45	4.27 ± 2.65
70–100	5.54	13.46	3.33 ± 1.68	2.28 ± 1.68

Harmonic Oscillator

Centrality(%)	b_{min} (fm)	b_{max} (fm)	$\langle N_{\text{part}} \rangle \pm$ rms	$\langle N_{\text{coll}} \rangle \pm$ rms
0–5	0.00	1.28	29.48 ± 1.61	63.83 ± 11.32
5–10	1.28	1.83	27.06 ± 2.00	52.64 ± 9.17
10–20	1.83	2.58	23.20 ± 2.68	39.31 ± 8.57
20–30	2.58	3.17	18.30 ± 2.94	26.21 ± 6.95
30–40	3.17	3.66	14.12 ± 3.17	17.55 ± 6.00
40–50	3.66	4.10	10.46 ± 3.21	11.33 ± 4.98
50–60	4.10	4.51	7.76 ± 2.99	7.43 ± 3.98
60–70	4.51	4.89	5.76 ± 2.57	4.96 ± 3.07
70–100	4.89	9.86	3.47 ± 1.76	2.47 ± 1.86

α-Cluster

Centrality(%)	b_{min} (fm)	b_{max} (fm)	$\langle N_{\text{part}} \rangle \pm$ rms	$\langle N_{\text{coll}} \rangle \pm$ rms
0–5	0.00	1.30	29.43 ± 2.02	55.12 ± 8.90
5–10	1.30	1.86	26.50 ± 2.24	46.56 ± 7.53
10–20	1.86	2.63	22.25 ± 2.57	36.19 ± 7.09
20–30	2.63	3.22	17.51 ± 2.49	25.85 ± 5.74
30–40	3.22	3.72	13.71 ± 2.42	18.31 ± 5.17
40–50	3.72	4.15	10.58 ± 2.43	12.80 ± 4.69
50–60	4.15	4.56	8.05 ± 2.46	8.74 ± 4.21
60–70	4.56	4.94	6.11 ± 2.30	5.98 ± 3.51
70–100	4.94	8.79	3.74 ± 1.81	2.97 ± 2.35

Table 4.2: Centrality dependent average charged-particle multiplicity density for different nuclear profiles in O-O collisions at $\sqrt{s_{\mathrm{NN}}} = 7$ TeV in the range $|\eta| < 0.5$

Centrality	Woods-Saxon	harmonic oscillator	$\alpha-$cluster
	$\langle dN_{ch}/d\eta \rangle$	$\langle dN_{ch}/d\eta \rangle$	$\langle dN_{ch}/d\eta \rangle$
0–5	161.07 ± 0.15	192.60 ± 0.20	187.54 ± 0.14
5–10	139.38 ± 0.13	167.37 ± 0.18	163.86 ± 0.11
10–20	112.20 ± 0.13	134.72 ± 0.18	132.67 ± 0.10
20–30	82.84 ± 0.11	99.34 ± 0.12	100.21 ± 0.09
30–40	61.33 ± 0.10	73.40 ± 0.11	74.60 ± 0.08
40–50	45.10 ± 0.09	53.23 ± 0.09	54.72 ± 0.07
50–60	32.81 ± 0.07	38.31 ± 0.08	39.56 ± 0.06
60–70	23.44 ± 0.06	27.38 ± 0.07	27.65 ± 0.05
70–100	9.85 ± 0.03	10.65 ± 0.04	10.04 ± 0.03

the assumption of boost invariance is given as follows:

$$\epsilon_{\mathrm{Bj}} = \frac{1}{\tau S_{\mathrm{T}}} \frac{dE_{\mathrm{T}}}{dy}, \tag{4.4}$$

Where dE_{T}/dy represents the transverse energy density at midrapidity at the formation time τ and S_{T} is the transverse overlap area of the two colliding nuclei. A finite formation time of $\tau = 1\,\mathrm{fm}/c$ is assumed in this work for the estimation of the Bjorken energy density, as Eq. 4.4 diverges in the limit $\tau \to 0$. The total transverse energy produced in an event is denoted by E_{T}, and the transverse overlap area of the colliding nuclei is given by $S_{\mathrm{T}} = \pi R^2$. The nuclear radius R is parameterized as $R = R_0 A^{1/3}$, where the mass number is approximated by $A = N_{\mathrm{part}}/2$.

$$S_{\mathrm{T}} = \pi R_0^2 \left(\frac{N_{\mathrm{part}}}{2} \right)^{2/3} \tag{4.5}$$

Since pions, kaons, and protons are so abundant that they carry the majority of the transverse energy, the total transverse energy (E_{T}) can be approximately calculated as [17]:

$$\frac{dE_{\mathrm{T}}}{dy} \approx \frac{3}{2} \times \left(\langle m_{\mathrm{T}} \rangle \frac{dN}{dy} \right)_{\pi^{\pm}} + 2 \times \left(\langle m_{\mathrm{T}} \rangle \frac{dN}{dy} \right)_{K^{\pm},p,\bar{p}}. \tag{4.6}$$

The multiplicative factor in each term takes care of the corresponding neutral particles that are not detectable experimentally. $m_{\mathrm{T}} = \sqrt{p_{\mathrm{T}}^2 + m^2}$ is the transverse mass, and dN/dy is the integrated yield for $\pi^{\pm}$, $K^{\pm}$, and $p + \bar{p}$ in the mid-rapidity region, i.e., $|y| < 0.5$. Eq. 4.4 can now be written as,

$$\epsilon_{\mathrm{Bj}} \approx \frac{1}{\tau \pi R_0^2 \left(\frac{N_{\mathrm{part}}}{2} \right)^{2/3}} \left[\frac{3}{2} \times \left(\langle m_{\mathrm{T}} \rangle \frac{dN}{dy} \right)_{\pi^{\pm}} + 2 \times \left(\langle m_{\mathrm{T}} \rangle \frac{dN}{dy} \right)_{K^{\pm},p,\bar{p}} \right] \tag{4.7}$$

The integrated yields and mean transverse momenta for protons, kaons, and pions as a function of centrality classes for O-O collisions at $\sqrt{s_{\mathrm{NN}}} = 7$ TeV are displayed in Fig. 4.3.

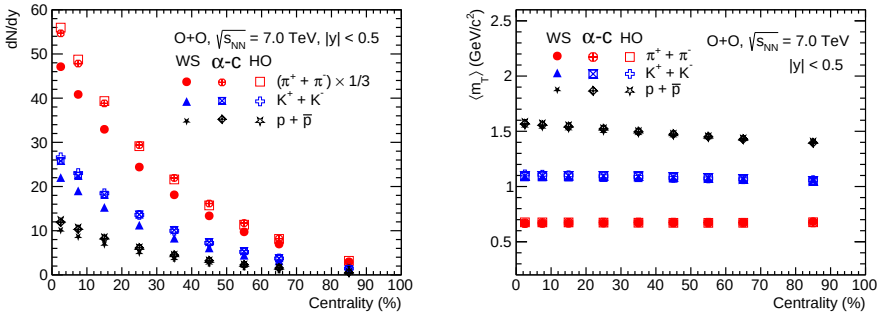

Figure 4.3: Centrality dependence of the integrated yield (left) and mean transverse mass (right) at mid-rapidity for pions, kaons, and protons in O-O collisions at $\sqrt{s_{\mathrm{NN}}} = 7$ TeV [17].

As expected, pions have a higher integrated yield than kaons and protons because they are the most abundant among the identified particles and are understood from a thermalized Boltzmannian production of secondaries in nuclear

collisions. The harmonic oscillator density profile produces more soft particles in central collisions than the Woods-Saxon density profile. The α-clustered structure demonstrates similar behavior to the harmonic oscillator density profile. However, the mean transverse mass is nearly the same for all cases.

The Bjorken energy density, as expressed in Eq. 4.7, is derived using the integrated yields and average transverse momenta of pions, kaons, and protons. Open markers denote the harmonic oscillator and solid markers indicate the Woods-Saxon density profile, and cross-referenced markers show the outcomes for the α-clustered structure.

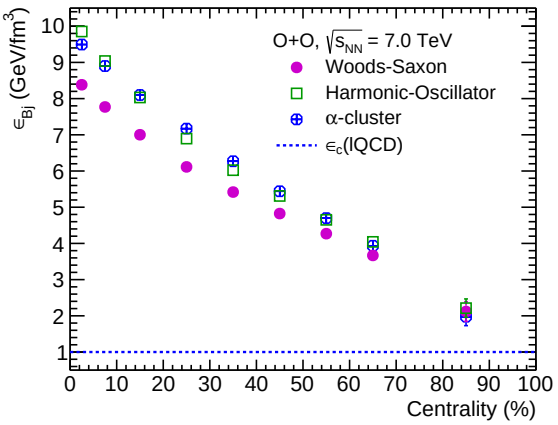

Figure 4.4: Centrality dependence of Bjorken energy density for pions, kaons, and protons in O-O collisions at $\sqrt{s_{\rm NN}} = 7$ TeV [17].

As shown in Fig. 4.4, the Bjorken energy density is found to be highest in the most central collisions and decreases approximately linearly toward more peripheral collisions. Bjorken energy density is strongly dependent on integrated yield, as shown in Eq. 4.7. The difference in integrated yield between different nuclear density profiles is reflected in the Bjorken energy density. The oxygen nucleus with harmonic oscillator density profile has approximately 15% higher energy density compared to the Woods-Saxon density profile. As observed for the

integrated yield, the α-clustered structure exhibits a similar trend in the Bjorken energy density as that seen with the harmonic oscillator density profile. The nuclear density profile affects the initial energy density of a fireball, influencing particle production and space-time evolution, ultimately affecting the equation of state (EoS). The initial energy densities for all collision centralities are higher than the 1 GeV/fm^3 value predicted by lattice QCD for the deconfinement transition [38]. This hints that QGP signals may be detectable in oxygen-oxygen collisions at LHC energies. In the following sections, we will strengthen these arguments and explore additional global observables in heavy-ion collisions.

4.4.2 Pseudorapidity distributions and squared speed of sound

Figure 4.5 illustrates the pseudorapidity distributions of charged particles in O-O collisions at $\sqrt{s_{\rm NN}} = 7$ TeV for centrality classes of (0-5)% and (70-100)% using Woods-Saxon, harmonic oscillator, and α-clustered density profiles. The variation in charged particles at mid-pseudorapidity is attributed to changes in nuclear density profiles, which is prominently observed in central collisions, whereas the variation is less pronounced in peripheral collisions. Nonetheless, at forward pseudorapidity, the multiplicity of charged particles shows minimal dependence on the density profiles.

According to the Landau hydrodynamical model [39], the rapidity distributions should be Gaussian. In this framework, the speed of sound (c_s) is connected to the rapidity distribution's width using the following formula.

$$\sigma_y^2 = \frac{8}{3}\frac{c_s^2}{1-c_s^2}\ln\left(\frac{\sqrt{s_{\rm NN}}}{2m_p}\right). \tag{4.8}$$

Where σ_y is the width of the rapidity distribution, and m_p is the mass of

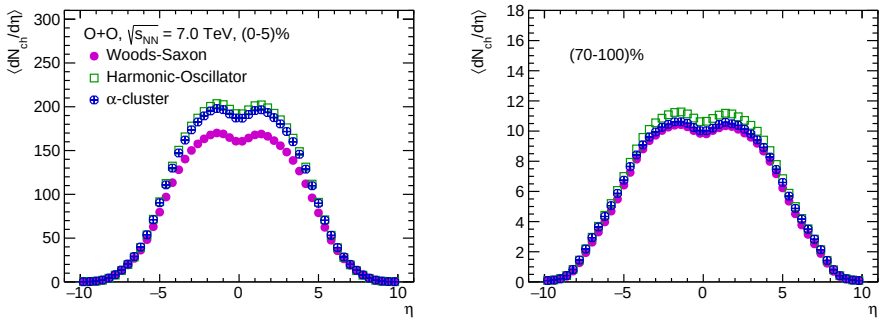

Figure 4.5: Charged particle pseudorapidity distributions in O-O collisions at $\sqrt{s_{\rm NN}} = 7$ TeV for the centrality classes (0-5)% (left) and (70-100)% (right) [17].

a proton. The massless ideal gas limit for the squared speed of sound (c_s^2) is 0.33. However, due to the dip observed at mid-pseudorapidity in pseudorapidity distributions, fitting them with a single Gaussian function is often inadequate. Generally, in experiments [40, 41], the following double Gaussian distribution is used to fit the pseudorapidity distributions and extrapolate the distributions to unmeasured regions.

$$A_1 e^{\frac{-\eta^2}{2\sigma_1^2}} - A_2 e^{\frac{-\eta^2}{2\sigma_2^2}}. \tag{4.9}$$

In this context, A_1 and A_2 serve as the normalization parameters, while σ_1 and σ_2 represent the widths of each Gaussian distribution. We have applied Eq. 4.9 to fit the pseudorapidity distribution and determined the values of σ_1 and σ_2. As shown in Table 4.3, the values of σ_1 and σ_2 are comparable within the margin of error. Figure 4.6 illustrates the squared speed of sound for pions, kaons, and protons as it varies with centrality in O-O collisions at $\sqrt{s_{\rm NN}} = 7$ TeV, using Woods-Saxon, harmonic oscillator, and α-clustered density profiles, as per Eq. 4.8. The absolute value was derived using σ_1, and the maximum deviation between σ_1 and σ_2 was used to estimate the uncertainties for c_s^2. Taking these uncertainties into account, c_s^2 appears to remain consistent across different centrality levels. The weak dependence of c_s^2 on centrality classes may indicate

that the medium created in O–O collisions is significantly less dense compared to that formed in Pb–Pb collisions. It should be noted here, the application of Landau hydrodynamics at TeV energies is a crude approximation to extract the speed of sound from the pseudorapidity distribution of the secondaries produced in heavy-ion collisions.

Table 4.3: Double-Gaussian width parameters obtained by fitting the pseudorapidity distributions in the range $|\eta| < 0.5$ using Eq. 4.9.

Centrality(%)	**Woods-Saxon**		**harmonic oscillator**		α **cluster**	
	σ_1	σ_2	σ_1	σ_2	σ_1	σ_2
0–5	2.35 ± 0.04	2.22 ± 0.04	2.31 ± 0.04	2.20 ± 0.04	2.33 ± 0.04	2.21 ± 0.04
5–10	2.34 ± 0.04	2.24 ± 0.04	2.31 ± 0.04	2.24 ± 0.03	2.32 ± 0.04	2.22 ± 0.04
10–20	2.34 ± 0.03	2.25 ± 0.03	2.32 ± 0.04	2.21 ± 0.03	2.33 ± 0.04	2.22 ± 0.04
20–30	2.34 ± 0.02	2.27 ± 0.03	2.32 ± 0.03	2.24 ± 0.03	2.32 ± 0.03	2.25 ± 0.03
30–40	2.35 ± 0.02	2.30 ± 0.02	2.33 ± 0.02	2.27 ± 0.02	2.33 ± 0.02	2.27 ± 0.02
40–50	2.36 ± 0.01	2.33 ± 0.01	2.33 ± 0.02	2.29 ± 0.02	2.33 ± 0.02	2.29 ± 0.02
50–60	2.37 ± 0.01	2.35 ± 0.01	2.36 ± 0.01	2.33 ± 0.01	2.36 ± 0.01	2.32 ± 0.01
60–70	2.38 ± 0.01	2.36 ± 0.01	2.38 ± 0.01	2.35 ± 0.01	2.37 ± 0.01	2.35 ± 0.01
70–100	2.48 ± 0.01	2.44 ± 0.01	2.47 ± 0.01	2.46 ± 0.01	2.45 ± 0.01	2.44 ± 0.01

4.4.3 p_T -spectra and kinetic freeze-out parameters

Figure 4.7 depicts the simultaneous fitting of identified particles' p_{T}-spectra with Boltzmann-Gibbs blastwave distribution in O-O collisions at $\sqrt{s_{\mathrm{NN}}}$. = 7 TeV for (0-5)% (left) and (70-100)% (right) centrality classes of Woods-Saxon, harmonic oscillator density profiles, and α-clustered structure in oxygen nucleus. The fitting ranges for each particle are comparable to those reported by ALICE [42]. The χ^2-minimization method is used to fit the data, and the values of χ^2 per degree of freedom are displayed in each case in Fig 4.7.

The formula for invariant yield in the Boltzmann-Gibbs blastwave

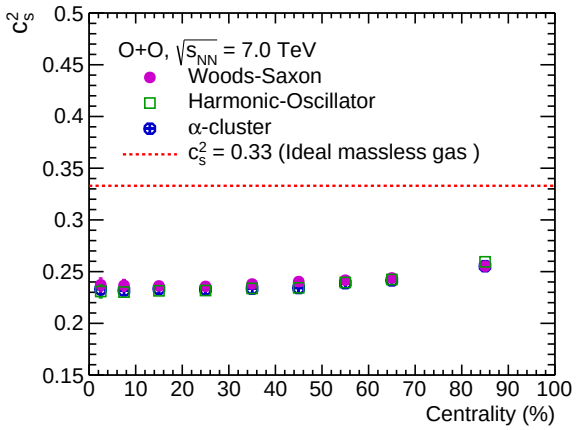

Figure 4.6: Centrality dependence of the squared speed of sound for pions, kaons, and protons in O-O collisions at $\sqrt{s_{\rm NN}} = 7$ TeV [17].

$$E\frac{d^3N}{dp^3} = C\int d^3\sigma_\mu p^\mu \exp(-\frac{p^\mu u_\mu}{T_{\rm kin}}). \tag{4.10}$$

Where C is the normalisation constant. The four-momentum of a particle is given by,

$$p^\mu \;=\; (m_T\cosh y,\; p_T\cos\phi,\; p_T\sin\phi,\; m_T\sinh y), \tag{4.11}$$

and the four-velocity is given by,

$$u^\mu = \cosh\rho\;(\cosh\eta,\;\tanh\rho\;\cos\phi_r,\;\tanh\rho\;\sin\phi_r,\;\sinh\;\eta). \tag{4.12}$$

Finally, the freeze-out surface is written as,

$$d^3\sigma_\mu \;=\; (\cosh\eta,\;0,\;0,-\sinh\eta)\;\tau\;r\;dr\;d\eta\;d\phi_r. \tag{4.13}$$

here, η is the space-time rapidity. Now, Eq. 4.10 is expressed as,

$$\left.\frac{d^2N}{dp_T dy}\right|_{y=0} = Cp_T m_T\int_0^{R_0} r\;dr\;K_1\Big(\frac{m_T\;\cosh\rho}{T_{\rm kin}}\Big)I_0\Big(\frac{p_T\;\sinh\rho}{T_{\rm kin}}\Big). \tag{4.14}$$

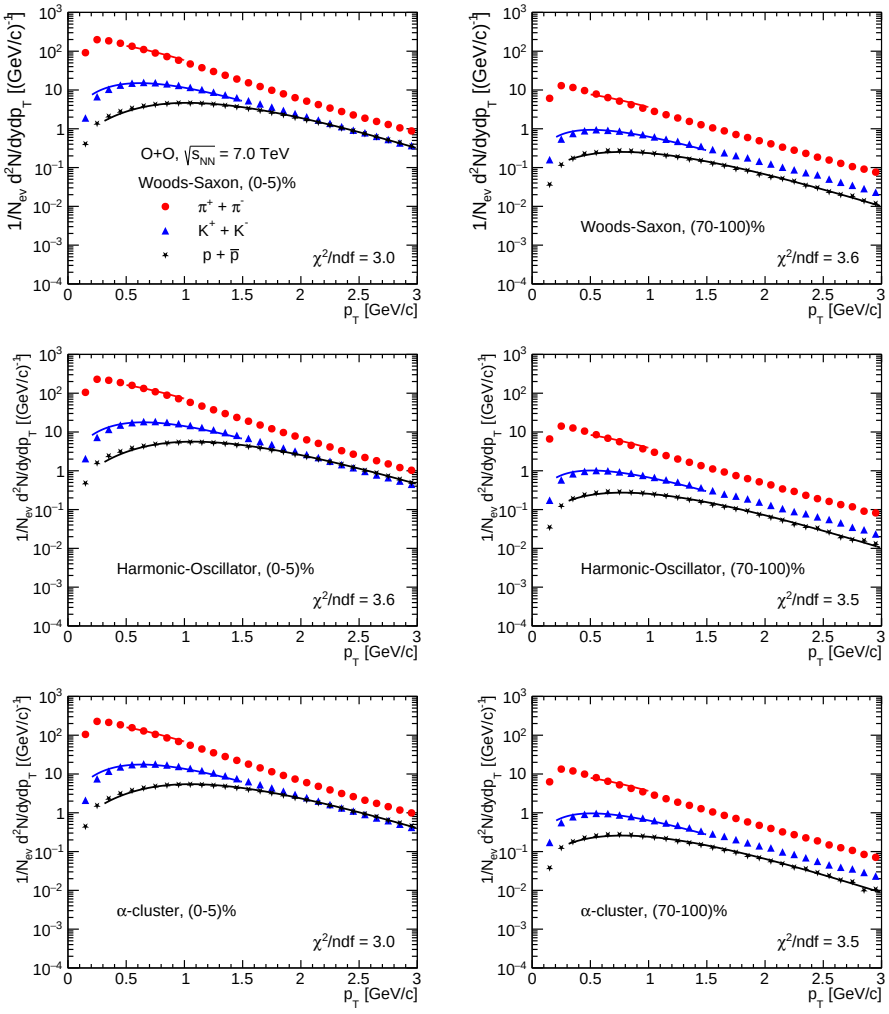

Figure 4.7: Blast-wave model fits to the transverse momentum (p_{T}) spectra of identified particles in O–O collisions at $\sqrt{s_{\mathrm{NN}}} = 7$ TeV. Left and right panels represent the (0–5)% and (70–100)% centrality classes, respectively [17].

$K_1\Big(\frac{m_T \cosh\rho}{T_{\mathrm{kin}}}\Big)$ and $I_0\Big(\frac{p_T \sinh\rho}{T_{\mathrm{kin}}}\Big)$ are modified Bessel's functions, which are given by,

$$K_1\Big(\frac{m_T \cosh\rho}{T_{\mathrm{kin}}}\Big) = \int_0^{\infty} \cosh y \exp\Big(-\frac{m_T \cosh y \cosh\rho}{T_{\mathrm{kin}}}\Big) dy,$$

$$I_0\Big(\frac{p_T \sinh\rho}{T_{\mathrm{kin}}}\Big) = \frac{1}{2\pi}\int_0^{2\pi} \exp\Big(\frac{p_T \sinh\rho \cos\phi}{T_{\mathrm{kin}}}\Big) d\phi,$$

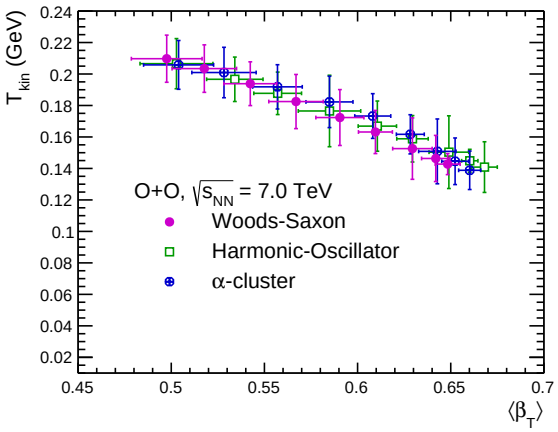

Figure 4.8: Variation of kinetic freeze-out temperature with transverse radial flow velocity, obtained from simultaneous Boltzmann-Gibbs blast-wave fits to the transverse momentum spectra of identified particles in O–O collisions at $\sqrt{s_{\rm NN}}$ = 7 TeV [17].

where, ρ is given by $\rho = \tanh^{-1}\beta_{\rm T}$ and $\beta_{\rm T}(= \beta_s\xi^n)$ is the radial flow [43–46] . Here, β_s is the maximum surface velocity, r is the radial distance, and ξ is given as (r/R_0). The source's maximum radius at freeze-out is R_0.

According to this model, the particles near the fireball's center move more slowly than those near its edges. The average transverse velocity is calculated as follows: [47],

$$\langle\beta_{\rm T}\rangle = \frac{\int \beta_s\xi^n\xi\ d\xi}{\int \xi\ d\xi} = \Big(\frac{2}{2+n}\Big)\beta_s. \tag{4.15}$$

For our calculation, we kept n as a free parameter. Figure 4.8 depicts the kinetic freeze-out temperature versus transverse radial flow from a simultaneous fit of identified particles' $p_{\rm T}$-spectra with Boltzmann-Gibbs blastwave distribution (Eq. 4.14) in O-O collisions at $\sqrt{s_{\rm NN}}$ = 7 TeV. In all cases, the average transverse flow ($\langle\beta_T\rangle$) and the kinetic freeze-out temperature ($T_{\rm kin}$) have a similar correlation within uncertainties. $T_{\rm kin}$ is the lowest, and the transverse flow is the highest for

the most central collisions (0–5% class). The larger system size in these collisions leads to a prolonged hadronic phase and reduced $T_{\rm kin}$. Additionally, the highest radial flow is anticipated because of the largest system size. For Pb-Pb collisions at LHC energies, a similar pattern is observed [42].

Table 4.4: Kinetic freeze-out temperature and transverse radial flow parameter extracted from the Boltzmann-Gibbs blast-wave fit using Eq. 4.14.

Centrality(%)	**Woods-Saxon**		**harmonic oscillator**		**α-cluster**	
	$T_{\rm kin}$ (GeV)	$\langle\beta_T\rangle$	$T_{\rm kin}$ (GeV)	$\langle\beta_T\rangle$	$T_{\rm kin}$ (GeV)	$\langle\beta_T\rangle$
0–5	0.143 ± 0.013	0.65 ± 0.01	0.141 ± 0.016	0.67 ± 0.01	0.139 ± 0.012	0.66 ± 0.01
5–10	0.146 ± 0.015	0.64 ± 0.01	0.145 ± 0.007	0.66 ± 0.00	0.145 ± 0.015	0.65 ± 0.01
10–20	0.153 ± 0.019	0.63 ± 0.01	0.150 ± 0.231	0.65 ± 0.01	0.151 ± 0.021	0.64 ± 0.01
20–30	0.163 ± 0.014	0.61 ± 0.01	0.159 ± 0.015	0.63 ± 0.01	0.162 ± 0.012	0.63 ± 0.01
30–40	0.172 ± 0.018	0.59 ± 0.01	0.167 ± 0.016	0.61 ± 0.01	0.173 ± 0.014	0.61 ± 0.01
40–50	0.182 ± 0.017	0.57 ± 0.01	0.177 ± 0.022	0.58 ± 0.02	0.182 ± 0.016	0.58 ± 0.01
50–60	0.194 ± 0.013	0.54 ± 0.01	0.188 ± 0.013	0.56 ± 0.01	0.192 ± 0.014	0.56 ± 0.01
60–70	0.203 ± 0.015	0.52 ± 0.02	0.197 ± 0.014	0.53 ± 0.01	0.201 ± 0.016	0.53 ± 0.02
70–100	0.210 ± 0.015	0.50 ± 0.02	0.206 ± 0.008	0.50 ± 0.01	0.206 ± 0.016	0.50 ± 0.02

4.4.4 Particle ratios

Figure 4.9 depicts the $p_{\rm T}$-differential proton-to-pion and kaon-to-pion ratios in O-O collisions at $\sqrt{s_{\rm NN}}$ = 7 TeV for (0-5)% and (70-100)% centrality classes. The ratios of both kaons to pions and protons to pions increase with $p_{\rm T}$. Since the kaon-to-pion ratio reflects strangeness production, this indicates an enhancement in strangeness as $p_{\rm T}$ rises. This enhancement appears to be similar for both centrality classes at low-$p_{\rm T}$. However, at intermediate-$p_{\rm T}$, the enhancement is more pronounced for the (0-5)% centrality class. The proton-to-pion ratio, which compares the lightest baryon to the lightest meson, serves as a proxy for the baryon-to-meson ratio. For (70-100)%, the particle ratios do not exhibit any

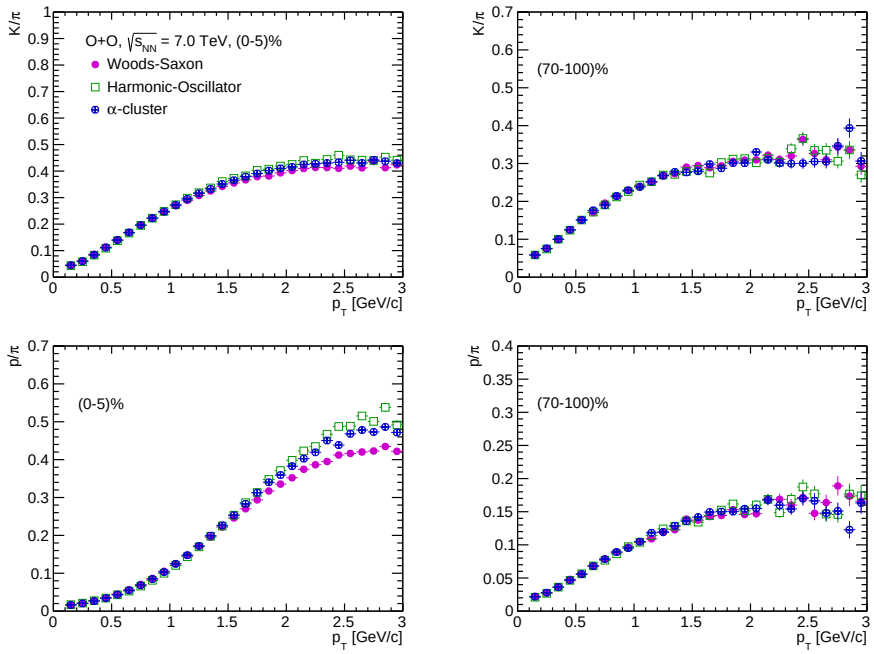

Figure 4.9: p_{T}-dependent K/π (top) and p/π (bottom) ratios in O–O collisions at $\sqrt{s_{\mathrm{NN}}} = 7$ TeV for central (0–5)% and peripheral (70–100)% events (left and right panels, respectively [17].

dependence on the density profiles. The kaon-to-pion and proton-to-pion ratios, however, increase for the (0-5)% centrality class at intermediate-p_{T} for the harmonic oscillator density profile in comparison to the Woods-Saxon density profile, becoming noticeable at higher p_{T}. The results for the harmonic oscillator density profile are comparable to those for the α-clustered structure.

4.5 Anisotropic flow

Research on QGP focuses on examining all indirect indicators because QGP is a very short-lived state due to the nature of strongly interacting matter. It undergoes rapid expansion, and its evolution is effectively described through relativistic viscous hydrodynamics and dissipative effects. This collective expansion of the QGP embeds the initial-state collision geometry, as well as fluctuations in energy

and entropy density, in the final-state multi-particle correlations [48–50]. The Fourier coefficients (v_2 and v_3) of the azimuthal momentum distribution of the final-state hadrons [51] are often quantified in order to study this as the medium response to the initial eccentricity (ϵ_2) and triangularity (ϵ_3). Hydrodynamic equations predict that QGP behaves as a perfect fluid, which is supported by experimental observations of flow coefficients [52]. Thus, the presence of finite flow coefficients is regarded as an indicator of the QGP's hydrodynamic behavior and, thus, thermalization in the early stages of the collision. Recent observations of similar signatures have been observed in small collision systems, such as high-multiplicity *pp* collisions, where collectivity or hydrodynamic expansion is typically not seen [53]. Hydrodynamics' suitability for small collision systems created in ultrarelativistic nuclear collisions is also called into question by these findings. Because the system size of ^{16}O–^{16}O overlaps peripheral Pb–Pb collisions and high-multiplicity *pp* collisions, it offers an opportunity to investigate the origin of flow-like signatures in small collision systems.

In this section, we investigate the eccentricity (ϵ_2), triangularity (ϵ_3), normalized symmetric cumulants [NSC(2,3)], elliptic flow (v_2), triangular flow (v_3) in ^{16}O-^{16}O collisions at $\sqrt{s_{\rm NN}}$ = 7 TeV. The constituent quark number scaling of the elliptic flow is also reported.

4.5.1 Methodology for estimation of anisotropic flow (Two-particle correlation method)

In non-central heavy-ion collisions, the collision overlap region is anisotropic in space. In these collisions, the initial spatial anisotropies can be changed into momentum space azimuthal anisotropies by the pressure gradient of the thermalized partonic medium. These azimuthal anisotropies of various orders can be measured using the coefficients of the Fourier series decomposition of the final-state

particle momentum distribution, which are as follows:

$$E\frac{d^3N}{dp^3} = \frac{d^2N}{2\pi p_{\mathrm{T}} dp_{\mathrm{T}} dy}\left(1 + 2\sum_{n=1}^{\infty} v_n \cos[n(\phi - \psi_n)]\right). \tag{4.16}$$

Here, ψ_n denotes the nth harmonic event plane angle, and ϕ denotes the azimuthal angle of the final-state particles in the transverse plane [54]. $n = 1$ denoting directed flow, $n = 2$ denoting elliptic flow, and $n = 3$ denoting triangular flow, v_n is the nth-order anisotropic flow coefficient. The following method can be used to estimate anisotropic flow coefficients of various orders:

$$v_n = \langle \cos[n(\phi - \psi_n)] \rangle \tag{4.17}$$

It is difficult to determine the event plane angle in experiments, and Eq. 4.17 accounts for non-flow effects like resonance decay and jet contributions. However, by using a proper pseudorapidity gap, a two-particle correlation method to estimate the flow coefficients can effectively reduce the non-flow contribution and does not require the event-plane angle. The pseudorapidity dependence of ψ_n, which is seen in the experiments, has been ignored in this study.

The following procedures can be used to determine the two-particle correlation function, which is necessary in order to estimate the anisotropic flow coefficients using the two-particle correlation method [55]:

1. The transverse momenta of each event are used to create two sets of particles, "a" and "b". The trigger particles are indicated by "a" and the associated particle set by "b".

2. The relative pseudorapidities ($\Delta\eta = \eta_a - \eta_b$) and relative azimuthal angles ($\Delta\phi = \phi_a - \phi_b$) are calculated for each particle from the trigger group ("a") that pairs with each particle from the associate group ("b").

3. We determine the same event pairs ($S(\Delta\eta, \Delta\phi)$) and mixed event pairs ($B(\Delta\eta, \Delta\phi)$). In the mixed event pair, "a" and "b" are from different events, where "a" pairs with "b" from five randomly chosen events to eliminate physical correlations. In the same event pair, both "a" and "b" belong to the same event.

4. The correlation function for two particles ($C(\Delta\eta, \Delta\phi)$) is calculated by dividing $S(\Delta\eta, \Delta\phi)$ by $B(\Delta\eta, \Delta\phi)$.

We employ final-state charged hadrons in this analysis to cover a wider range of particles, with kinematic cuts as $|\eta| < 2.5$ and $p_{\mathrm{T}} > 0.4$ GeV/c. Carefully chosen is the $\Delta\eta$ interval to exclude the jet peak region observed in the $C(\Delta\eta, \Delta\phi)$ distribution. The 1D correlation $C(\Delta\phi)$ is obtained by implementing the interval $1.0 < |\Delta\eta| < 4.8$ in our case.

$$C(\Delta\phi) = \frac{dN_{\mathrm{pairs}}}{d\Delta\phi} = A \times \frac{\int S(\Delta\eta, \Delta\phi) d\Delta\eta}{\int B(\Delta\eta, \Delta\phi) d\Delta\eta}. \tag{4.18}$$

The normalization constant A in this case ensures that the number of pairs in the same events and mixed events is equal at a given $\Delta\eta$ interval.

The pair distribution (N_{pairs}) or 1D correlation function can be expanded into a Fourier transform in $\Delta\phi$ as follows:

$$C(\Delta\phi) = \frac{dN_{\mathrm{pairs}}}{d\Delta\phi} \propto \left[1 + 2\sum_{n=1}^{\infty} v_{n,n}(p_{\mathrm{T}}^{a}, p_{\mathrm{T}}^{b}) \cos(n\Delta\phi)\right]. \tag{4.19}$$

$v_{n,n}$ represents the two-particle flow coefficient. In this definition, the convolution of the particle pair removes the event plane angle. Now, $v_{n,n}$ can be obtained as follows:

$$v_{n,n}(p_{\mathrm{T}}^{a}, p_{\mathrm{T}}^{b}) = \langle cos(n\Delta\phi) \rangle \tag{4.20}$$

In terms of p_{T}^{a} and p_{T}^{b}, $v_{n,n}$ are symmetric functions. The definition of harmonics in Eq. 4.16 enters to Eq. 4.19, which can be written as:

$$\frac{dN_{\mathrm{pairs}}}{d\Delta\phi} \propto \left[1 + 2\sum_{n=1}^{\infty} v_n(p_{\mathrm{T}}^{a}) v_n(p_{\mathrm{T}}^{b}) \cos(n\Delta\phi)\right]. \tag{4.21}$$

If collective expansion is what causes azimuthal anisotropy, then $v_{n,n}$ can be factorized into the product of two single-particle harmonic coefficients.

$$v_{n,n}(p_{\mathrm{T}}^{a}, p_{\mathrm{T}}^{b}) = v_n(p_{\mathrm{T}}^{a}) v_n(p_{\mathrm{T}}^{b}). \tag{4.22}$$

From Eq. 4.22, v_n can be estimated as:

$$v_n(p_{\mathrm{T}}^{a}) = v_{n,n}(p_{\mathrm{T}}^{a}, p_{\mathrm{T}}^{b}) / \sqrt{v_{n,n}(p_{\mathrm{T}}^{b}, p_{\mathrm{T}}^{b})} \tag{4.23}$$

Following the above steps, the nth-order coefficients of the azimuthal anisotropy of all-charged particles can be obtained using AMPT model at the LHC energies, along with identified particles like $\pi^{\pm}$, $K^{\pm}$, and $p+\bar{p}$ for the O-O collision system.

4.5.2 Eccentricity and triangularity

Eccentricity represents the elliptic shape of the overlap region of the colliding nucleons, which is purely geometric; however, triangularity represents the triangular shape of the region, which results from the event-by-event density fluctuations in the collision overlap region. The initial geometrical anisotropies contribute significantly to the anisotropic flow coefficients of the final-state hadrons. Eccentricity has a significant impact on elliptic flow, while triangularity has a limited influence on triangular flow (65-70%) for a minimally viscous fluid [56].

The eccentricity and triangularity are difficult to determine in experiments, but they can be estimated in the AMPT model using the following expression [57, 58]:

$$\epsilon_{\rm n} = \frac{\sqrt{\langle r^{\rm n}\cos(n\phi_{\rm part})\rangle^2 + \langle r^{\rm n}\sin(n\phi_{\rm part})\rangle^2}}{\langle r^{\rm n}\rangle} \tag{4.24}$$

where r and $\phi_{\rm part}$ are the polar co-ordinates of the participants. In ϵ_n, n = 2 corresponds to eccentricity (ϵ_2) and n = 3 corresponds to triangularity (ϵ_3). Fig. 4.10 shows the event averaged eccentricity ($\langle\epsilon_2\rangle$) (left), triangularity ($\langle\epsilon_3\rangle$) (middle), and their ratios (right) for the Woods-Saxon density profile and α-clustered structure in O-O collisions at $\sqrt{s_{\rm NN}}$ = 7 TeV using AMPT model. As the impact parameter of the collisions increases, the overlap region becomes substantially elliptic, and the value of $\langle\epsilon_2\rangle$ is shown to be increasing towards the peripheral collisions. With the exception of mid-central situations, when the values of $\langle\epsilon_2\rangle$ are identical for both profiles, $\langle\epsilon_2\rangle$ is lower for the α-cluster case than for the Woods-Saxon nuclear density profile for a given centrality class. This suggests that the distribution of nucleons inside the nucleus plays a significant role in the eccentricity, which is expected to be reflected in the anisotropic flow coefficients, given the hydrodynamical behavior of the formed medium, even if the number of participants in a collision is similar.

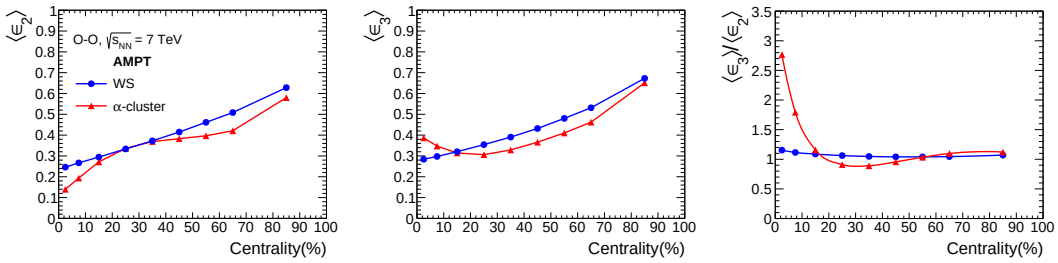

Figure 4.10: Average eccentricity ($\langle\epsilon_2\rangle$), triangularity ($\langle\epsilon_3\rangle$), and $\langle\epsilon_3\rangle/\langle\epsilon_2\rangle$ as a function of centrality for Woods-Saxon and α-cluster nuclear density profiles in O-O collisions at $\sqrt{s_{\rm NN}}$ = 7 TeV, as obtained using the AMPT string melting model [15].

Both the Woods-Saxon and α-cluster density profiles show a similar pattern

of $\langle\epsilon_3\rangle$ as a function of centrality, with the mean triangularity increasing towards the periphery of collisions due to the appearance of a more triangular shape. The trend of $\langle\epsilon_3\rangle$ as a function of centrality shows a peculiar behaviour for the α-cluster case, where the value decreases from central to mid-central collisions, reaches a minimum, and then starts to increase again towards the peripheral collisions. However, throughout the centrality selection, the Woods-Saxon nuclear density profile value consistently surpasses the α-cluster structure, except for the most central cases, which are (0–5)% and (5–10)%. Because of its greater triangularity in the most centre collisions, the α-cluster structure may exhibit more notable event-by-event changes in the participant distribution. A comparable analysis employing AMPT for the most central ($b = 0$) O-O collisions at $\sqrt{s_{\rm NN}} = 6.37$ TeV is reported in Ref. [20]. When considering a particular nuclear profile option, the reported values for $\langle\epsilon_2\rangle$ and $\langle\epsilon_3\rangle$ exhibit a similar pattern. While the $\langle\epsilon_3\rangle$ values are nearly equal to those in the current study, the $\langle\epsilon_2\rangle$ values in Ref. [20] are larger. In contrast to the current study, which uses the initial participant nucleons, this might be because the initial partons were used to estimate $\langle\epsilon_2\rangle$ and $\langle\epsilon_3\rangle$.

The right-most panel of Fig. 4.10 presents the ratio $\langle\epsilon_3\rangle/\langle\epsilon_2\rangle$ as a function of centrality for O-O collisions at $\sqrt{s_{\rm NN}} = 7$ TeV using AMPT, comparing Woods-Saxon and α-clustered nuclear profiles. The ratio is significantly higher for the α-clustered case in the most central collisions, while it fluctuates around unity and aligns with the Woods-Saxon results in mid-central to peripheral collisions. This indicates a strong interplay between collision geometry and nucleon distribution fluctuations. Only the α-clustered structure exhibits the exceptionally high value of $\langle\epsilon_3\rangle/\langle\epsilon_2\rangle$ in the most central collisions.

Figure 4.11 shows the distributions of eccentricity (ϵ_2) and triangularity (ϵ_3) for the most central (0–5)% O–O collisions at $\sqrt{s_{\rm NN}} = 7$ TeV, calculated using the AMPT model for both Woods-Saxon (left) and α-clustered (right) density

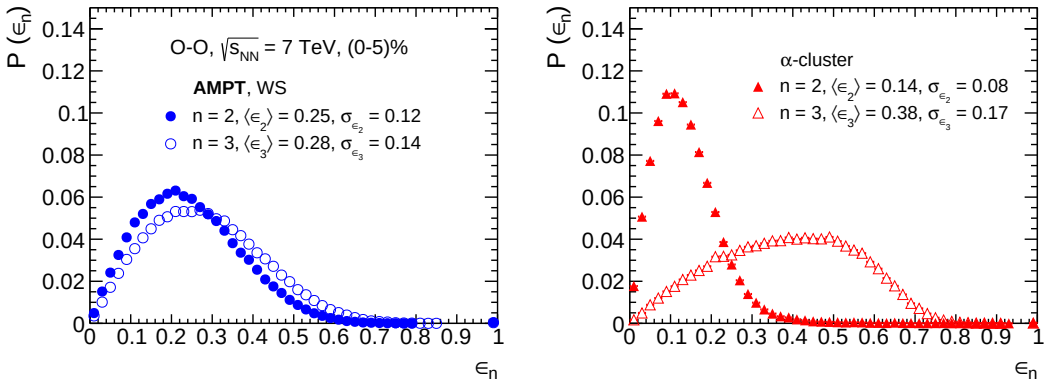

Figure 4.11: Distributions of eccentricity ($\langle\epsilon_2\rangle$) and triangularity ($\langle\epsilon_3\rangle$) for the most central O–O collisions at $\sqrt{s_{\rm NN}} = 7$ TeV, shown for Woods-Saxon (left) and α-cluster (right) nuclear density profiles [15].

profiles. The ϵ_2 distribution for the α-clustered structure exhibits a lower mean and standard deviation compared to the Woods-Saxon case, suggesting a more isotropic distribution of participating nucleons. In contrast, the ϵ_3 distribution is broader for the α-clustered configuration, indicating enhanced event-by-event fluctuations in the initial geometry. Its standard deviation and mean value are significantly higher. This suggests that the α-clustered structure has more inherent fluctuations even though the participant distribution is more isotropic in shape. These aspects of the interaction between eccentricity and triangularity in relation to different nucleon distribution profiles could be investigated using various correlation functions, such as the normalized symmetric cumulants, which are discussed in the following subsection.

4.5.3 Normalized symmetric cumulants NSC(n,m)

We define the normalised symmetric cumulant coefficient NSC(n,m) to quantify the positive or negative correlations between eccentricity and triangularity for different nuclear density profiles with regard to collision centrality, which is given by [59]:

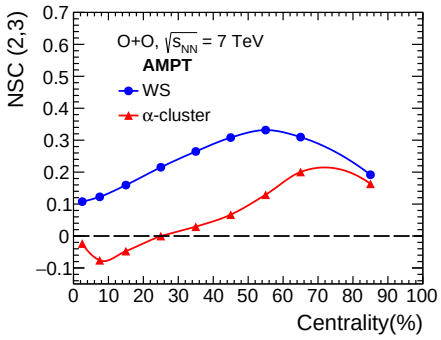

Figure 4.12: Centrality dependence of the normalized symmetric cumulant NSC(2, 3) in O–O collisions at $\sqrt{s_{\rm NN}} = 7$ TeV, using Woods-Saxon and α-cluster nuclear density profiles within the AMPT string melting model [15].

$$\mathrm{NSC(n,m)} = \frac{\langle {\varepsilon_{\rm n}}^2 {\varepsilon_{\rm m}}^2 \rangle - \langle {\varepsilon_{\rm n}}^2 \rangle \langle {\varepsilon_{\rm m}}^2 \rangle}{\langle \varepsilon_{\rm n}^2 \rangle \langle \varepsilon_{\rm m}^2 \rangle}. \tag{4.25}$$

Figure 4.12 illustrates the normalized symmetric cumulant coefficient as a function of centrality for both Woods-Saxon and α-clustered configurations in O–O collisions at $\sqrt{s_{\rm NN}} = 7$ TeV, obtained using the AMPT string melting model. An anti-correlation between the two variables is indicated by the negative coefficient values. For the α-clustered example, we find a negative correlation up to mid-central (20–30%). Accordingly, $\langle \epsilon_2 \rangle$ and $\langle \epsilon_3 \rangle$ only show anti-correlation when the density profile is α-clustering. On the other hand, in the instance of the Woods-Saxon density profile, we obtained positive correlations for all centralities.

4.5.4 Elliptic flow and triangular flow

Figure 4.13 illustrates the $p_{\rm T}$-integrated elliptic flow (left), triangular flow (middle), and their ratio (right) as functions of collision centrality in O-O collisions at $\sqrt{s_{\rm NN}} = 7$ TeV, obtained using the AMPT model. Results are shown for both Woods-Saxon and α-clustered nuclear density profiles. The α-clustered structure shows a large centrality dependency, whereas the elliptic flow does not show a

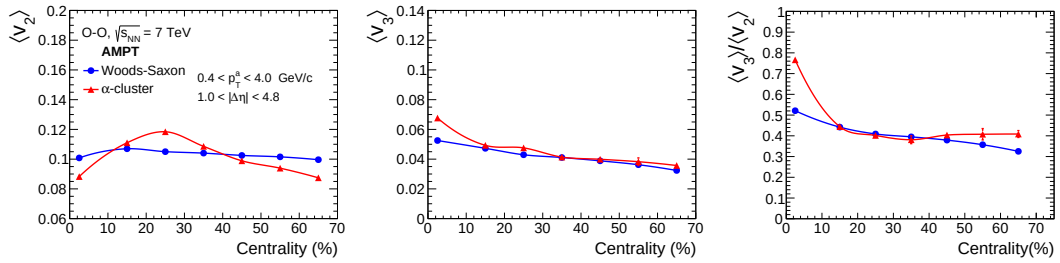

Figure 4.13: Integrated elliptic flow ($\langle v_2 \rangle$) (left), triangular flow ($\langle v_3 \rangle$) (middle), and the ratio ($\langle v_3 \rangle / \langle v_2 \rangle$) (right) as a function of centrality in O-O collisions at $\sqrt{s_{\rm NN}} = 7$ TeV for both Woods-Saxon and α-cluster type nuclear density profiles from AMPT model [15].

strong centrality dependence for the Woods-Saxon density profile. In contrast to the Woods-Saxon profile, where the elliptic flow is finite but nearly constant with centrality, the α-clustered structure's elliptic flow value increases as one moves from central to mid-central collisions, reaches a maximum around (20-30)% centrality class, and then decreases towards peripheral collisions.

On the other hand, triangular flow for the α-clustered structure and the Woods-Saxon density profile show similar patterns, with a peak at the central collisions and a decline as one moves towards the peripheral collisions. The α-clustered structure shows a more considerable triangular flow than the Woods-Saxon density profile across all centrality classes. The right plot of Fig. 4.13 displays $\langle v_3 \rangle / \langle v_2 \rangle$ as a function of centrality, and it appears to decrease for both nuclear profiles as one moves towards the peripheral collisions. In the most central and peripheral collisions for α-clustered structures, the value of $\langle v_3 \rangle / \langle v_2 \rangle$ is larger than the Woods-Saxon density profile. Interestingly, a sharp increase in the $\langle v_3 \rangle / \langle v_2 \rangle$ ratio is observed in the most central collisions, as indicated by the right panel of Fig. 4.10, which shows $\langle \epsilon_3 \rangle / \langle \epsilon_2 \rangle$ as a function of centrality. This behavior may suggest the presence of α-clustered structures in oxygen nuclei during O–O collisions, which can be confirmed through further experiments.

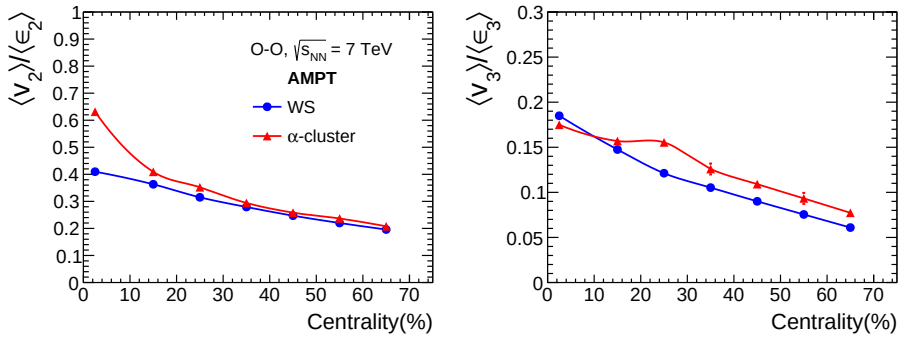

Figure 4.14: The ratio $\langle v_2\rangle/\langle\epsilon_2\rangle$ (left) and $\langle v_3\rangle/\langle\epsilon_3\rangle$ (right) for both Woods-Saxon and α-cluster type nuclear density profiles for O-O collisions at $\sqrt{s_{\rm NN}} = 7$ TeV from AMPT [15].

Fig. 4.14 depicts $\langle v_2\rangle/\langle\epsilon_2\rangle$ (left) and $\langle v_3\rangle/\langle\epsilon_3\rangle$ (right) as a function of centrality for α-clustered structure and Woods-Saxon density profile for O-O collisions at $\sqrt{s_{\rm NN}} = 7$ TeV. Both nuclear profiles show a decrease towards the peripheral collisions; however, for the α-clustered structure, both of these ratios are greater than the Woods-Saxon density profile. $\langle v_2\rangle/\langle\epsilon_2\rangle$ and $\langle v_3\rangle/\langle\epsilon_3\rangle$ both characterise how the medium affects the evolution of the flow coefficients, i.e., $\langle v_2\rangle$ and $\langle v_3\rangle$, from initial eccentricities, i.e., $\langle\epsilon_2\rangle$ and $\langle\epsilon_3\rangle$, respectively. It is well established that anisotropic flow coefficients of different orders are influenced differently by the medium created in the collision. As the order of the flow harmonics increases, their sensitivity to the medium's viscosity also becomes more pronounced [60]. The observed enhanced values of $\langle v_2\rangle/\langle\epsilon_2\rangle$ and $\langle v_3\rangle/\langle\epsilon_3\rangle$ for α-clustered structure may therefore be explained by a longer duration of the partonic or hadronic phase of the collision system in comparison to the Woods-Saxon density profile.

4.5.5 Elliptic flow of light-flavor hadrons and NCQ scaling

Figure 4.15 displays the two-particle azimuthal correlation function $C(\Delta\phi)$ for $\pi^{\pm}$, $K^{\pm}$, and $p + \bar{p}$ in the most central O-O collisions at $\sqrt{s_{\rm NN}} = 7$ TeV, plotted over the relative azimuthal angle range $\Delta\phi \in [-\pi/2, 3\pi/2]$. The correlation is

evaluated within a pseudorapidity gap of $1.0 < |\Delta\eta| < 4.8$ and for transverse momentum $0.5 < p_{\mathrm{T}}^{\mathrm{a}}, p_{\mathrm{T}}^{\mathrm{b}} < 5.0$ GeV/c, effectively suppressing short-range non-flow effects such as those from resonance decays and mini-jets. The prominence of the peaks in the correlation function reflects the strength of the anisotropic flow.

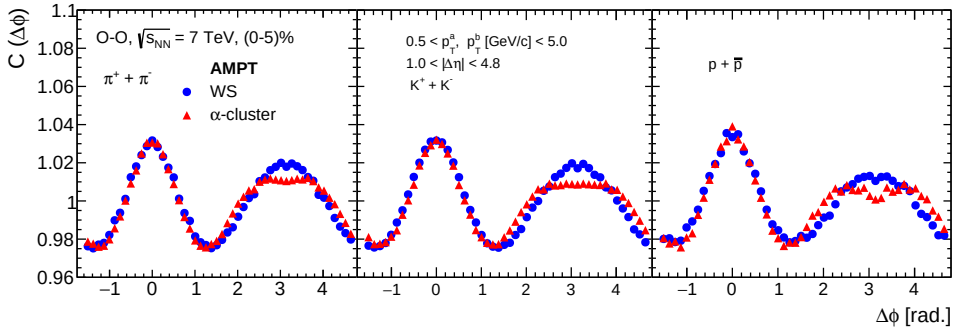

Figure 4.15: Two-particle azimuthal correlations of $\pi^{\pm}$, $K^{\pm}$, and $p + \bar{p}$ in most central O–O collisions at $\sqrt{s_{\mathrm{NN}}} = 7$ TeV, for Woods-Saxon and α-cluster nuclear density profiles [15].

The magnitudes of the near-side peaks in both density profiles ($\Delta\phi \simeq 0$) are similar. For the α-cluster scenario, the two-particle azimuthal correlation function shows an away-side ($\Delta\phi \simeq \pi$) broadening and suppression. This effect becomes more apparent when one moves from pion to kaon and ultimately to proton. The more compact and dense fireball produced in nuclear collisions with α-clusters may generate more violent interactions among partons, leading to this away-side valley. This may also result in higher multiplicity than the Woods-Saxon scenario in similar centrality bins [17]. The contribution to the triangle flow is increased when there are two peaks on the away side. [57, 61].

In conclusion, comparing the $C(\Delta\phi)$ distributions of the Woods-Saxon nucleus with the α-clustered nucleus reveals that the azimuthal correlation function is dependent on the initial density profile of the nucleus. These findings are con-

sistent with those found in Ref. [62]. It should be mentioned that away-side signal suppression could be caused by residual jet-like correlations. Compared to pion and kaon, the proton exhibits comparatively greater suppression in the medium due to its mass.

Figure 4.16 illustrates the centrality dependence of the elliptic flow coefficients (v_2) for $\pi^{\pm}$, $K^{\pm}$, and $p + \bar{p}$ in O-O collisions at $\sqrt{s_{\rm NN}} = 7$ TeV, for both Woods-Saxon and α-clustered density profiles.

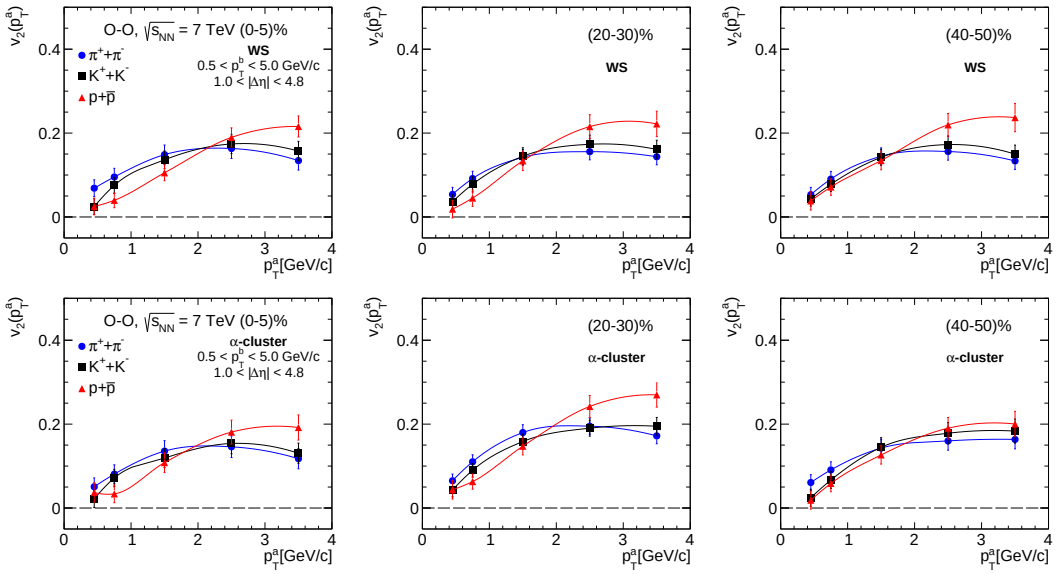

Figure 4.16: $p_{\rm T}$ dependence of elliptic flow ($v_2(p_{\rm T})$) for $\pi^{\pm}$, $\rm K^{\pm}$, and $\rm p + \bar{p}$ in O–O collisions at $\sqrt{s_{\rm NN}} = 7$ TeV, obtained using both Woods-Saxon and α-cluster charge density profiles for the oxygen nucleus [15].

For this study, three centrality bins, the most central (0-5)%, the intermediate (20-30)%, and the noncentral (40-50)%, were chosen. In the Woods-Saxon scenario, $v_2(p_{\rm T})$ has a relatively weak dependence on centrality for the three types of particles. In contrast to the other centrality bins, the α-clustered case exhibits a greater $v_2(p_{\rm T})$ in (20–30)% centrality. We argue that in the Woods-Saxon case, the smaller system size does not permit much variation in v_2 as a function of cen-

trality, regardless of an increasing ϵ_2. On the other hand, the α-cluster situation, where the more compact geometry tends to produce a relatively denser medium, introduces a variation of v_2 with respect to centrality.

Moving on to the particle types, the elliptic flow of $\pi^{\pm}$, $K^{\pm}$, and $p+\bar{p}$ exhibits a clear mass ordering at low p_{T}. This is interpreted as arising from the interplay between radial (symmetric) flow and anisotropic flow effects. The baryon-meson flow separation occurs in the intermediate p_{T} region, where baryons exhibit a larger v_2 compared to mesons. This is made possible by the hadronization quark coalescence mechanism that is incorporated into the AMPT string melting model.

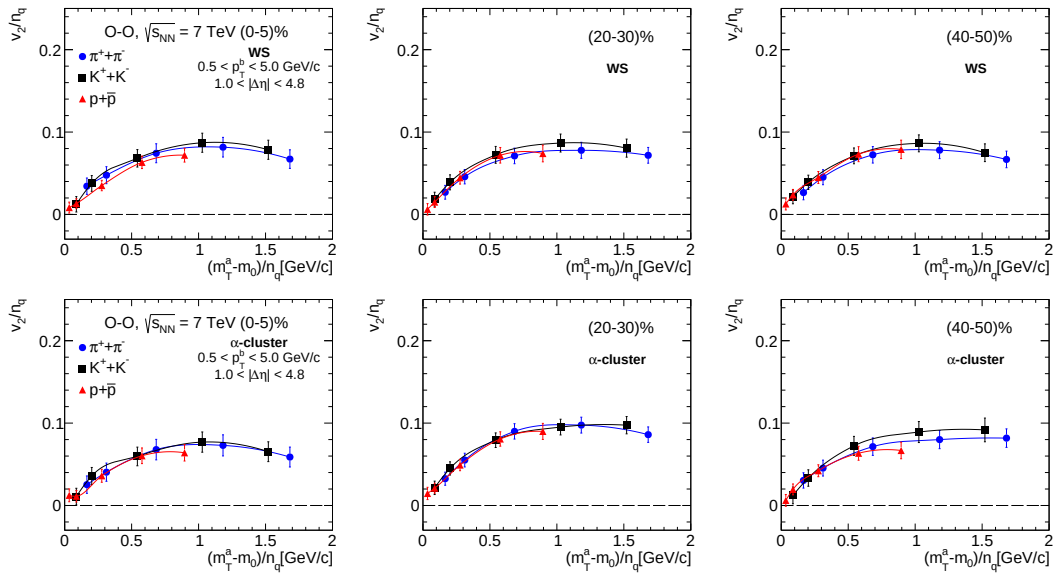

Figure 4.17: The transverse kinetic energy dependence of the constituent-quark number scaling of elliptic flow (v_2) for $\pi^{\pm}$, $K^{\pm}$, and $p+\bar{p}$ in O–O collisions at $\sqrt{s_{\mathrm{NN}}} = 7$ TeV is investigated using the AMPT model [15].

Figure 4.17 depicts the centrality dependence of $v_2(p_{\mathrm{T}}^a)/n_q$ scaling as a function of $(m_{\mathrm{T}} - m_0)/n_q$ for $\pi^{\pm}$, $K^{\pm}$ and $p+\bar{p}$ in O-O collisions at $\sqrt{s_{\mathrm{NN}}} = 7$ TeV for both Woods-Saxon and α-cluster type nuclear density profiles. Here, $KE_{\mathrm{T}} =$

$(m_{\mathrm{T}} - m_0)$, where m_{T} is the transverse mass and m_0 is the particle's rest mass, and $n_q = 2$ for mesons and $n_q = 3$ for baryons. The elliptic flow of the constituent quarks as a function of their transverse kinetic energy is quantitatively displayed in these plots. As discussed earlier, the NCQ scaling is broken in Pb-Pb collisions at the LHC energies within the AMPT framework. However, the NCQ scaling is found to be valid in the Si-Si collision system at the same energy. The scaling holds true for all centrality classes in O-O collisions, which is a much smaller system, regardless of whether the nucleus is of the α-clustered type or the Woods-Saxon type. Therefore, the NCQ-scaling behavior does not appear to be affected by the existence of α-cluster geometry.

To better understand QGP-like effects, it is crucial to explore observable behaviour in various collision systems at the LHC with the same multiplicity environment. This strategy would significantly improve experimental efforts. This idea can be investigated by comparing observables that are sensitive to medium qualities in various system sizes. In summary, the new concept of final state multiplicity would drive system properties and bridge the gap across relevant colliding species and centralities, making the study of ultra-relativistic O-O Collisions at the LHC energy an important part of high-energy physics. In the following section, we have observed the behavior of the nuclear modification factor (R_{AA}) in the same multiplicity environment between O-O ccollsiions at $\sqrt{s_{\mathrm{NN}}} = 7$ TeV and Pb-Pb collsions at $\sqrt{s_{\mathrm{NN}}} = 5.02$ TeV. Additionally, we investigate the variation of R_{AA} across different rapidity intervals.

4.6 Nuclear modification factor

In this section, we examine the nuclear modification factor (R_{AA}) for all-charged hadrons and identified particles in O-O collisions at $\sqrt{s_{\mathrm{NN}}} = 7$ TeV. Table 4.5 shows the number of binary collisions ($\langle N_{\mathrm{coll}} \rangle$) from the Glauber model, the num-

ber of participating nucleons ($\langle N_{\rm part}\rangle$) from both AMPT and Glauber models, and the average charged-particle multiplicity ($\langle dN_{ch}/d\eta\rangle$) from AMPT and ALICE [63] for O-O [17] and Pb-Pb collisions at $\sqrt{s_{\rm NN}}$ = 7 TeV and 5.02 TeV respectively, at mid-rapidity. Table 4.5 presents the results, which show that the $\langle dN_{ch}/d\eta\rangle$ for the α-clustered density profile for (0-5)% of O-O collisions is approximately equal to the ALICE [63] Pb-Pb collisions for (50-60)% centrality. This is a remarkable finding regarding the role of multiplicities in relation to thermalization in small systems, as investigated by Landau in 1953 [64]. Van Hove expanded on this finding later in 1982 when he used multiplicity as a probe to investigate the possibility of a quark-hadron phase transition in small systems [28]. This demonstrates how crucial multiplicities are to the investigation of understanding the effects of the generated QCD medium. In this sec. 4.4.1, we show that the initial energy density generated in all O-O collision centralities are greater than the threshold for a deconfinement transition predicted by lattice QCD. This suggests the possibility of creating a QGP-like state in the oxygen nucleus collisions. Thus, it is interesting to investigate the effects of the medium formed in two distinct colliding systems (O-O and Pb-Pb), which have relatively similar numbers of final state charged particle multiplicity at particular centralities but differ in geometric overlap sizes [14]. Table 4.5 shows a discrepancy between the expected $\langle dN_{ch}/d\eta\rangle$ for Pb-Pb collisions based on AMPT simulation and ALICE experimental results. The discrepancy could be due to the AMPT model's inability to explain certain experimental results, as discussed in references. [65, 66]. Therefore, since multiplicities in these centralities are comparable, we continue to examine the behaviors of R_{AA} derived from ALICE results of (50-60)% centrality in Pb-Pb collisions and AMPT simulation of O-O collisions at (0-5)% centrality. We take into account both Woods-Saxon and α-clustered nuclear density profiles for oxygen nuclei in order to present a thorough and comparable conclusion.

The well-known expression for R_{AA} is as follows:

Table 4.5: Average charged-particle multiplicity density ($\langle dN_{\rm ch}/d\eta \rangle$) [from ALICE [63] and AMPT], number of participating nucleons ($\langle N_{\rm part} \rangle$) [from AMPT and Glauber model], and number of binary collisions ($\langle N_{\rm coll} \rangle$) [from Glauber model] for O–O collisions [17] at $\sqrt{s_{\rm NN}}$ = 7 TeV and for Pb–Pb collisions at $\sqrt{s_{\rm NN}}$ = 5.02 TeV in the pseudorapidity range $|\eta| < 0.5$.

System	$\sqrt{s_{\rm NN}}$ [TeV]	Centrality (%)	$\langle N_{\rm part} \rangle$[Glauber]	$\langle N_{\rm part} \rangle$ [AMPT]	$\langle N_{\rm coll} \rangle$ [Glauber]	$\langle dN_{ch}/d\eta \rangle$
O-O, $\alpha-$cluster	7	0–5	29.43 ± 2.02	30.73 ± 2.06	55.12 ± 8.90	187.54 ± 0.14
O-O, Woods-Saxon	7	0–5	28.00 ± 2.06	29.26 ± 1.99	48.33 ± 9.43	161.07 ± 0.15
Pb-Pb	5.02	50–60	53.6 ± 1.2	50.20 ± 7.04	90.88 ± 33.00	183.00 ± 8.00 [ALICE]
						235.25 ± 0.56 [AMPT]

$$\mathrm{R_{AA}} = \frac{\mathrm{d^2N^{AA}/dp_T d\eta}}{\langle \mathrm{N_{coll}} \rangle \mathrm{d^2N^{pp}/dp_T d\eta}} \tag{4.26}$$

where N^{pp} and N^{AA} represent the charged-particle yields in pp and A-A collisions, respectively. The average number of binary collisions is $\langle N_{coll} \rangle = \sigma_{inel}^{NN} \langle T_{AA} \rangle$, where σ_{inel}^{NN} is the total inelastic nucleon-nucleon cross section and $\langle T_{AA} \rangle$ is the mean nuclear thickness function. For O-O collisions, the $\langle N_{coll} \rangle$ values are derived from Ref. [17], while for Pb-Pb collisions, they are obtained using the Glauber model's impact parameter determination [67–69].

We begin by comparing the transverse momentum ($p_{\rm T}$) spectra from pp and Pb–Pb collisions with corresponding ALICE experimental data to evaluate the accuracy of the AMPT simulations. After that, we calculated the nuclear modification factor for charged hadrons in O-O collisions at $\sqrt{s_{\rm NN}}$ = 7 TeV. To investigate the impact of scaling on the estimation of the nuclear modification factor, we utilize both ALICE experimental data and AMPT simulations for particle yields in pp collisions. For scaling using ALICE experimental (AMPT simulated) data, we define R_{AA}^{Exp} (R_{AA}^{AMPT}). However, the AMPT simulation is the only source of the corresponding yields from O-O and Pb-Pb collisions. The effect of Woods-

Saxon and α-clustered nuclear density profiles on the nuclear modification factor, including contributions from identified particles, is also examined. The choice of phase space is likely to have an impact on this observable, which depends on basic quantities like rapidity (y). To account for this fact, we have also examined how the nuclear modification factor depends on the collisions' centrality and rapidity (y).

4.6.1 Simulation validation using p_{T}-spectra

Particle production yield and transverse momentum (p_{T}) spectra are crucial for understanding particle production in ultra-relativistic collisions. The dynamics of QCD matter can be better understood by examining high-p_{T} particle production and parton energy loss. Partons lose energy while moving through a medium, which results in parton splitting and gluon emission. The main objective of heavy-ion collisions is, therefore, to comprehend the mechanism of parton energy loss. The energy loss can be calculated by comparing the p_{T}-spectra of proton-proton (pp) collisions with heavy-ion collisions at the same energy. To comprehend the mechanism through which hard particles lose energy as they move through the medium, a detailed examination of R_{AA} is necessary. However, as indicated in Eq. 4.26, estimation of this observable requires input from both pp and heavy-ion collisions. For this reason, the tuning of the simulation is first validated by comparing the p_{T} spectra of all charged particles from AMPT with the corresponding ALICE experimental data. The setting for pp simulations in AMPT is reported in Ref. [37].

Figure 4.18 illustrates this comparison in Pb-Pb collisions at $\sqrt{s_{\mathrm{NN}}} = 5.02$ TeV for (50-60)% centrality, and Fig. 4.19 illustrates the comparison of charged particle p_{T}-spectra in pp collisions at $\sqrt{s} = 5.02$ TeV (left) and 7 TeV (right) for minimum bias respectively. This comparison shows the experimental data and the AMPT spectral shape agree well toward the high-p_{T} (> 4 GeV), but there is

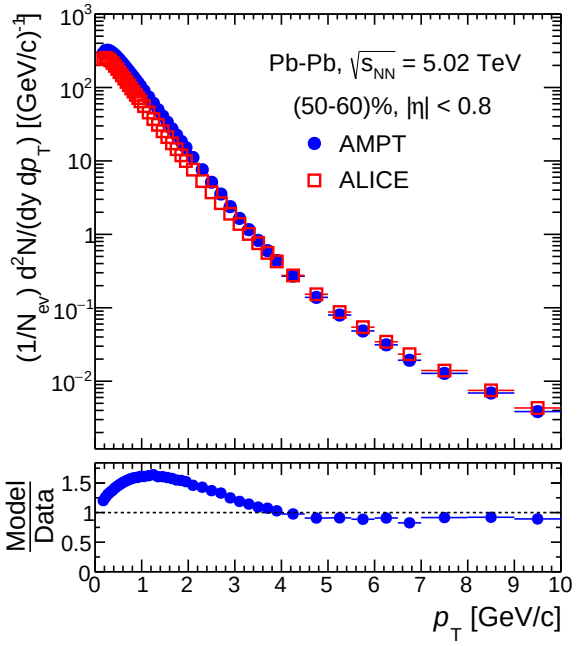

Figure 4.18: Comparison between the transverse momentum (p_{T}) spectra of charged particles from AMPT simulations and ALICE experimental data [70] for Pb–Pb collisions at $\sqrt{s_{\mathrm{NN}}} = 5.02$ TeV. The statistical uncertainties lie within the marker size [37].

a reasonable degree of deviation from the experimental results toward the low-p_{T} region. However, this also indicates, within uncertainties, that the experimental results within the acceptable range are quantitatively matched by the tuning of the AMPT simulation used in this work.

Figure 4.20 compares the p_{T}-spectra of identified particles from the AMPT simulated data at $\sqrt{s} = 5.02$ and 7 TeV with the ALICE experimental [72, 73] results respectively. These comparisons show that pions from AMPT show comparatively good agreement with the experimental data when uncertainties are taken into account, especially in the high-p_{T} region. However, there are notable differences between protons and kaons. It is clear that kaons and protons match the experimental data more closely as we move towards low-p_{T} ranges (< 1 GeV),

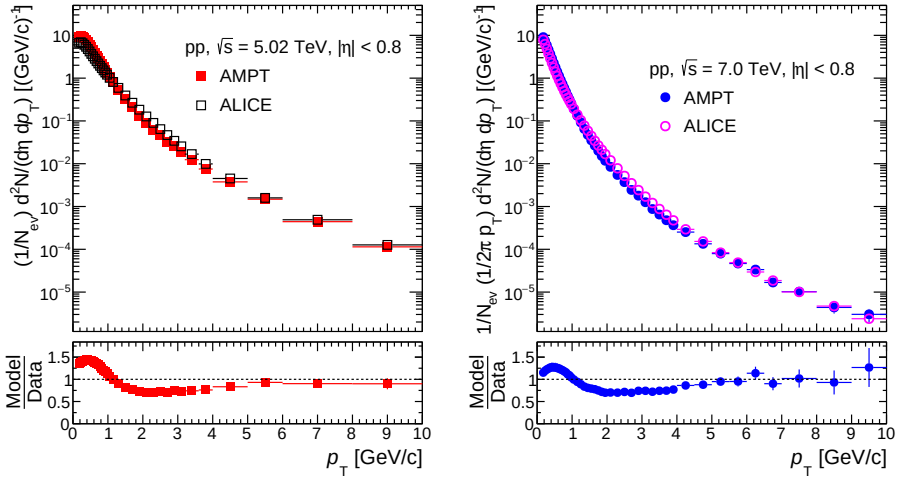

Figure 4.19: Comparison between the transverse momentum (p_{T}) spectra of charged particles from AMPT simulations and ALICE experimental data for pp collisions at $\sqrt{s} = 5.02$ TeV (left) [70] and $\sqrt{s} = 7$ TeV (right) [71]. The statistical uncertainties are within the marker size [37].

but there is still a discernible difference for pions. It is worth noting that, the scaling of R_{AA} throughout in the remainder of the article takes into account p_{T}-spectra in pp collisions from both AMPT and ALICE [70–73].

We proceed to obtain R_{AA} in ultra-relativistic O-O collisions after the comparison and simulation validation mentioned above. This system lies between Pb-Pb and pp collisions in terms of final-state multiplicity [74]. Though, the mean number of participants ($\langle N_{part} \rangle$) in the most central (0-5)% O-O collisions is said to be comparable to the $\langle N_{part} \rangle$ in peripheral (60-70)% Pb-Pb collisions [17, 75] in the MC-Glauber model computation. However, it has been observed that the charged particle multiplicity from AMPT simulations of O–O collisions in the (0–5)% centrality class is comparable to that of the (50–60)% centrality class in Pb–Pb collisions [17]. This fact is expected to be reflected in the p_{T}-spectra. In Fig. 4.21, we have shown charged particle p_{T}-spectra for the most central O-O collisions , taking into account both $\alpha-$clustered and Woods-Saxon density profiles.

These results are compared with ALICE data corresponding to the (50–60)% and (60–70)% centrality classes in Pb–Pb collisions at $\sqrt{s_{\rm NN}} = 5.02$ TeV.

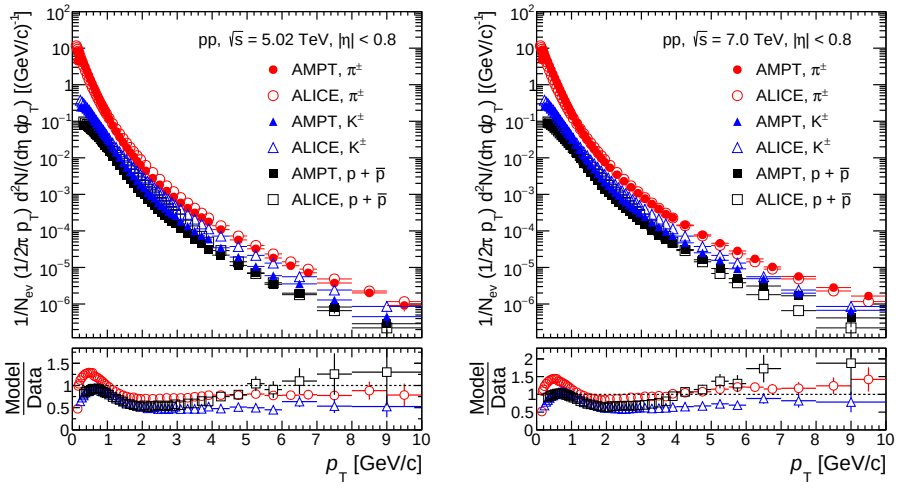

Figure 4.20: Comparison between the transverse momentum ($p_{\rm T}$) spectra of identified particles from AMPT simulations and ALICE experimental data for pp collisions at $\sqrt{s} = 5.02$ TeV (left) [72] and $\sqrt{s} = 7$ TeV (right) [73]. The statistical uncertainties are within the marker size [37].

It can be seen that in the lower panel of Fig. 4.21, the results for O–O collisions at $\sqrt{s_{\rm NN}} = 7$ TeV for (0-5)% centrality for both density profiles shows good agreement with the results for Pb-Pb collisions at $\sqrt{s_{\rm NN}} = 5.02$ TeV for (50-60)% centrality classes within uncertainties. Based on this observation, a comparative study is carried out in this work between the most central O–O collisions ((0–5)%) and mid-central Pb–Pb collisions ((50–60)%).

4.6.2 Nuclear modification factor (R_{AA}) vs. transverse momentum spectra ($p_{\rm T}$)

To ensure the reliability of $R_{\rm AA}$ predictions for the oxygen system, we first validated the AMPT model by evaluating its performance in describing this observable in Pb–Pb collisions. Fig. 4.22 illustrates the model-based investigation and

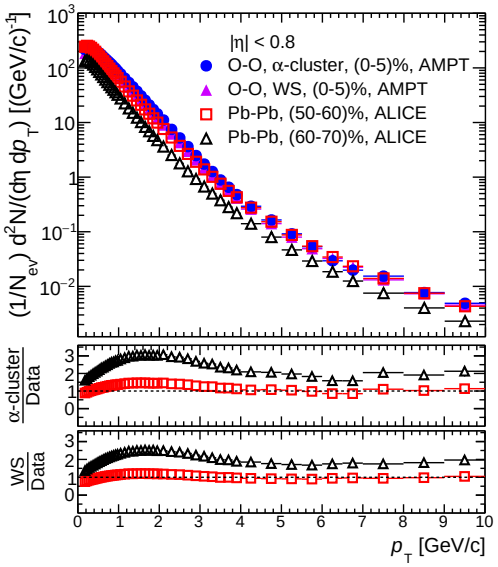

Figure 4.21: Comparison of the transverse momentum (p_{T}) spectra of charged particles from AMPT simulations for central (0–5)% O–O collisions at $\sqrt{s_{\mathrm{NN}}}$ = 7 TeV with the peripheral (50–60)% and (60–70)% ALICE results [70] for Pb–Pb collisions at $\sqrt{s_{\mathrm{NN}}} = 5.02$ TeV. The statistical uncertainties are within the marker size [37].

comparison of ALICE results for all charged hadrons. These figures illustrate the p_{T} dependence of R_{AA} for both charged hadrons and identified particles in the (50–60)% centrality class of Pb–Pb collisions at $\sqrt{s_{\mathrm{NN}}} = 5.02$ TeV.

The estimation of R_{AA} using collision results from pp collisions from ALICE (AMPT) data is shown in Figure 4.22 left (right). The AMPT simulation provides the Pb-Pb yields for both figures. The comparison shows that the simulated and experimental data for $p_{\mathrm{T}} < 4$ GeV differ significantly. As seen in Fig. 4.18, this discrepancy might be the consequence of a deviation in the particle's p_{T}-spectra towards the low-p_{T} range. At $p_{\mathrm{T}} > 3$ GeV, protons are also observed to be less suppressed than other hadrons. The difference in species-specific suppression implicates radial flow to a mass ordering toward $p_{\mathrm{T}} < 1.5$ GeV [42]. For

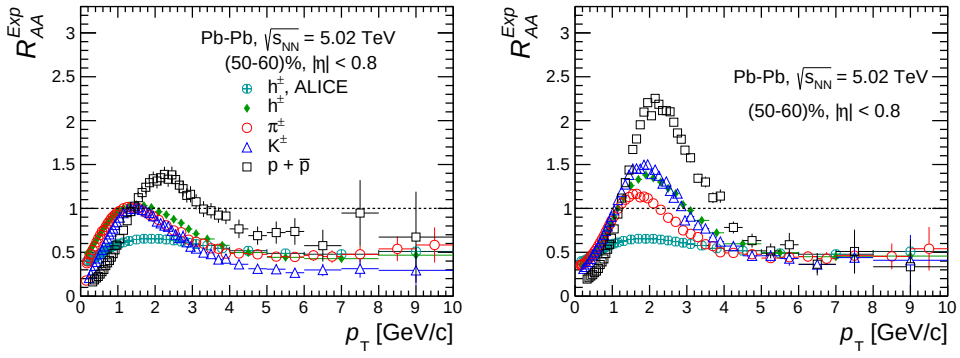

Figure 4.22: Nuclear modification factor of charged hadrons and identified particles in Pb–Pb collisions at $\sqrt{s_{\rm NN}} = 5.02$ TeV for the (50–60)% centrality class. The top-left plot shows the results obtained using the *pp* yield from ALICE experimental data and the Pb–Pb yield from AMPT simulations. The top-right plot displays the nuclear modification factor computed using both *pp* and Pb–Pb yields from AMPT simulations [37, 70].

$p_{\rm T} > 4$ GeV, a good agreement between the experimental results and the AMPT model is found.

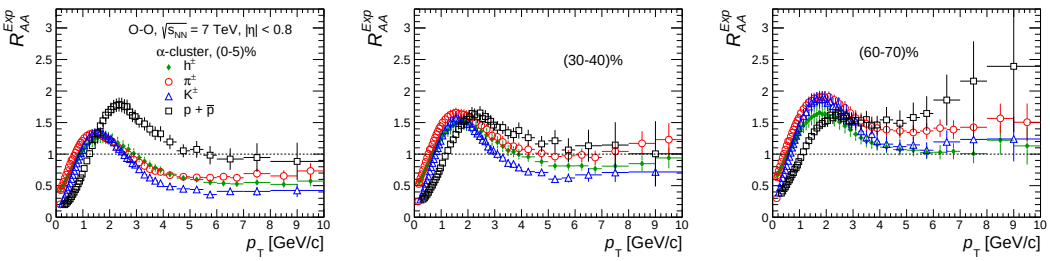

Figure 4.23: Nuclear modification factor (R_{AA}) for all charged hadrons ($h^{\pm}$) and identified particles ($\pi^{\pm}$, $K^{\pm}$, and $p + \bar{p}$) in O–O collisions at $\sqrt{s_{\rm NN}} = 7$ TeV is shown for three centrality classes: (0–5)% [Left], (30–40)% [Middle], and (60–70)% [Right]. The calculations are based on AMPT simulations with an α-clustered nuclear structure, using the $p_{\rm T}$ spectra from ALICE *pp* data to estimate R_{AA} [37].

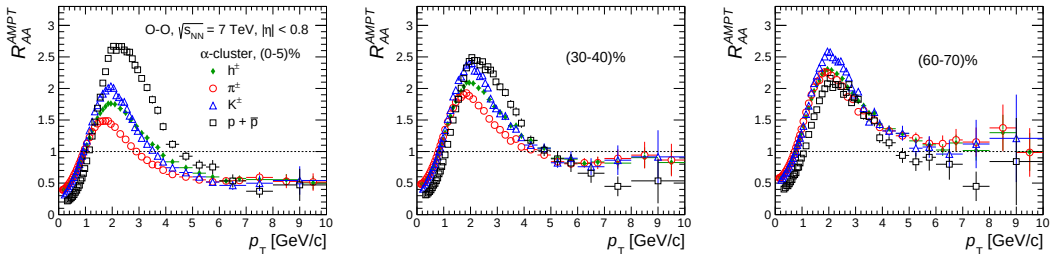

Figure 4.24: Nuclear modification factor (R_{AA}) for all charged hadrons ($h^{\pm}$) and identified particles ($\pi^{\pm}$, $K^{\pm}$, and $p + \bar{p}$) in O–O collisions at $\sqrt{s_{NN}} = 7$ TeV is shown for three centrality classes: (0–5)% [Left], (30–40)% [Middle], and (60–70)% [Right]. The results are obtained using AMPT simulations with an α-clustered nuclear structure, where the p_T spectra from AMPT pp collisions are used as the baseline to calculate R_{AA} [37].

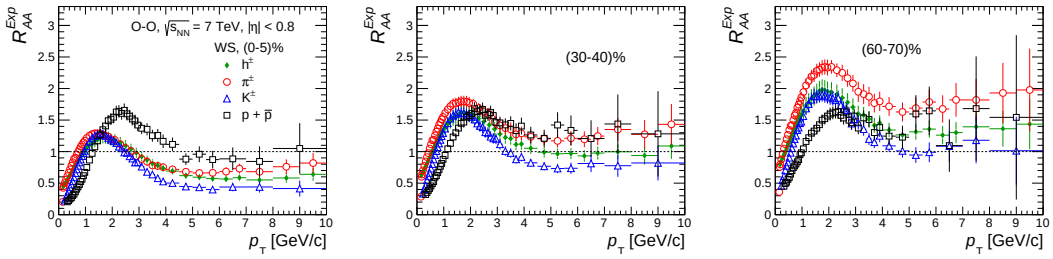

Figure 4.25: Nuclear modification factor (R_{AA}) for all charged hadrons ($h^{\pm}$) and identified particles ($\pi^{\pm}$, $K^{\pm}$, and $p + \bar{p}$) in O–O collisions at $\sqrt{s_{NN}} = 7$ TeV is presented for three centrality classes: (0–5)% [Left], (30–40)% [Middle], and (60–70)% [Right]. The results are obtained using the AMPT model with a Woods-Saxon nuclear density profile, employing p_T spectra from ALICE pp data to calculate R_{AA} [37].

Now we are proceeding with estimating R_{AA} in O−O collisions at $\sqrt{s_{NN}} = 7$ TeV. However, we took into consideration both $\alpha-$clustered (Fig. 4.23 and 4.24) and the Woods-Saxon (Fig. 4.25 and 4.26) density profiles in order to investigate the impact of the nuclear density profile on the production of charged particles. Additionally, Figures 4.23 and 4.24 present the results obtained by applying scal-

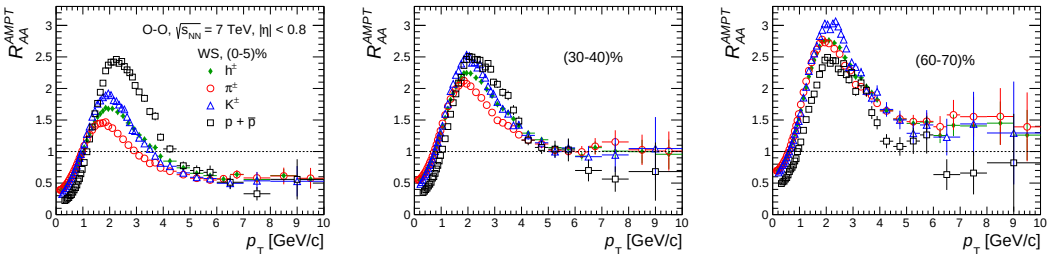

Figure 4.26: Nuclear modification factor (R_{AA}) for all charged hadrons ($h^{\pm}$) and identified particles ($\pi^{\pm}$, $K^{\pm}$, and $p + \bar{p}$) in O–O collisions at $\sqrt{s_{NN}} = 7$ TeV is shown for three centrality intervals: (0–5)% [Left], (30–40)% [Middle], and (60–70)% [Right]. The results are based on AMPT simulations using a Woods-Saxon nuclear density profile, with p_T spectra from AMPT pp collisions used as the baseline to estimate R_{AA} [37].

ing based on ALICE experimental data and AMPT simulations, respectively, to reflect the effect of scaling the nuclear modification factor (R_{AA}) with the p_T spectra from pp collisions. For the most central (0–5%), mid-central (30–40%), and peripheral (60–70%) collisions, the findings are shown. A clear mass ordering among $\pi^{\pm}$, $K^{\pm}$, and protons remains conserved towards $p_T < 2$ GeV, despite changes in density profiles and/or centralities, as can be shown from figures (4.23 - 4.26). But for both density profiles above $p_T > 2$ GeV, this pattern appears to break out. Using p_T-spectra of pp collisions from AMPT (Fig. 4.24, 4.26) reveals that the R_{AA} values are greater than those obtained using ALICE (Fig. 4.23, 4.25). Furthermore, a similar pattern is seen among the particles found in the most central collisions, which is in line with the results in Ref. [76], where mesons like $\phi(1020)$ and $K^{*0}(892)$ show lower R_{AA} values than protons at high p_T. This behaviour suggests that there may be a baryon-meson ordering.

In Fig. 4.27, the effects of density profiles for O−O collisions are further examined. Here, we consider $\alpha-$clustered and Woods-Saxon density profiles and investigate the ratio of R_{AA} of all charged hadrons using the transverse momentum at different centralities. One can observe that at the most central collisions

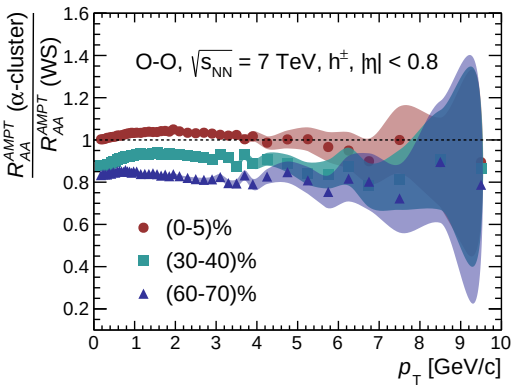

Figure 4.27: Ratio of the nuclear modification factor (R_{AA}) obtained using the α-clustered nuclear structure to that using the Woods–Saxon density profile for all charged hadrons (h$^{\pm}$) in O–O collisions at $\sqrt{s_{\rm NN}} = 7$ TeV. The shaded region represents the statistical uncertainties [37].

[(0-5)%], Woods-Saxon and $\alpha-$clustered density profiles have similar effects on charged hadron yield. However, taking into account the uncertainties, it is clear that nuclei with oxygen and α-clustered density profiles affect particle production more than those with Woods-Saxon profiles, especially in mid-central [(30–40)%] to peripheral [(60–70)%] collisions. This suggests that, in contrast to the Woods-Saxon density profile, colliding nuclei with $\alpha-$clustered structure produce a compact and denser fireball, especially in relatively non-central collisions. This finding contributes to a better understanding of the intricate physics at work in O$-$O collisions by illuminating the complex relationship between the internal structure of the nuclei, collision dynamics, and the subsequent particle production processes.

On further investigation of Fig. 4.23, 4.24, and Fig. 4.25, 4.26 it is observed in the intermediate $p_{\rm T}$ range, (1.5 GeV $< p_{\rm T} <$ 3.0 GeV) R_{AA} is seen to peak before dropping at higher-$p_{\rm T}$. The decline can be attributed to a single energy loss mechanism that affects all particle species at high $p_{\rm T}$ [70, 77]. In low and mid-$p_{\rm T}$ regions, radial boosts and $p_{\rm T}$-broadening contribute to observed trends [78].

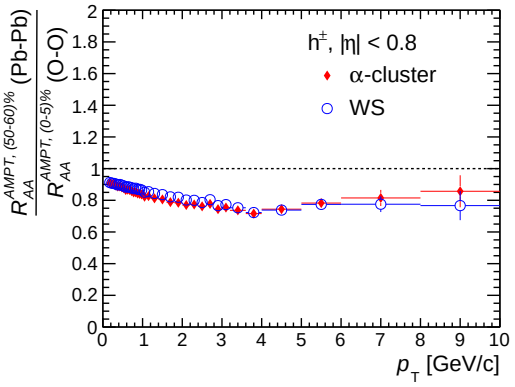

Figure 4.28: Ratio of the nuclear modification factor (R_{AA}) for charged hadrons in Pb–Pb collisions at $\sqrt{s_{\rm NN}} = 5.02$ TeV for the (50–60)% centrality class to that in O–O collisions at $\sqrt{s_{\rm NN}} = 7$ TeV for the (0–5)% centrality class. The statistical uncertainties are within the marker size [37].

Radial boosts reduce R_{AA} in the low-$p_{\rm T}$ region by pushing particles with low-$p_{\rm T}$ toward higher $p_{\rm T}$ regions [77]. However, a noticeable peak in the $p_{\rm T}$ spectrum results from $p_{\rm T}$-broadening brought on by several parton interactions. Furthermore, we find that most central collisions exhibit more suppression than peripheral collisions. This might be explained by the comparatively higher energy densities of the central collisions.

The (0–5)% centrality class of O–O collisions and the (50–60)% class of Pb–Pb collisions show similar charged-particle multiplicities, as described in Section 4.6.1. We compare the ratio of R_{AA} in Pb–Pb (50–60%) collisions to that in O–O (0–5%) collisions for all charged hadrons in order to investigate the effect of this similarity on the nuclear modification factor. Both α-clustered and Woods-Saxon density profiles for the oxygen nuclei are used in the investigation. This ratio of the R_{AA} value in Pb-Pb collisions is lower than in O-O collisions, as Figure 4.28 illustrates. In Pb-Pb collisions, the suppression effect is more pronounced than in O-O collisions with similar multiplicity ranges. In compar-

ison to O–O collisions at the same multiplicity, Pb–Pb collisions have a radius that is almost 60% larger (Ref. [14]). This finding implies that partons travel a longer path length when they propagate through a dense medium formed in Pb-Pb collisions (relatively bigger nuclei). In comparison to O-O collisions, this longer path length leads to a higher energy loss. This finding is consistent with the study reported in Ref. [79] that looked at the R_{AA} for Pb-Pb collisions and Xe-Xe collisions at comparable multiplicity.

4.6.3 R_{AA} variation with η

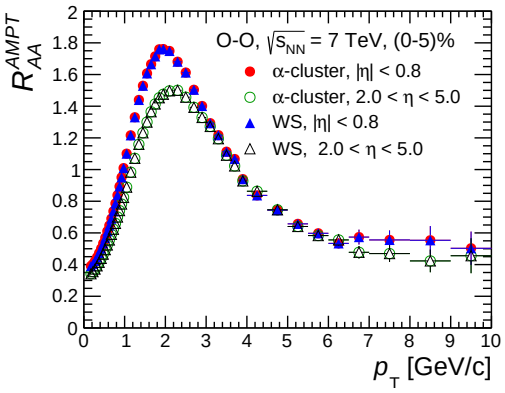

Figure 4.29: Rapidity dependence of the nuclear modification factor for charged hadrons in O–O collisions at $\sqrt{s_{\rm NN}} = 7$ TeV for the 0–5% centrality class. [37].

We know that the gluon-rich medium is the main source of particle production at mid-rapidity. The constituent quarks control the particle production mechanism at forward rapidity. Therefore, it is interesting to study the rapidity dependence on the relative yield of the particles produced in ultra-relativistic collisions. Figure 4.29 shows R_{AA} for all charged hadrons in (0-5)% centrality class at mid ($|\eta| < 0.8$) and forward ($2 < \eta < 5$) rapidity interval for both α-cluster and Woods-Saxon density profiles in O-O collisions at $\sqrt{s_{\rm NN}} = 7$ TeV. It should be noted that the selected rapidity regions were taken from Ref. [17]. The open and closed markers represent the nuclear modification factors evaluated at

forward and mid rapidity, respectively. Figure 4.29 shows that the AMPT model predicts a lower yield of charged particles at forward rapidity compared to mid-rapidity, particularly for $p_{\mathrm{T}} \approx 3$ GeV. All charged particles are, however, equally suppressed at mid and forward rapidity at $p_{\mathrm{T}} > 3$ GeV. It means that particles traveling at high speeds are not affected by the distribution of the phase space. The phenomenon indicates that the fastest-moving particles leave the system before experiencing any significant energy loss in the medium. At a given rapidity, we have also found that the nuclear modification factor is independent of the alpha-cluster and Wood-Saxon density profiles.

4.7 Summary

Section 4.4: In this work, we use a multi-phase transport model (AMPT) to provide the predictions for global properties in O-O collisions at $\sqrt{s_{\mathrm{NN}}} = 7$ TeV. As a function of collision centrality, we present the kinetic freeze-out parameters, p_{T}-spectra, squared speed of sound, transverse mass, Bjorken energy density, pseudorapidity distributions, mid-rapidity charged-particle multiplicity, and transverse mass. The findings are shown for Woods-Saxon and harmonic oscillator nuclear density profiles, as well as the α-clustered structure included for the oxygen nucleus. Changing the density profile from Woods-Saxon to the harmonic oscillator and implementing α-clustered in the nucleus results in a modification in average charged-particle multiplicity, which is also reflected in the initial energy density, as one would expect. All collision centralities in O-O collisions at $\sqrt{s_{\mathrm{NN}}} = 7$ TeV yield an initial energy density that is typically larger than the value anticipated by lattice QCD for a deconfinement transition, indicating the possibility of QGP production. Additionally, the current research also shows a comparable freeze-out temperature and a significant radial flow.

Section 4.5: The effects of Woods-Saxon and α-clustered nuclear geometry

on eccentricity and triangularity, as well as their correlations, elliptic flow, triangularity flow, and NCQ scaling in O-O collisions at $\sqrt{s_{\rm NN}} = 7$ TeV, have been studied in this section. We note,

1. Eccentricity and triangularity are observed to vary with density profiles. However, the consequences are more obvious in the most central case, where the initial state has greater triangularity than eccentricity for a α-clustered oxygen nucleus, compared to the standard Woods-Saxon distribution.

2. Using normalized symmetric cumulants, we found a stronger association between eccentricity and triangularity in the Woods-Saxon density profile compared to the α-clustered structure. In the central collisions, the $\alpha-$clustered nucleus shows a negative NSC (2,3) value.

3. The elliptic flow in the Woods-Saxon type nucleus is found to have a weak dependence on collision centrality. However, in the $\alpha-$clustered nucleus, the elliptic flow increases from central to mid-central collisions, then drops from mid to periphery collisions.

4. We found that the $\langle v_3 \rangle / \langle v_2 \rangle$ is higher for the $\alpha-$clustered nucleus compared to the Woods-Saxon scenario.

5. The two-particle azimuthal correlation function $[C(\Delta\phi)]$ of the identified particles is broadened away-side by the α-clustered type nucleus. This implies a more compact system formation in the nucleus of the α-clustered system.

6. The number-of-constituent-quark (NCQ) scaling holds across all centrality classes, for both Woods-Saxon and α-clustered nuclear configurations. This observation is significant as it indicates the formation of a deconfined partonic medium in O-O collisions at $\sqrt{s_{\rm NN}} = 7$ TeV and the appearance of partonic collectivity.

4.7 Summary

Section 4.6: Here we examine the nuclear modification factor (R_{AA}) for O-O collisions at $\sqrt{s_{\rm NN}}$ = 7 TeV at the LHC. We observe the behavior of the nuclear modification factor between O-O and Pb-Pb collisions at similar multiplicity environments. We also investigate the dependence on density profiles, such as α-clustered and Wood-Saxon patterns. Lastly, we examine how the nuclear modification factor for O-O collisions at $\sqrt{s_{\rm NN}} = 7$ TeV depends on rapidity. The key conclusions regarding O–O Collisions from this section are summarized below:

1. Regardless of the density profiles utilised, it is found that the nuclear modification factor (R_{AA}) of charged hadrons and identifiable particles for O-O collisions is smaller for the most central (0-5)% collisions than for the peripheral collisions (60-70)%.

2. The mass-ordering of the identified particles is shown to be constant in the low-$p_{\rm T}$ region (< 2 GeV), regardless of variations in centralities and/or density profiles. However, for $p_{\rm T} > 2$ GeV, this behavior changes, and a distinct baryon-meson separation becomes apparent at higher $p_{\rm T}$, especially in the most central collisions.

3. Using the $p_{\rm T}$-spectra of pp collisions from the AMPT simulation, we found that the R_{AA} values show higher values than those obtained using ALICE data. This illustrates the inadequacy of the AMPT Model by proving that pp collisions at ALICE produce more hadrons than the AMPT simulation.

4. The analysis of R_{AA} for identified particles and charged hadrons shows that, in contrast to the Woods-Saxon density profile, α-clustered density profiles have a stronger effect on particle generation in mid-central and peripheral collisions than in most central collisions. A denser fireball may be produced by collisions between nuclei with α-clustered structure, particularly in non-central collisions.

5. We found that Pb-Pb collisions with a centrality of 50-60% exhibit stronger suppression than O-O collisions with a centrality of 0-5% while having the same final state multiplicity. This emphasizes the role of system size in hadron production, as Pb–Pb collisions provide a significantly larger nuclear medium compared to O–O collisions.

6. For charged hadrons in O-O collisions at $\sqrt{s_{\mathrm{NN}}} = 7$ TeV, we found a much reduced yield at forward rapidity compared to mid-rapidity in the context of rapidity dependency. The nuclear modification factor within a given rapidity window is observed to be independent of the choice of nuclear density profiles.

Bibliography

[1] J. Adam *et al.* [ALICE Collaboration], Nature Phys. **13**, 535 (2017).

[2] V. Khachatryan *et al.* [CMS Collaboration], Phys. Lett. B **765**, 193 (2017).

[3] R. Sahoo, AAPPS Bull. **29**, 16-21 (2019).

[4] R. Sahoo and T. K. Nayak, Curr. Sci. **121**, 1403 (2021).

[5] J. Brewer, A. Mazeliauskas and W. van der Schee, [arXiv:2103.01939].

[6] S. Acharya et al. [ALICE Collaboration], ALICE-PUBLIC-2021-004 (2021).

[7] M. Rybczyński and W. Broniowski, Phys. Rev. C **100**, 064912 (2019).

[8] S. Huang, Z. Chen, J. Jia and W. Li, Phys. Rev. C **101**, 021901 (2020).

[9] B. Schenke, C. Shen and P. Tribedy, Phys. Rev. C **102**, 044905 (2020).

[10] B. G. Zakharov, JHEP **09**, 087 (2021).

[11] A. Huss, A. Kurkela, A. Mazeliauskas, R. Paatelainen, W. van der Schee and U. A. Wiedemann, Phys. Rev. C **103**, 054903 (2021).

[12] S. H. Lim, J. Carlson, C. Loizides, D. Lonardoni, J. E. Lynn, J. L. Nagle, J. D. Orjuela Koop and J. Ouellette, Phys. Rev. C **99**, 044904 (2019).

[13] A. M. K. R, S. Prasad, N. Mallick, R. Sahoo and G. G. Barnaföldi, [arXiv:2505.22367 [hep-ph]].

[14] M. D. Sievert and J. Noronha-Hostler, Phys. Rev. C **100**, 024904 (2019).

[15] D. Behera, S. Prasad, N. Mallick and R. Sahoo, Phys. Rev. D **108**, no.5, 054022 (2023).

[16] G. Röpke, P. Schuck, C. Xu, Z. Ren, M. Lyu, B. Zhou, Y. Funaki, H. Horiuchi, A. Tohsaki and T. Yamada, J. Low Temp. Phys. **189**, 383 (2017).

[17] D. Behera, N. Mallick, S. Tripathy, S. Prasad, A. N. Mishra and R. Sahoo, Eur. Phys. J. A **58**, 175 (2022).

[18] A. Menon Kavumpadikkal Radhakrishnan, S. Prasad, N. Mallick and R. Sahoo, Eur. Phys. J. A **61**, 134 (2025)

[19] S. Prasad, N. Mallick, R. Sahoo and G. G. Barnaföldi, Phys. Lett. B **860**, 139145 (2025)

[20] Y. A. Li, S. Zhang and Y. G. Ma, Phys. Rev. C **102**, 054907 (2020).

[21] G. Gamow, Constitution of Atomic Nuclei and Radioactivity (Clarendon Press, Oxford, 1931).

[22] J.A. Wheeler, Phys. Rev. **52**, 1083 (1937).

[23] W. Broniowski and E. Ruiz Arriola, Phys. Rev. Lett. **112**, 112501 (2014).

[24] P. Bozek, W. Broniowski, E. Ruiz Arriola and M. Rybczynski, Phys. Rev. C **90**, 064902 (2014).

[25] P. Bozek and W. Broniowski, Phys. Lett. B **739**, 308 (2014).

[26] Rohlf, James William, Modern Physics from α to Z^0, Wiley (1994).

[27] Z. W. Lin, C. M. Ko, B. A. Li, B. Zhang and S. Pal, Phys. Rev. C **72**, 064901 (2005).

[28] L. Van Hove, Phys. Lett. **118B**, 138 (1982).

[29] J. D. Bjorken, Phys. Rev. D **27**, 140 (1983).

[30] X. N. Wang and M. Gyulassy, Phys. Rev. D **44**, 3501 (1991).

[31] B. Zhang, Comput. Phys. Commun. **109**, 193 (1998).

[32] Z. W. Lin, C. M. Ko, B. A. Li, B. Zhang and S. Pal, Phys. Rev. C **72**, 064901 (2005).

[33] Z. W. Lin and C. M. Ko, Phys. Rev. C **65**, 034904 (2002).

[34] Y. He and Z. W. Lin, Phys. Rev. C **96**, 014910 (2017).

[35] B. Li, A. T. Sustich, B. Zhang and C. M. Ko, Int. J. Mod. Phys. E **10**, 267 (2001).

[36] V. Greco, C. M. Ko and P. Levai, Phys. Rev. C **68**, 034904 (2003).

[37] D. Behera, S. Deb, C. R. Singh and R. Sahoo, Phys. Rev. C **109**, 014902 (2024).

[38] F. Karsch, Nucl. Phys. A **698**, 199, (2002).

[39] L. D. Landau, Izv. Akad. Nauk Ser. Fiz. **17**, 51 (1953).

[40] E. Abbas *et al.* [ALICE Collaboration], Phys. Lett. B **726**, 610 (2013).

[41] R. Sahoo, A. N. Mishra, N. K. Bahera and B. K. Nandi, Adv. High Energy Phys. **2015**, 612390 (2015).

[42] S. Acharya *et al.* [ALICE Collaboration], Phys. Rev. C **101**, 044907 (2020).

[43] E. Schnedermann, J. Sollfrank and U. W. Heinz, Phys. Rev. C **48**, 2462 (1993).

[44] P. Huovinen, P. F. Kolb, U. W. Heinz, P. V. Ruuskanen and S. A. Voloshin, Phys. Lett. B **503**, 58 (2001).

[45] P. Braun-Munzinger, J. Stachel, J. P. Wessels and N. Xu, Phys. Lett. B **344**, 43 (1995).

[46] Z. Tang *et al.*, Chin. Phys. Lett. **30**, 031201 (2013).

[47] K. Adcox *et al.* [PHENIX Collaboration], Phys. Rev. C **69**, 024904 (2004).

[48] U. Heinz and R. Snellings, Ann. Rev. Nucl. Part. Sci. **63**, 123 (2013).

[49] S. A. Voloshin, A. M. Poskanzer and R. Snellings, Landolt-Bornstein **23**, 293 (2010).

[50] J. Y. Ollitrault, Phys. Rev. D **46**, 229 (1992).

[51] S. Voloshin and Y. Zhang, Z. Phys. C **70**, 665 (1996).

[52] J. Adams *et al.* (STAR Collaboration), Nucl. Phys. A **757**, 102 (2005).

[53] V. Khachatryan *et al.* (CMS Collaboration), Phys. Lett. B **765**, 193 (2017).

[54] B. B. Abelev et al. (ALICE Collaboration), JHEP **1506**, 190 (2015).

[55] G. Aad *et al.* (ATLAS Collaboration), Phys. Rev. C **86**, 014907 (2012)

[56] A. K. Chaudhuri, Phys. Lett. B **713**, 91 (2012).

[57] S. Prasad, N. Mallick, S. Tripathy and R. Sahoo, Phys. Rev. D **107**, 074011 (2023).

[58] H. Petersen, G. Y. Qin, S. A. Bass and B. Muller, Phys. Rev. C **82**, 041901 (2010).

[59] P. Dasgupta, G. L. Ma, R. Chatterjee, L. Yan, S. Zhang and Y. G. Ma, Eur. Phys. J. A **57**, 134 (2021).

[60] B. Schenke, S. Jeon and C. Gale, Phys. Rev. C **85**, 024901 (2012).

[61] N. Mallick, S. Tripathy and R. Sahoo, Eur. Phys. J. C **82**, 524 (2022).

[62] Y. Z. Wang, S. Zhang and Y. G. Ma, Phys. Lett. B **831**, 137198 (2022).

[63] J. Adam *et al.* [ALICE Collaboration], Phys. Rev. Lett. **116**, 222302 (2016).

[64] L. D. Landau, Izv. Akad. Nauk. SSSR **17**, 51 (1953); S. Belenkij and L. D. Landau, Usp. Fiz. Nauk. **56**, 309 (1955): Nuovo Cimento Suppl. **3**, 15 (1956); D. ter Haar (Ed.), Collected papers of L.D. Landau, Gordon & Breach, New York, 1965, p. 665.

[65] B. B. Abelev *et al.* [ALICE Collaboration] , Phys. Lett. B **727**, 371 (2013).

[66] Z. W. Lin and L. Zheng, Nucl. Sci. Tech. **32**, 113 (2021).

[67] M. L. Miller, K. Reygers, S. J. Sanders and P. Steinberg, Ann. Rev. Nucl. Part. Sci. **57**, 205 (2007).

[68] C. Loizides, Phys. Rev. C **94**, 024914 (2016).

[69] R. J. Glauber and G. Matthiae, Nucl. Phys. B **21**, 135 (1970).

[70] S. Acharya *et al.* [ALICE Collaboration], JHEP **11**, 013 (2018).

[71] B. B. Abelev *et al.* [ALICE Collaboration], Eur. Phys. J. C **73**, 2662 (2013).

[72] J. Adam *et al.* [ALICE Collaboration], Phys. Lett. B **760**, 720 (2016).

[73] J. Adam *et al.* [ALICE Collaboration], Eur. Phys. J. C **75**, 226 (2015).

[74] A. Huss, A. Kurkela, A. Mazeliauskas, R. Paatelainen, W. van der Schee and U. A. Wiedemann, Phys. Rev. Lett. **126**, 192301 (2021).

[75] C. Loizides, J. Kamin and D. d'Enterria, Phys. Rev. C **97**, 054910 (2018) [erratum: Phys. Rev. C **99**, 019901 (2019)].

[76] J. Adam *et al.* [ALICE Collaboration], Phys. Rev. C **95**, 064606 (2017).

[77] F. X. Liu, Z. L. She, H. G. Xu, D. M. Zhou, G. Chen and B. H. Sa, Sci. Rep. **12**, 1772 (2022).

[78] J. W. Cronin *et al.* [E100 Collaboration], Phys. Rev. D **11**, 3105 (1975).

[79] S. Acharya *et al.* [ALICE Collaboration], Phys. Lett. B **788**, 166 (2019).

Chapter 5

Summary

This thesis reports the first measurements of barrel charged-particle multiplicity at midrapidity in pp collisions at $\sqrt{s} = 13.6$ TeV with ALICE at the LHC. We studied how the number of generated and reconstructed charged particles is related and found a clear linear correlation. The average number of charged particles was calculated for different multiplicity ranges. The J/ψ particle is identified through its decay into two muons ($J/\psi \rightarrow \mu^+\mu^-$) using the ALICE muon spectrometer. We used tracks coming from the primary vertex within the pseudo-rapidity range $|\eta| < 0.8$ to estimate the charged particle multiplicity. An iterative Bayesian unfolding method was used to correct the raw track counts to get the true number of charged particles. The muon spectrometer also allows us to detect muons with very low transverse momentum (p_T), in the range $-4.0 < \eta < -2.5$. Further, we have corrected the multiplicity distribution by taking care of the efficiency estimated from MC data. The J/ψ number is extracted from different multiplicity bins with an integrated multiplicity bin by fitting invariant mass spectra to the CB2+VWG function. Further, we estimate the relative self-normalized J/ψ yields with respect to self-normalised charged particle multiplicity. At last, we estimate the ratio of self-normalized $\psi(2S)$-over-J/ψ yields as a function of self-normalised charged particle multiplicity.

Further in this thesis, we investigate light-flavor observables in O–O collisions at $\sqrt{s}_{NN} = 7$ TeV, using the A Multi-Phase Transport (AMPT) model. The aim is to characterize collective dynamics and probe the possibility of QGP formation in O-O collisions. We have studied the global observables in O-O collisions with implementing different nuclear density profiles. These are Woods-Saxon, harmonic oscillator, and α-clustered configurations. Using these density profiles, we have observed the Bjorken energy density, pseudorapidity distributions, squared speed of sound, freeze-out parameters, and particle ratios. By changing the nuclear density profile from Woods–Saxon to harmonic oscillator and implementing an α-clustered structure, we observe a noticeable modification in the average charged-particle multiplicity. This alteration also reflects in the initial energy density, which remains above the lattice QCD-predicted threshold for deconfinement across all centralities, suggesting that O–O Collisions at LHC energies can potentially form a QGP-like state. The squared speed of sound (c_s^2) has been estimated in O–O collisions at $\sqrt{s_{NN}} = 7$ TeV. We found a minimal dependency of c_s^2 on centrality classes. Additionally, a strong radial flow and freeze-out temperatures comparable to those observed in Pb–Pb collisions are also reported, supporting the formation of a thermalized medium in O–O collisions.

Further, we investigate the influence of different nuclear density profiles, i.e, Woods-Saxon and α-clustered, on the initial geometry and final-state observables in O–O collisions at $\sqrt{s_{\rm NN}} = 7$ TeV. The initial-state eccentricity and triangularity are found to vary with the chosen profile, with the α-clustered structure exhibiting more triangularity than eccentricity in the most central collisions. Using normalized symmetric cumulants, we observe a stronger correlation between eccentricity and triangularity for the Woods-Saxon case, while a negative NSC(2,3) value appears in the central events for the α-clustered nucleus, reflecting distinct geometric fluctuations. The elliptic flow (v_2) shows only a mild dependence on centrality for the Woods-Saxon profile, whereas for the α-clustered configuration,

v_2 increases from central to mid-central collisions before decreasing in peripheral events. Additionally, the ratio $\langle v_3 \rangle / \langle v_2 \rangle$ is enhanced towards central collisions in the α-clustered scenario, indicating stronger triangular flow contributions. Two-particle azimuthal correlations reveal an away-side broadening for the α-clustered nucleus, suggesting a denser and more compact system. Finally, the validity of the number-of-constituent-quark (NCQ) scaling across all centralities for both profiles points to the emergence of partonic collectivity and the possible formation of a deconfined medium in these small collision systems.

Furthermore we have studied the nuclear modification factor ($R_{\rm AA}$) in O–O collisions at $\sqrt{s_{\rm NN}} = 7$ TeV. We observe that both charged hadrons and identified particles show a clear centrality dependence, with stronger suppression observed in the most central (0–5%) collisions compared to peripheral (60–70%) collisions, irrespective of the nuclear density profile. At low transverse momentum ($p_{\rm T} < 2$ GeV), a consistent mass ordering among identified particles persists across all centralities and density profiles, while at higher $p_{\rm T}$, this ordering transitions into a distinct baryon-meson separation, particularly evident in central collisions. Comparisons with reference *pp* spectra from AMPT simulations reveal that the $R_{\rm AA}$ values are systematically higher than those obtained using ALICE *pp* data, indicating an overestimation of hadron production in AMPT. Furthermore, the impact of the α-clustered structure becomes more significant in mid-central and peripheral collisions than in the most central ones, suggesting the formation of a denser fireball in non-central collisions for clustered nuclei. Additionally, it is observed that at similar final-state multiplicities environment, the (50–60)% centrality class in Pb–Pb collisions shows stronger suppression than the (0–5)% centrality class in O–O collisions. This highlights the crucial role of system size, with Pb–Pb collisions producing a denser and larger environment than O–O collisions. Finally, it is observed that the yield of charged hadrons is lower at forward rapidity than at mid-rapidity, though the rapidity-dependent $R_{\rm AA}$ remains unaf-

fected by the choice of density profile.